Heat Sink Performance of Electrodeposited Copper-Diamond Composites

by

Hussain Syed

Thesis submitted to the University of Ottawa
in partial fulfilment of the requirements for Master of Applied Science in

Advanced Materials and Manufacturing

Department of Mechanical Engineering

Faculty of Engineering

University of Ottawa

© Hussain Syed, Ottawa, Canada, 2026

Heat Sink Performance of Electrodeposited Copper-Diamond Composites

Hussain Syed

Thesis submitted as a requirement for Master of Applied Science in

Advanced Materials and Manufacturing, University of Ottawa, 2026

Abstract

The rapid advancement of modern electronics has intensified thermal management challenges, driving the need for heat sink materials with high thermal conductivity and efficient heat removal. Electrodeposited copper–diamond (Cu-D) composites show strong potential for next-generation electronic applications, offering thermal conductivities exceeding those of conventional metals while remaining more economical than composites produced through high-temperature–high-pressure methods. Despite this promise, most studies emphasize intrinsic material properties rather than evaluating practical cooling performance. This thesis investigates the heat sink behavior of electrodeposited Cu-D composites under realistic operating conditions using LED junction-to-ambient thermal resistance. Cu-D samples containing uncoated and TiC-coated diamond particles, arranged in single-layer and multi-layer architectures, were fabricated and assessed. Uncoated composites exhibited poorer heat sink performance than pure copper due to small, equiaxed copper grains near the Cu-D interface, which limited thermal boundary conductance despite being free of interfacial voids. In contrast, TiC-coated diamond particles significantly lowered steady-state LED temperatures, demonstrating the importance of interfacial engineering in improving phonon transport across metal–diamond interfaces. The influence of thermal interface materials (TIMs) was also examined. Incorporating 10–30 wt.% diamond particles into the commercial thermal paste further reduced LED temperatures, even though the thicker bond-line would typically increase thermal resistance. This shows that TIM formulation plays an additional role in determining overall heat sink effectiveness. Overall, this work advances electrodeposited Cu–D composites toward practical heat sink applications and shows that interfacial coatings, copper microstructure, and TIM design collectively influence thermal performance.

Acknowledgements

Alhamdulillah, all praise and gratitude are due to the Almighty (swt), by whose grace and guidance this achievement was made possible. This, followed by my gratitude to Professor Hai Jun Cho for taking me under his wing, and giving me the opportunity in his Solid-State Kinetics Lab to fulfill the requisites for the fulfillment of my MASc degree. His guidance, patience and support have been invaluable, and he has not only taught me things throughout my degree, but real-life lessons as well.

Thank you to all my colleagues, especially Sophie Kim, Xinrui Dong, and Junhee Park. I am sincerely grateful for everything I learned from each of you. Sophie's help and support in the lab during the summer made a tremendous difference, and the discussions and guidance from Xinrui and Junhee consistently strengthened my understanding and progress. I will always appreciate the impact you have had on my journey.

My utmost expression of respect and love goes to my parents, Sohail Akhtar and Seema Sohail, for their unwavering encouragement, guidance, and for always being there to provide assurance and emotional support through every high and low of this journey. I owe it to them for raising me to be the man I am today, one with the fortitude and resilience to keep pushing forward no matter the circumstances. I am equally grateful to my brother, Hasan, and my sister, Maryam, whose constant encouragement, understanding, and belief in me have been a source of strength and motivation throughout this process. I would also like to extend my heartfelt appreciation to my friends back home, whose continued support, prayers, and faith in me have played a meaningful role in carrying me through this path.

I look forward to what is to come and ask Allah (swt) to grant me the best of both worlds. Ameen.

Table of Contents

Chapter 1: Introduction and motivation for this research 1

Chapter 2: Literature Review 7

2.1. Heat Removal in Engineering & Electronic Devices 7

2.1.1 Active and Passive Cooling Strategies 7

2.1.2 Hybrid Cooling Approaches 10

2.2 Interface Bonding Between Heat sinks and Components 11

2.2.1 Thermal Interface Materials (TIMs) 12

2.2.2 Bonding Techniques 15

2.3 Metal-Diamond Composite heat sink materials via HTHP methods 17

2.4 Electrodeposition of copper-diamond composites 21

2.5 Metrics for Measuring Heat sink Performance 23

2.6 Predictive Models for Effective Thermal Conductivity of Composites 26

2.6.1 Hasselman–Johnson (H–J) Model 26

2.6.2 Differential Effective Medium (DEM) Model 27

Chapter 3: Experimental Procedures 29

3.1 Materials and Methods 29

3.2 Sample dimensions and diamond volume fraction calculations 34

3.3 Scanning electron microscopy and X-ray diffraction 35

3.4 Heat sink performance testing and setup 37

3.5 Preparation of diamond-modified thermal interface materials 39

Chapter 4: Heat Sink Performance of Electrodeposited Copper–Diamond Composites Using Thermal Tape Interface **41**

4.1 Electron microscopy and X-ray diffraction patterns 41

4.2 Heat sink performance of electrodeposited copper-diamond composites 44

4.3 Discussions 47

4.4 Research Contributions from This Chapter 51

Chapter 5: Engineering Thermal Interface Materials and its Effect on the Performance of Metal-Based Heat Sink Materials **53**

5.1 Thermal Interface Materials Used in This Chapter 53

5.2 Results and discussion 55

5.3 Contribution from this chapter 58

Chapter 6: Conclusion and Future Work **60**

6.1 Conclusions 60

6.2 Future Work 61

6.2.1 Thermo-Mechanical Reliability and Long-Term Stability 61

6.2.2 Fabrication of Fin-Shaped and Structured Copper–Diamond Composites 62

Appendix A: Supplemental Materials **77**

A.1 Sample Orientation Index Calculation 77

A.2 DEM-Based Evaluation of the Influence of Thermal Boundary Conductance on Composite Thermal Conductivity 80

A.3 Copper–diamond TBC values from literature 82

A.4 Manual Lower- and Upper-Bound Pore Population Analysis 83

A.5 Thermal paste lightly pressed vs hardly pressed 84

A.6 Steady-State Thermal calculations with Convection, Radiation and Interfacial Resistance 85

A.7 Sample Copper Deposition Thickness Estimation for Agitation Timing........................... 89

List of Tables

Table 2.1 - Summary of Cooling Methods, Applications, and Key Considerations................ 11

Table 2.2 - Reported thermal conductivities of Al–diamond composites................................ 19

Table 2.3 - Reported thermal conductivities of Cu-D composites... 21

Table 2.4 - Reported thermal conductivities of electrodeposited Cu–diamond composites..... 23

Table 3.1 - Bath composition and plating parameters.. 31

Table 3.2 - Dimensions and diamond volume fractions of heat sink samples.......................... 35

Table 4.1 - Copper crystallographic orientation indices 44

Table 4.2 – Steady-state LED temperatures with different heat sink materials........................ 45

Table 5.1 – Steady-state LED temperatures of different TIMs.. 57

Table A.1 - Lorentzian peak fitting parameters for the Cu (111) reflection. 78

Table A.2 - Literature values of thermal boundary conductance at uncoated copper–diamond interfaces.. 83

Table A.3 – Steady-state junction temperature as a function of TIM bond-line thickness....... 88

Table A.4 – Sample thickness estimation 89

List of Figures

Figure 1.1: Moore's Law 2
Figure 2.1: Comparison between passive and active cooling methods 7
Figure 2.2: Schematic of an active–passive hybrid cooling configuration. 10
Figure 2.3: Schematic of vibrational density of states. 18
Figure 3.1: SEM micrographs of diamond particles and respective particle size distribution. 29
Figure 3.2: SEM image of the synthetic diamond particles and the corresponding particle size distribution. 30
Figure 3.3: Experimental electrodeposition apparatus for fabricating copper–diamond composites and schematic illustration of the plating setup. 31
Figure 3.4: Optical micrographs showing diamond particle deposition. 33
Figure 3.5: Schematic illustration of the electrodeposited copper–diamond composite configurations 34
Figure 3.6: Schematic illustration of Bragg's law. 36
Figure 3.7: The LED used in this project 37
Figure 3.8: Experimental setup for LED-based heat sink performance testing 38
Figure 3.9: Schematic of diamond-loaded thermal paste preparation 40
Figure 4.1: Planar SEM view of as-deposited composite samples on the side facing the cathode, and microstructures of the cross-sections. 41
Figure 4.2: SEM micrographs of ion-milled electrodeposited Cu–D interfaces 42
Figure 4.3: XRD patterns of the electrodeposited pure copper and copper-diamond composite materials obtained from. 43
Figure 4.4: Heat sink performances of copper-diamond composites. 45
Figure 4.5: Comparison of copper matrix microstructures near diamond particles in uncoated Cu–D composites.. 47
Figure 4.6: Thermal boundary conductance at the Cu-D interface. 49
Figure 5.1: Optical micrograph of the commercial SYY thermal paste. 54
Figure 5.2: Pixel-to-length calibration in ImageJ using the known copper heat sink thickness and representative thickness measurements of the TIM layer 55
Figure 5.3: Measured TIM bond-line thickness for the baseline thermal paste and the higher diamond loadings. 56

Figure 5.4: Transient LED temperature as a function of diamond wt.% for different thermal interface materials 57
Figure 6.1: Schematic illustration of the proposed fabrication route for fin-shaped copper–diamond composite heat sinks. 63
Figure 6.2: Schematic illustration of the proposed mold-assisted electrodeposition route for fabricating fin-shaped Cu–D composites. 64
Figure A.1: XRD pattern of the pure Cu reference sample. 77
Figure A.2: Lorentz peak fit for the Cu (111) reflection. 78
Figure A.3: DEM-predicted effective thermal conductivity of a Cu–diamond composite versus thermal boundary conductance 81
Figure A.4: DEM-predicted composite thermal conductivity versus diamond volume fraction at varying thermal boundary conductance 82
Figure A.5: ImageJ-based manual pore population analysis of SYY thermal paste. 84
Figure A.6: Measured bond-line thickness of the commercial thermal paste under light and hard pressing conditions 85
Figure A.7: Simplified steady-state one-dimensional heat transfer model 86

List of acronyms

AI – Artificial Intelligence

AMM – Acoustic Mismatch Model

CNT – Carbon Nanotube

CPU – Central Processing Unit

CTE – Coefficient of thermal expansion

Cu-D – Copper Diamond

DEM – Differential Effective Medium

FOM – Figure of Merit

GPI – Gas Pressure Infiltration

GPU – Graphics Processing Unit

HPC – High Performance Computing

HTHP – High Temperature High Pressure

HVAC – Heating, Ventilation and Air Conditioning

ICSD – Inorganic Crystal Structure Database

OI – Orientation Index

PCM – Phase Change Material

SEM – Scanning Electron Microscopy

SPS – Spark Plasma Sintering

TIM – Thermal Interface Material

TPU – Tensor Processing Unit

VDOS – Vibrational Density of States

XRD – X-Ray Diffraction

List of symbols

A – Surface area

$C_j(\omega, T)$ – Phonon heat capacity

D – Density of states

d – Interplanar spacing

H – Interfacial thermal conductance

h_c – Convective heat transfer coefficient

h – Thermal boundary conductance

$I_{(hkl)}$ – Intensity of diffraction peak

$I_{0(hkl)}$ – Standard intensity from reference (ICSD) data.

P – Power

Q – Heat flux through interface

q – Heat flux

R – Interfacial thermal resistance

R_θ – Thermal resistance

T – Temperature

V – Volume or volume fraction

v – Phonon speed

v_i – Sound velocity

Z_i – Acoustic impedance

Z_θ – Thermal impedance

$\alpha_{1\rightarrow 2}$ – Transmission coefficient

η – Orientation index

$\eta_{(hkl)}$ – Orientation index

θ – Diffraction angle

κ_{eff} – Effective thermal conductivity

κ_P – Intrinsic thermal conductivity

κ_m – Thermal conductivity of the matrix

λ – X-ray wavelength

ρ – Density

ω – Angular frequency

$\omega_{D,j}$ – Debye frequency

Chapter 1: Introduction and motivation for this research

The increasing demand for faster and more compact computing systems is reflected in Moore's Law, which states that transistor density in integrated circuits doubles approximately every two years, as shown in **Figure 1.1** [1]. This trend has introduced significant thermal management challenges, as increasing power and heat are confined within progressively smaller devices. Over the past two decades, transistor dimensions have shrunk from the microscale to mere tens of nanometers, dramatically raising power density and exacerbating heat dissipation bottlenecks [2], [3], [4]. Furthermore, leading semiconductor manufacturers such as Samsung and TSMC have already commercialized 5 nm technology nodes and recently advanced to 3 nm transistors, marking a new era of ultra-fine devices [5], [6]. While this persistent scaling enables greater transistor density and improved energy efficiency, it simultaneously intensifies the challenge of heat removal.

The significance of these thermal challenges extends beyond conventional computing systems. Emerging applications in flexible electronics and mobile devices also face significant heat removal challenges. The development of materials compatible with transparent and flexible substrates enables innovative display technologies but introduces new thermal management problems. These include localized hot spots in bendable circuits [7] and thermal expansion mismatches in multilayer structures [8], which may ultimately limit device performance and commercial viability [4]. These challenges are worsened by increases in power dissipation resulting from the shrinking size and higher density of transistors and other integrated circuit components [9], [10].

These thermal challenges are also present in artificial intelligence (AI), where processors are pushed to operate at their thermal limits for prolonged periods, significantly intensifying the problem. Modern high-performance central processing units (CPUs) now reach power levels of 200–250 W. In comparison, AI accelerators such as graphics processing units (GPUs) and tensor processing units (TPUs) can exceed 700 W, corresponding to local heat fluxes of roughly 100–200 W/cm^2 depending on die size. Together, these processors can generate system-level heat loads approaching 1 kW [11]. The most critical thermal challenges occur at the die level, where power density and distribution directly impact reliability and cooling effectiveness [4]. What makes AI

workloads particularly demanding, unlike conventional workloads with variable power demands, is their persistent thermal load characteristics. This persistent thermal load has pushed current cooling solutions to their limits, as evidenced by data centers where AI clusters have rapidly progressed to requiring liquid cooling within just five years [12].

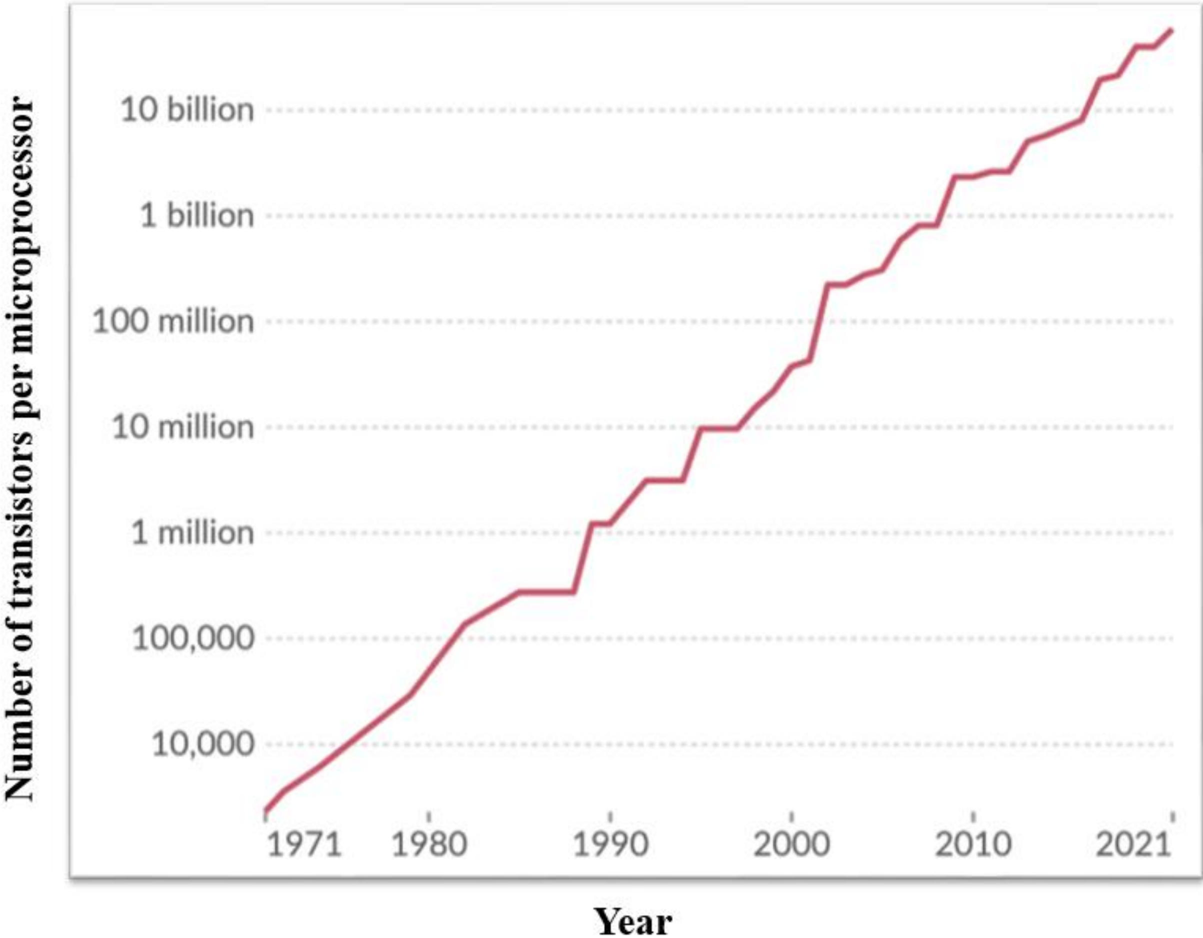

Figure 1.1: Moore's Law showing the doubling of transistors in integrated circuits every two years [13].

Furthermore, recent overheating incidents in consumer electronics illustrate how thermal constraints directly impact user experience. For instance, Samsung's Galaxy S23 series had thermal throttling after prolonged camera use in 2023, with internal temperatures rising to 58°C [14]. Users reported that the case of Apple's M2 Pro MacBook Pro reached 45°C under prolonged loads, resulting in notable performance decreases during 4K video rendering [15]. Additionally, the ASUS ROG Zephyrus G14 displayed CPU temperatures of up to 96°C during AAA gaming sessions, causing emergency shutdowns [16]. The LG G Flex 2, powered by the infamous

Snapdragon 810 (20nm), suffered severe thermal throttling that reduced CPU performance by 40% during benchmark testing, with core temperatures exceeding 80°C [17]. Likewise, Sony Xperia devices utilizing various Snapdragon chipsets (including the Xperia 1 III's Snapdragon 888) implemented aggressive camera throttling during 4K recording, with internal sensors reporting temperatures above 60°C after just 5 minutes of operation [17]. Even popular devices, like the iPhone 15 Pro [18], had thermal problems when they were first released; customers complained that the smartphone overheated when recording videos and charging wirelessly. Together, these occurrences show how difficult it is for contemporary thermal design to strike a compromise between thermal management and performance in small form factors (the physical size and layout constraints of a device).

These widespread occurrences of overheating issues highlight an important issue in thermal design: the challenge of managing increasing power densities within ever-smaller form factors without compromising performance, safety, or user comfort. When thermal management falls short, manufacturers are often forced to implement software-based throttling strategies, which limit device capabilities and degrade user experience. Moreover, thermal failures can reduce the lifespan of electronic components, accelerate material degradation, and increase the risk of system instability or collapse. These real-world examples underscore the urgent and growing need for more effective, scalable, and cost-efficient thermal management solutions in modern electronic devices, especially as the demands for high performance and miniaturization continue to rise.

In consumer devices and industrial systems, where reliability, low maintenance cost, and simplicity are essential, passive heat sinks remain the most widely adopted thermal management solution [19], [20]. Metals such as copper and aluminum are commonly used as heat sink materials due to their high thermal conductivity, machinability, and affordability. Thermal conductivity, a material's ability to transfer heat (SI unit: W/m·K) [21], is a critical parameter for heat sink performance, as it directly affects how efficiently heat can be spread and dissipated away from electronic components. Copper has a thermal conductivity of approximately 400 W/m·K [22], while aluminum offers around 200 W/m·K [23]. However, despite their widespread use, these metals face performance limitations in high-power-density applications. For example, aluminum's

lower conductivity can limit its heat-spreading ability in compact devices, while copper's higher density contributes to added weight, in addition to being costly compared to aluminum.

As devices continue to miniaturize and power densities rise, traditional metal-based heat sinks are no longer sufficient to meet thermal demands without sacrificing design flexibility or efficiency. While active cooling methods [24], such as liquid cooling or vapor chambers, can manage higher heat loads, they also add to system complexity, cost, and power consumption. This highlights the need for higher-performing passive heat sink materials that can handle greater thermal loads. Emerging material systems with superior thermal properties are therefore gaining attention as potential solutions for the next generation of electronic thermal management.

To develop the next generation of passive heat sinks with noticeably better cooling performance, researchers have been concentrating on carbon-based materials and composites [25]. Carbon-based materials like diamond (1500-2500 W/ m·K [26]), graphite (700-2000W/ m·K [27]), graphene (500-1500 W/ m·K [28]), and carbon nanotubes (CNT, 3000 W/ m·K [29]) exhibit exceptionally high thermal conductivities, though many of these values are strongly dependent on crystallographic direction or structural orientation. However, since bulk substrates comprised of these materials have issues with fracture (graphite), mass manufacturing (CNT), cost (CNT, diamond), and negative thermal expansion coefficient (graphene [30]), their use in heat sink applications is extremely limited. In this regard, metal matrix composites (MMCs) reinforced with carbon-based materials offer a potential alternative. MMCs combine the outstanding thermal conductivities of carbon-based materials with the manufacturability of metals. Among the most promising of these are metal-diamond composites, such as copper-diamond (Cu-D) [31] and aluminum-diamond (Al-D) [32]. Diamond, which exhibits the highest known thermal conductivity among natural materials (~2000 W/m·K) [26] can significantly enhance the overall heat transfer performance of a composite when homogenously dispersed within a metal matrix. In applications that cannot be sufficiently cooled by conventional aluminum or copper heat sink materials, such as high-power electronics and laser systems, these materials are particularly appealing because they can offer better cooling performance without requiring additional expensive active cooling systems. However, their broader use remains limited by challenges related to high manufacturing costs, underscoring the need for ongoing research into more economical fabrication methods.

Currently, the most common methods of fabricating MMCs for heat sink applications are through high-temperature, high-pressure (HTHP) manufacturing techniques such as gas pressure infiltration (GPI), squeeze casting, spark plasma sintering (SPS), and hot press sintering. To keep the metal and reinforcements from oxidizing, these procedures need oxygen-free conditions [33], [34]. In addition, high pressures can also cause microstructural defects that weaken the thermal performance: particle fracture, undesired phases, and interfacial cracks [34], [35]. Even though some HTHP-fabricated MMCs exhibit thermal conductivities of 800 W/m·K, these outcomes come at a significant cost in terms of energy consumption and specialized equipment requirement [36]. Therefore, a more economically viable method for fabricating high-quality metal-diamond composite heat sink materials is needed.

Electrodeposition offers a low-temperature and more cost-effective substitute for creating metal matrix composites [37]. Despite being used traditionally for thin coatings, electrodeposition can provide bulk materials with excellent mechanical and corrosion properties with controllable microstructures [38], [39]. Electrodeposited composites offer a promising pathway to integrate high-conductivity reinforcements like diamond into a metal matrix using a relatively low-cost, scalable fabrication process, enabling tailored thermal properties suitable for heat sink applications [40]. However, although electrodeposited Cu-D composites have demonstrated excellent thermal conductivities (500 W/m·K- 850 W/m·K) [41], [42], [43], [44], [45], [46], [47], [48] in laboratory settings, a critical knowledge gap remains in the literature regarding their performance as practical heat sink materials. Most studies focus primarily on microstructural features and intrinsic thermal conductivity, overlooking the evaluation of full heat sink level behavior under realistic thermal loads. As such, the actual thermal performance of these electrodeposited Cu-D composites in real-world applications, including composite design, reliability, and practical heat sink implementation, is still not well understood or validated.

This thesis addresses the gap in understanding the practical heat sink performance of electrodeposited Cu–D composites under realistic operating conditions. The study investigates how different heat sink implementation strategies, including composite structure and the use of thermal interface materials (TIMs), influence the steady-state thermal behavior of electronic devices. Thermal performance is evaluated by measuring the steady-state surface temperature of

each heat sink under a controlled heat flux using a commercial light-emitting diode (LED) and a standardized temperature measurement setup. The results clarify how Cu-D composite design and integration strategies govern heat removal efficiency in thermally loaded systems, while establishing a direct link between microstructural design, interfacial heat transport, and practical device-level performance. The findings demonstrate that electrodeposited Cu-D composites can serve as cost-effective heat sink materials for next-generation electronic devices, provided that interfacial thermal resistance between copper and diamond is mitigated through strategies such as TiC coatings to enhance heat carrier transmission across the interface. Chapter 2 presents a focused review of the relevant literature and effective thermal conductivity models. Chapter 3 describes the fabrication of the composite heat sinks and the experimental methods used for thermal performance evaluation. Chapter 4 discusses the thermal performance of the Cu-D composite heat sinks relative to reference copper systems. Chapter 5 addresses the engineering aspects associated with heat sink attachment and evaluates diamond-modified thermal interface materials. The thesis concludes in Chapter 6 with a summary of key findings, limitations, and recommendations for future work.

Chapter 2: Literature Review

2.1. Heat Removal in Engineering & Electronic Devices

2.1.1 Active and Passive Cooling Strategies

In engineering systems, cooling techniques are generally categorized as either passive or active. Passive approaches depend solely on natural heat transfer mechanisms, whereas active approaches employ externally powered components to enhance/force heat removal. These methods are employed not only in electronics but also across a wide range of other applications. These include industrial machinery such as cutting tools and furnaces, automotive engines and battery systems, building heating, ventilation, and air conditioning (HVAC) and refrigeration systems, as well as spacecraft thermal control systems [49], [50], [51], [52].

The difference between passive and active methods is schematically illustrated in **Figure 2.1**, which compares natural convection, a passive approach where heat is carried away by buoyancy-driven airflow without external assistance through a heat sink. It also contrasts the natural convection with forced convection, an active approach in which a fan or other external source drives airflow to increase the rate of heat transfer from an electronic device.

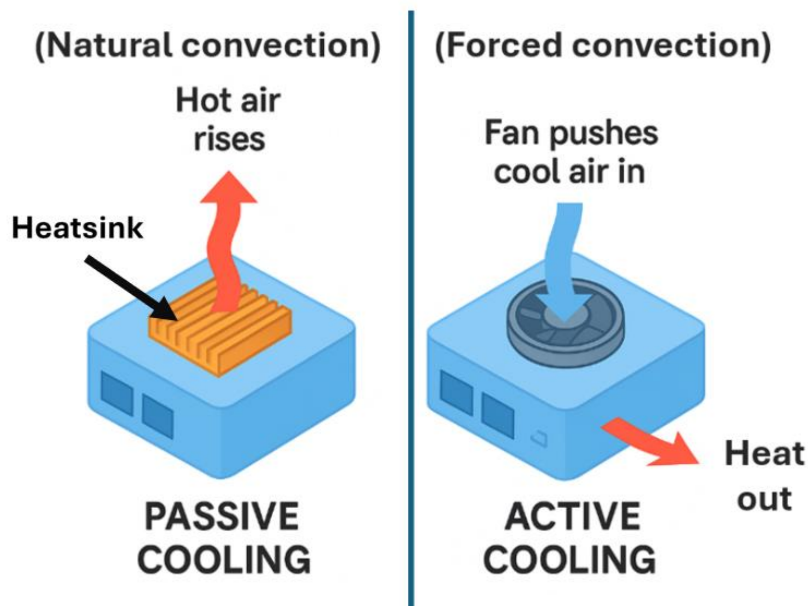

Figure 2.1: Comparison between passive and active cooling methods in electronic devices.

Since passive cooling does not require external power, it is economically appealing for consumer electronics, telecommunications, photovoltaic systems, and LED lighting, where long-term dependability, low maintenance, silent operation, and energy efficiency are essential [53], [54]. Passive cooling is also widely used in building envelopes and architectural design (e.g., thermal mass walls, ventilated facades) to reduce HVAC loads [49], in power electronics cabinets, and in radiative cooling panels for spacecraft [55].

The performance of passive cooling is strongly influenced by the thermal conductivity of the heat sink material, which is a measure of a material's ability to conduct heat, typically expressed in W/m·K. Mathematically, it is defined by Fourier's law of heat conduction:

$$q = -k\nabla T \tag{2.1}$$

where q is the heat flux ($W \cdot m^{-2}$), k is the thermal conductivity, and ∇T is the temperature gradient ($K \cdot m^{-1}$). The negative sign indicates that heat flows from regions of higher temperature to lower temperature, according to the second law of thermodynamics. Aluminum (~200 W/m·K [23]) and copper (~400 W/m·K [31]), are commonly used due to their high conductivity. Aluminum is often chosen for cases that require large heat sinks because its lower density and cost offer an attractive weight-to-performance ratio, even though copper has superior thermal conductivity.

Despite these advantages, passive cooling has notable limitations. Achieving effective natural convection typically requires large surface areas to facilitate sufficient heat transfer to the surrounding environment. However, as devices become smaller and more compact while their heat dissipation continues to increase, providing sufficient surface area for efficient cooling becomes increasingly challenging [56]. In many passive systems, performance can also be restricted by environmental factors such as limited airflow paths, accumulation of dust or debris on heat-dissipating surfaces, and temperature fluctuations in the surrounding medium, which can reduce the overall effectiveness of heat transfer [57].

On the other hand, externally driven active cooling methods improve heat dissipation beyond what can be achieved by natural convection. Common examples include forced-air cooling, liquid

cooling, and two-phase heat transfer devices such as vapor chambers and heat pipes. Forced air cooling, which often employs fans or blowers, remains the dominant approach due to its relatively low cost, straightforward installation, and moderate effectiveness across a wide range of power electronics, industrial cabinet cooling, and automotive radiator applications [50], [58], [59]. However, it is fundamentally limited by air's low heat transfer coefficient, making it insufficient for many modern compact high-power applications.

Liquid cooling offers significantly better thermal performance than air-based methods. This is achieved by circulating liquid coolants with higher heat capacity directly over the heated surfaces. Liquid systems such as cold-plate-based loops, direct-to-chip cooling, and immersion cooling can handle extremely high heat dissipation, making them suitable for demanding applications like data centers, high-performance computing (HPC), and electric vehicles (EVs) [60]. Liquid cooling is also employed in automotive engines for cylinder head and brake system temperature control; in industrial process equipment such as rolling mills; and in spacecraft systems. In the latter, heat pipes and pumped loops dissipate heat into radiators exposed to space [51], [52]. Despite these advantages, liquid cooling introduces added complexity, cost, and potential reliability concerns such as leakage, corrosion, and excessive maintenance requirements, restricting its application to systems where such trade-offs are acceptable.

Two-phase cooling techniques, such as heat pipes and vapor chambers, rely on phase-change phenomena, evaporation at the heat source and condensation at the heat sink, to efficiently transport heat across small temperature gradients. While not the same as full refrigeration cycles (which require compressors and pumps), these systems use the latent heat of vaporization to passively move thermal energy without mechanical pumping. This ability to transfer large amounts of heat with minimal temperature difference has made them increasingly popular in compact electronic devices, where traditional active methods are impractical due to size or reliability constraints [52]. However, two-phase systems can have limitations related to orientation dependence and maximum allowable heat flux, and they are often more expensive and challenging to integrate than liquid cooling solutions [61].

2.1.2 Hybrid Cooling Approaches

Hybrid cooling combines aspects of both passive and active techniques to optimize thermal performance and cost. By leveraging the strengths of each approach, hybrid systems can overcome the limitations of purely passive or purely active methods. A common example is a heat sink integrated with fans, which uses the extended surface area of the heat sink (passive) while enhancing air flow with forced convection (active) [62] as shown in **Figure 2.2**. This combination is widely used in desktop CPUs, GPU cooling, and industrial control cabinets [63].

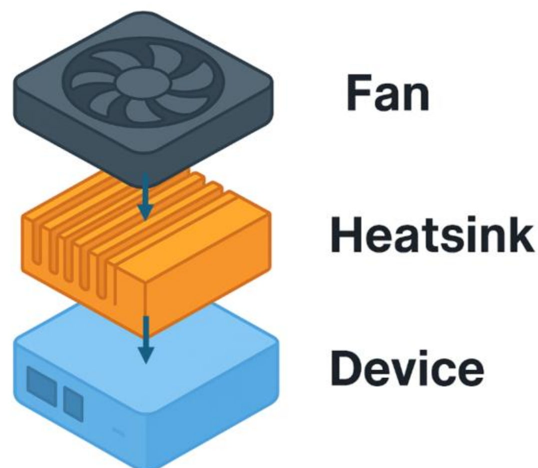

Figure 2.2: Schematic of an active–passive hybrid cooling configuration, where a fan provides forced convection over a finned heat sink mounted on top of the device.

Other noteworthy hybrid solutions are liquid-cooled heat sinks, which effectively transfer heat away from the source by maximizing contact surface through coolant channels embedded in a solid metal block. Efficient and compact cooling is critical in high-power laser systems, electric vehicle inverters, and aerospace power electronics, where these solutions are frequently applied [51], [52]. Thermal management systems in electric batteries also use hybrid strategies, combining active liquid loops with passive heat spreaders made from high thermal conductivity materials such as aluminum and copper; to maintain uniform temperature distribution across cells [64]. Hybrid cooling strategies are expected to gain wider adoption, driven by industry demands for compact, reliable, and energy-efficient solutions. All cooling strategies discussed in this section are summarized in **Table 2.1**, along with representative applications and key considerations such as cost, complexity, and reliability. This comparison demonstrates that no single approach is

universally optimal, and that system-specific requirements ultimately determine the most suitable thermal management strategy.

Given these constraints, the choice between active and passive cooling depends on system requirements, cost, complexity, and reliability considerations. These inherent limitations highlight the need for improved heat sink materials and designs capable of achieving higher thermal performance within compact form factors. This thesis focuses on developing Cu-D composites with high thermal conductivity for passive cooling components such as heat sinks and heat exchangers.

Table 2.1 - Summary of Cooling Methods, Applications, and Key Considerations

Cooling Method	Type	Example Applications	Key Considerations
Heat sink (natural convection)	Passive	LED lighting, telecommunications equipment, building-integrated passive cooling panels	Low cost, silent operation, no power consumption; limited performance in high heat flux applications
Heat sink + fan (forced-air)	Active	Desktop CPUs, GPU cooling, industrial control cabinets	Low to moderate cost, simple design, moderate performance; requires power and moving parts
Liquid cooling (cold plates, immersion)	Active	Data centers, HPC servers, electric vehicle battery systems, high-performance automotive engines	High thermal performance, scalable; higher cost, potential leakage and maintenance issues
Heat pipes / vapor chambers	Active / Passive assist	Laptops, smartphones, aerospace avionics, spacecraft thermal control	Compact, effective over small temperature gradients; orientation-sensitive, higher manufacturing cost
Hybrid: liquid-cooled heat sink	Hybrid	High-power laser systems, EV inverters, aerospace power electronics	Combines high capacity with compact size; high cost, complex integration
Hybrid: liquid loop + passive heat spreaders	Hybrid	Battery thermal management systems	Improved temperature uniformity; added system complexity

2.2 Interface Bonding Between Heat sinks and Components

The effectiveness of heat transfer at the interface between the heat sink and the heat-generating component is equally critical as the heartsink's bulk thermal conductivity in determining its overall cooling performance. If interfacial thermal resistance (R), the resistance to heat flow across the junction between two materials, is high, which can result from surface roughness or poor

mechanical contact, even high-performance heat sinks may struggle to transfer heat effectively. Mathematically, R can be expressed as:

$$R = \frac{\Delta T}{Q} \tag{2.2}$$

where ΔT is the temperature difference across the interface and Q is the heat flux through it ($W \cdot m^{-2}$). R is expressed in $m^2 \cdot K \cdot W^{-1}$.

The reciprocal of R is the interfacial thermal conductance (H), which is defined as:

$$H = \frac{1}{R} \tag{2.3}$$

with units of $W \cdot m^{-2} \cdot K^{-1}$. To reduce R *(or equivalently, to improve H)*, thermal interface materials (TIMs) are frequently used to enhance contact and promote effective heat transfer. In addition to selecting an appropriate TIM, the mechanical attachment method, such as clamping, bolting, or spring-loading, also plays a crucial role in maintaining consistent, low-resistance contact over the device's operational lifetime. This section focuses on TIM types and bonding techniques used for heat sink materials in electronic devices.

2.2.1 Thermal Interface Materials (TIMs)

Thermal interface materials (TIMs) are employed to mitigate the interfacial resistance that arises from microscopic gaps and surface roughness at the contact between a heat source and a heat sink. These imperfections can trap air pockets, which have an extremely low thermal conductivity (~0.024 W/m·K) [65] [66], thereby becoming an additional source of thermal resistance. While certain surface textures may increase contact area, excessive roughness often worsens the problem. By filling these voids and creating a more uniform interface, TIMs enhance thermal contact and reduce interfacial thermal resistance, making them essential for reliable heat dissipation in electronic devices.

Commonly used TIMs include:

- Thermal Tape: this is one of the least expensive heat sink attachment options, typically made from a pressure-sensitive adhesive on both sides of a thermally conductive carrier polymer, most often polyimide (Kapton). Thermal conductivities for commercial thermal tapes typically range from approximately 0.3 to 1.5 W/m·K, depending on the carrier polymer and filler content. It bonds to surfaces when pressed into place, without requiring heat or curing, and works well with low-mass heat sinks and low-power dissipating components. Market prices are around US $10 for a 32 m roll, which translates to less than $0.01 per cm² in typical use, making it highly cost-effective for small-scale applications [67].
- Thermal conductive adhesives (TCAs): TCAs are typically epoxy-based materials filled with conductive particles. Silver is the most common filler due to its high thermal conductivity (400 W/ m·K [68]), although nickel, copper, and carbon fillers are also used. Though silver has an intrinsic thermal conductivity of approximately 400 W/m·K, the effective thermal conductivity of commercial TCAs typically ranges between 1 and 7 W/m·K due to filler loading limits and polymer matrix resistance. They provide strong mechanical bonding and moderate thermal performance. However, they can be difficult to rework and may degrade over repeated thermal cycles [69]. Compared to thermal tapes, thermally conductive adhesives (TCAs) are generally more expensive. Commercial products such as MG Chemicals cost approximately US $25 for a 6 mL kit. Assuming a representative thermally conductive adhesive bond-line thickness of 50–100 µm, based on reported values for commercial thermal adhesives, this volume would cover approximately 600–1200 cm², corresponding to an estimated cost of approximately $0.02–0.04/cm² Additionally, TCAs typically require preparation prior to use, as most are supplied as two-part liquid formulations that must be thoroughly mixed before application and subsequently cured for durations ranging from 2 to 48 hours [67]. Unlike thermal greases or pastes, TCAs cure into a solid bond, providing permanent attachment rather than a removable interface layer.
- Thermal grease/paste, and gels: they are typically composed of a silicone or synthetic oil base filled with thermally conductive particles such as zinc oxide, aluminum oxide, boron nitride, or silver. Commercial thermal greases typically exhibit thermal conductivities in the range of ~1 to 8 W/m·K, with higher-performance formulations exceeding 10 W/m·K.

These materials conform to microscopic surface irregularities when compressed, achieving very low bond-line thickness and low interfacial resistance. However, they can "pump-out," meaning the compound is gradually displaced from the interface due to thermal expansion, vibration, or mechanical stress, which reduces its effectiveness and increases thermal resistance. Prices vary depending on filler type and quality; for example, a 3.5 g tube of Arctic Silver 5 (silver-filled) costs about US $6-8, translating to roughly $0.015-0.020 per cm², while budget silicone-based greases can be as low as $0.0025-0.005 per cm² [70], [71].

- Phase-change materials (PCMs): these materials are used as thermal interface layers and are solid at room temperature. At operating temperatures, typically between 45 °C and 70 °C, they soften or melt slightly, allowing them to flow into microscopic surface gaps and improve interface contact without the need for manual spreading. Once cooled, they re-solidify, maintaining the formed contact and reducing interfacial thermal resistance. PCMs are typically made from waxes, thermoplastic polymers, or paraffin-based compounds blended with thermally conductive fillers such as aluminum oxide, boron nitride, or graphite to achieve conductivities in the range of ~1–6 W/m·K. They are commonly supplied as pre-applied coatings on heat sink bases, or in thin film form (0.1–0.5 mm thick) that can be cut to size and placed between components. Their advantages include reusability over multiple thermal cycles and clean handling compared to greases; however, their performance can degrade if the material repeatedly exceeds its phase-change temperature or undergoes filler separation over time. In terms of cost, standard paraffin-based PCM sheets average about US $0.10–0.20 per cm², while high-performance graphite-enhanced or metallic-filler PCMs can range from US $0.30–0.60 per cm² [69], [71].
- Thermal pads (gap fillers): these are pre-formed, solid sheets, most made from silicone elastomers. They are embedded with thermally conductive fillers such as ceramic particles (e.g., aluminum oxide, boron nitride) or, in higher-end products, graphite or phase-change materials. These soft, compliant materials deform under slight pressure, allowing them to conform to surface irregularities and fill air gaps, which improves thermal contact between components. While easier to install, remove, and clean than grease, they generally have higher bulk and interfacial thermal resistance, making them more suitable for simple or

low-power applications. Thicknesses typically range from 0.5 to 5 mm, with thermal conductivities spanning ~1-12 W/m·K depending on filler type. Costs vary widely: basic silicone-ceramic pads average around US $0.15-0.25 per cm², while high-performance graphite or PCM-based pads can exceed US $0.50-0.80 per cm² [65].

- Advanced carbon-based TIMs (graphene or CNT-enhanced composites): these materials leverage nanomaterials to dramatically increase thermal conductivity by creating highly conductive pathways within the base medium. Unlike conventional thermal pads, which are relatively thick, compliant sheets designed mainly to fill air gaps, carbon-based TIMs are typically formulated as greases, gels, or thin coatings that operate at much smaller bond-line thickness. Reported thermal conductivities for graphene-enhanced greases commonly exceed 5 W/m·K under optimized filler loading [72]. Moreover, a graphene-enhanced grease has been reported to achieve interface resistances of ~3.2–4.3 mm²·K/W, comparable to or better than many commercial TIMs, while increasing overall thermal conductivity by a factor of ~17 at moderate loadings (~10 vol%). Despite these promising results, such materials are still largely at the research and prototype stage, with limited commercial availability. Their adoption is currently hindered by challenges in large-scale manufacturing, dispersion uniformity of nanofillers, long-term stability, and cost, which can be significantly higher than conventional TIMs [26].

2.2.2 Bonding Techniques

Bonding, in the context of heat sinks, refers to the mechanical method used to physically secure the heat sink to the heat-generating component. Bonding methods provide that pressure, holding the two parts together to maintain reliable contact over time. In practice, TIMs and bonding are not alternatives but are used together, TIMs improve the quality of the thermal path, while bonding ensures that this path remains stable under operational conditions. The chosen bonding method directly affects contact pressure, interface uniformity, mechanical stability, and the long-term reliability of the assembly under mechanical stresses and thermal cycling. An effective bonding process minimizes the formation of air gaps, which would otherwise increase interfacial thermal resistance, thereby ensuring consistent heat transfer throughout the device's operational lifetime.

Common bonding techniques in electronics cooling include:

- Mechanical fastening: In both consumer and industrial electronics, mechanical fastening (such as spring-loaded Z-clips, clamps, or screws) is the most popular technique for securing heat sinks. To keep the heat sink and device in contact, these systems use regulated pressure. They are inexpensive, reusable, and adjustable to different heat sink shapes. Uneven pressure distribution, however, may cause localized separation and eventually lower the thermal performance [67], [74].
- Soldering: Soldering creates a metallurgical connection between the component and the heat sink base, resulting in an extremely stable, low-resistance interface. Tin-based or indium-based alloys, chosen according to mechanical and thermal requirements, are commonly used. Although soldering provides strong mechanical integrity, it requires relatively elevated processing temperatures, typically in the range of ~180–250 °C for tin-based solders and ~150–200 °C for indium-based solders, making it unsuitable for electronics that are sensitive to heat exposure [75].
- Brazing: Brazing is another bonding method. It is similar to soldering but uses filler metals like silver-copper alloys at greater temperatures. For larger or heavier heat sinks, brazing is usually utilized in applications that require outstanding mechanical strength and stability at high temperatures. Although highly reliable, the elevated processing temperatures (often above 450 °C) can risk damaging delicate electronic components, so careful temperature control is required during assembly [76].
- Diffusion bonding: Diffusion bonding is a solid-state joining technique that allows for atomic-level bonding by pressing two surfaces together for a long time at high temperatures. This method creates hermetic joints that are highly robust and have very little interfacial resistance. However, it is typically saved for high-reliability or aerospace-grade systems because it is a labor-intensive procedure that requires accurate surface preparation [77].

In this thesis, the focus will be on evaluating a range of thermal interface materials (TIMs) for Cu-D composite heat sinks, including commercially available options such as thermal tapes and thermal pastes. Their performance will be systematically compared under controlled conditions to assess their effectiveness in enabling efficient heat transfer. In addition to testing these established materials, this work will also involve the development of a custom TIM, where diamond particles

are incorporated into a conventional thermal paste to examine their effect on thermal performance. This modification is intended to better match the high thermal conductivity of Cu-D composites and could provide insights into designing TIMs tailored for advanced composite heat sinks.

2.3 Metal-Diamond Composite heat sink materials via HTHP methods

Metal–diamond composites have been extensively studied as viable candidates for heat sink applications, offering high thermal conductivity values suitable for enhancing heat removal in high-performance microelectronics. Diamonds are incorporated into metallic matrices using various high temperature/high-pressure (HTHP) processing techniques, including gas pressure infiltration (GPI), spark plasma sintering (SPS), and vacuum hot pressing (VHP). Particle size, diamond content, matrix selection, and interface quality all have a significant impact on reported thermal conductivities. The primarily material systems have been copper–diamond, silver–diamond, and aluminum–diamond composites [78], [79], [80], [81], [82], [83].

Silver exhibits the highest intrinsic thermal conductivities of all metals (~430 W/m·K) [68]. When combined with diamond, silver–based composites consistently show high thermal conductivities, often above 750 W/m·K. For instance, Ag–Si–diamond composites with ~57 vol.% diamond achieved ~782 W/m·K [84], while pure Ag–diamond composites with similar diamond volume fractions reached ~847 W/m·K [85]. Despite their high thermal conductivity, silver–diamond composites are not favored for practical applications because silver is expensive and the cost of maintaining a silver-plating bath limits its industrial use.

Aluminum's low density (2.7 g/cm^3) and affordability make it a desirable material for lightweight heat sink applications, despite its modest intrinsic thermal conductivity (~200 W/m·K) [68]. Its thermal conductivity is usually increased by a factor of two to three when diamond reinforcement is implemented. While infiltration processes achieve high thermal conductivities (550–700 W/m·K), particularly at diamond loadings beyond ~55 vol.%, these values exceed those obtained by conventional SPS and sintering, which typically yield 360-430 W/m·K. This significant improvement in conductivity is attributed to the formation of intermetallic Al_4C_3, which strengthens the bond between the diamond and aluminum matrix [86], [87].

A notable approach to lower interfacial resistance at the metal-diamond interface in composites is the utilization of interfacial intermetallic carbides [88], [89], [90], [91]. Rather than relying solely on the intrinsic conductivity of the metal, intermetallic carbides such as TiC, WC, and Al_4C_3 provide vibrational spectra that overlap with both the metal matrix and diamond, thereby facilitating phonon transmission across the otherwise mismatched interface. As illustrated in **Figure 2.3**, the vibrational density of states (VDOS) of pure metals is concentrated at relatively low frequencies compared to the high-frequency modes of diamond. The addition of an interfacial carbide introduces intermediate vibrational states, thereby creating a phonon bridge that enhances thermal boundary conductance between the metal matrix and the diamond [92].

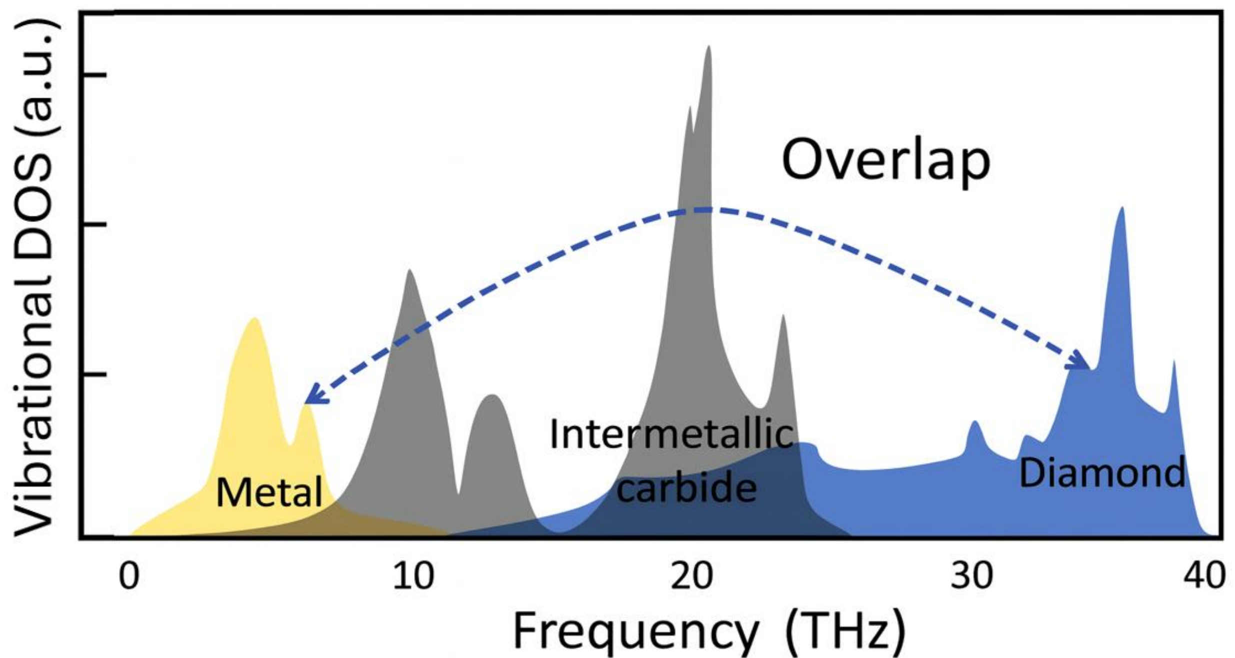

Figure 2.3: Schematic of vibrational density of states (VDOS) for metal, intermetallic carbide, and diamond.

The importance of such interfacial carbides extends directly to practical coating strategies used in Al–diamond composites. By deliberately introducing carbide-forming elements, researchers have been able to enhance thermal conductivity. For example, Zhu *et al*. reported that uncoated infiltration-based composites reached ~727 W/m·K, but their conductivity decreased significantly upon thermal hysteresis. After 1000 thermal cycles, W-coated diamonds stabilized the composite near 615 W/m·K due to the formation of Al_5W on diamond particles, while WC-coated composites retained ~703 W/m·K but showed reduced stability with further cycling. Likewise, Kondakci and

Solak demonstrated that SiC-coated diamond/Al composites-maintained conductivity above 450 W/m·K up to 200 °C, reaching ~528 W/m·K compared with ~376 W/m·K for uncoated counterparts. These results highlight the critical role of surface coatings in preserving long-term stability and optimizing thermal conductivity in Al–diamond systems [93], [94]. A summary of reported values from different fabrication methods and coating strategies is provided in **Table 2.2**, highlighting the impact of both the processing route and interfacial design on the achievable thermal conductivity and stability of Al–diamond composites.

Table 2.2 - Reported thermal conductivities of Al–diamond composites. (TC = thermal conductivity).

Diamond Coating	Method	Diamond vol.%	Particle size (µm)	TC range (W/m·K)	Notes	Ref.
Uncoated	SPS / Sintering	40–50	165–200	360–431	Powder-based, moderate bonding	[95], [96]
	Infiltration	58–63	98–395	550–676	High TC, limited stability due to Al_4C_3	[35], [91], [97], [98]
WC coated	Infiltration	~60	100–200	703–727	WC less stable under cycling	[94]
SiC coated	Infiltration	55–60	100–200	~528	Suppresses Al_4C_3	[93]

Copper's high intrinsic thermal conductivity (~400 W/m·K)[68], reasonable cost, and widespread use in electronics and thermal management applications makes it a frequently studied matrix. Due to copper's poor wettability on diamond surface, interfacial bonding quality can vary significantly. As a result, SPS and sintering methods report a wide range of thermal conductivities, from as low as ~185 W/m·K in poorly bonded systems to ~750 W/m·K when improved interfaces are achieved. Infiltration methods generally provide superior results, reaching 230–900 W/m·K, particularly when coarse diamond particles are used, since their lower surface-to-volume ratio reduces the total interfacial resistance. Interface control and alloying have pushed these values further: Li *et al*. demonstrated ~930 W/m·K using Cu–Zr alloys, where a thin ZrC interlayer (~400 nm) suppressed phonon scattering and enhanced bonding at Cu-D interfaces [99]. Similarly, WC-coated composites by infiltration have reported ~900 W/m·K at ~62 vol.% diamond [85], while ultra-high-pressure infiltration (2 GPa) with Cu–Ti alloys produced ~900 W/m·K through the formation of a TiC interfacial layer [100]. These results are summarized in **Table 2.3**, which compiles reported thermal conductivities of Cu-D composites produced by different processing routes and interfacial modification strategies. These observations, consistent with findings in Al–diamond composites, confirm that carbide coatings and alloying strategies are essential for optimizing both interfacial bonding and thermal transport in Cu-D systems.

Although diamond reinforcement has been shown to significantly increase the thermal conductivity of metallic matrices through powder-based sintering, spark plasma sintering, and infiltration, these processes have some challenges. Achieving maximum conductivities often requires extreme processing conditions, specialist equipment, or specific alloying additions (e.g., Ti, Zr) to promote carbide interlayers [32] which drives up cost and reduces economic viability. Furthermore, long-term reliability can be affected by interfacial challenges such as poor wettability of copper on diamond [101], instability of thermal transport at the metal/diamond boundary due to weak phonon coupling and interfacial degradation [32], and phase degradation, for example, hydrolysis of Al_4C_3 in Al-diamond systems, where exposure to moisture leads to the formation of $Al(OH)_3$ and CH_4, degrading interfacial stability [102].

Table 2.3 - Reported thermal conductivities of Cu-D composites. (TC = thermal conductivity)

Coating type	Method	Diamond vol.%	Particle size (µm)	TC range (W/m·K)	Notes	Ref.
Uncoated	SPS / Sintering	5–70	50–110	185–742	Limited by poor wettability	[80], [103], [104], [105], [106], [107], [108]
	Infiltration	65–95	70–550	230–900	Best uncoated results	[88], [100], [109], [110]
Carbide-coated	SPS / Sintering	5–60	75–156	285–654	Cu, TiC, Cr_3C_2, ZrC coatings	[80], [103], [104], [105], [107], [111]
	Infiltration	60–65	70–420	550–700	Cr_3C_2, B, SiC coatings	[85], [88], [112]
	Infiltration	62	420	900	WC-coated	[85]
Alloyed Cu matrices	Pressure infiltration	~61	~100	930	Cu–Zr alloy, optimized ZrC interlayer	[99]
	High-temp infiltration	60–65	~100	~900	Cu–Ti alloys, ultra-high pressure (2 GPa)	[99]

2.4 Electrodeposition of copper-diamond composites

Electrodeposition has emerged as a promising alternative to traditional high-temperature high pressure fabrication techniques such as infiltration, hot pressing, and spark plasma sintering. The main advantage is that it can create Cu-D composites at ambient conditions at room temperature. Through electrodeposition, diamond particles suspended in the electrolyte can be uniformly embedded within a copper matrix. However, the resulting microstructure and thermal performance of the composite are highly dependent on processing parameters, such as bath chemistry, current density, temperature, and particle size distribution, which govern the interfacial bonding and

overall thermal conductivity. Several studies have reported notable promising thermal conductivity values via electrodeposition techniques. Cho *et al*.[42] showed that with 34.7 vol.% loading, TiC-coated particles increased the conductivity to 557 W/m·K, whereas uncoated diamonds produced 454 W/m·K at 68.2 vol.%. Wu *et al.* [113] created void-free uncoated Cu-D composites with values of about 615 W/m·K. By using a bimodal distribution of diamond particles to increase packing density, they were able to improve this from 615 W/ m·K to 651 W/m·K [43]. Zhou *et al*. used electrodeposition to produce Cu-D composite foils with tungsten-coated micro-diamond particles. The composites had a thermal conductivity of 509.7 W/m·K under ideal processing conditions (diamond size 100/120 μm, current density 133.3 mA/cm^2), which was a 28.4% improvement over pure copper (397 W/m·K). However, the thermal conductivity progressively dropped after repeating thermal cycling between 196 °C and 200 °C. 13.5% loss after 5 cycles, remained comparatively steady for 15 cycles, and then dropped rapidly to 306.5 W/m·K (60.5% of the initial value) after 20 cycles [114]. Luo *et al*. [115] created single-layer composites reaching 588 W/m·K. Arai and Ueda [46] achieved 662 W/m·K at 61 vol.% diamond by electrodepositing dense Cu-D composites at room temperature and pressure. Their careful potentiostatic control, which reduced hydrogen evolution during deposition, was attributed to this high conductivity. The copper matrix completely filled the spaces between diamond particles by inhibiting the development of H_2 bubbles. Particle size effect was also discovered by Wu *et al.* [41], who reported a record 846 W/m·K with 400 μm particles, while smaller particles exhibited less noticeable thermal conductivity increases. A summary of these reported values is provided in **Table 2.4**, which consolidates the thermal conductivities of electrodeposited Cu-D composite. These results indicate that electrodeposition can produce Cu-D composites with thermal conductivities on par or even higher than those achieved by high-temperature procedures.

Table 2.4 - Reported thermal conductivities of electrodeposited Cu-D composites.

References	Particle size / coating	Diamond vol.%	Thermal Conductivity (W/m·K)
Cho *et al*. [42]	400 µm uncoated; TiC-coated	68 / 34.7	454/557
Wu *et al*. [113]	100 µm, uncoated	~40	615
Wu *et al*. [43]	30 µm + 100 µm (bimodal)	~45	651
Luo *et al*. [115]	100 µm, uncoated	36	588
Zhou *et al*.[114]	100–120 µm, W-coated	–	509.7 → 306
Arai & Ueda [46]	230 µm, uncoated	61	662
Cho *et al*. [44]	66 µm, uncoated	42	222
Wu *et al*. [41]	400 µm, uncoated	–	846

Using electrodeposition, high-performance Cu-D composites with thermal conductivities between 450 and more than 800 W/m·K can be created. Reported values vary widely due to differences in surface treatments, plating conditions, and diamond particle size. The achievement of such high conductivities under room-temperature and ambient-pressure conditions highlights electrodeposition as an economically viable alternative to HTHP-based methods for fabricating next-generation electronic heat sink materials.

2.5 Metrics for Measuring Heat sink Performance

The evaluation of heat sink performance requires standardized parameters that capture both material-level properties and system-level thermal response. Heat sink performance is best evaluated using standardized engineering metrics that reflect real operating conditions. Rather than relying only on intrinsic material properties such as thermal conductivity, these metrics quantify how effectively a heat sink removes heat under applied power and defined boundary conditions.

Heat sink performance is frequently evaluated using a variety of techniques, each of which focuses on a distinct facet of heat dissipation.

One of the most widely used metrics is thermal resistance (R_θ), which has already been defined in Section 2.2 as the ratio of temperature difference to applied heat load:

$$R\theta = \frac{\Delta T}{Q} \tag{2.4}$$

where ΔT is the temperature rise between the junction and the reference point (ambient, case, or substrate), and Q is the applied heat load. In the context of heat sink testing, this relationship is typically expressed as junction-to-ambient ($R_{\theta JA}$), junction-to-case ($R_{\theta JC}$) or case-to-ambient ($R_{\theta CA}$), depending on which part of the thermal path is being evaluated. These parameters consolidate the combined effects of conduction through heat sink, interfacial resistance at the TIM layer, and convection to the environment, and are therefore widely adopted for both datasheet specifications and comparative evaluation of heat sink performance [65], [115].

Thermal impedance (Z_θ) is used to characterize transient thermal response in addition to steady-state behavior. In contrast to thermal resistance, which is measured at thermal equilibrium, Z_θ records the time-dependent temperature change as power is applied or removed. It is defined as:

$$Z\theta(t) = \frac{\Delta T(t)}{P} \tag{2.5}$$

Here, $\Delta T(t)$ represents the transient temperature difference as a function of time, and P is the applied or dissipated power during heating or cooling. In high-power electronics such as GPUs or IGBTs operating under non-steady duty cycles. Z_θ provides critical insight into how a heat sink manages pulsed loads or abrupt variations in heat generation [58]. These dynamics are often modeled using equivalent thermal RC networks, which allow prediction of system behavior under dynamic operating conditions.

Reporting the temperature increase per unit power *(ΔT/P)* is another approach. In experimental settings where distinguishing between junction, case, and ambient contributions, is not feasible, this metric can be used. It offers a simple way to compare the heat sinks of various materials or geometries under the same heating situation, despite conceptually being similar to thermal resistance [56], [59].

In addition to resistance and impedance, composite metrics are also employed for comparative evaluations, particularly when new materials are benchmarked against conventional solutions. These metrics extend beyond absolute values to provide normalized or weight-sensitive measures of performance. Thermal performance ratio (TPR) [117] is a normalized metric used to compare thermal conductivity against a standard reference material, usually aluminum. It is expressed as:

$$TPR = \frac{k(material)}{k(Aluminum)} \tag{2.6}$$

where κ *(material)* is the thermal conductivity of the material under study, and κ (*Aluminum)* is the thermal conductivity of aluminum. A *TPR* greater than one indicates superior performance relative to aluminum. This simple normalization is used in the evaluation of advanced heat spreader materials.

Figure of merit (FOM) provides a performance measure that accounts for both conductivity and density, making it especially useful in mass-sensitive applications. It is defined as:

$$FOM = \frac{k}{\rho} \tag{2.7}$$

where κ is thermal conductivity and ρ is material density. Higher FOM values indicate better thermal transport per unit mass, which is critical in aerospace and electronic packaging applications [118].

Overall, these quantitative techniques provide a framework for evaluating heat sink performance. Among them, thermal resistance remains the most widely adopted industry standard. *In this thesis,*

junction-to-ambient thermal resistance ($R_{\theta JA}$) is used as the primary metric, since it directly captures the overall cooling effectiveness of Cu–diamond composite heat sinks under practical operating conditions.

2.6 Predictive Models for Effective Thermal Conductivity of Composites

Analytical models play a critical role in establishing theoretical expectations for heat transport in particle-reinforced metal matrix composites. Since diamond possesses an exceptionally high intrinsic thermal conductivity relative to copper, the rule of mixture predicts that increasing the diamond volume fraction should enhance the overall composite conductivity. However, this improvement is strongly dependent on interfacial heat transfer. Two standard models for the thermal conductivity of composites are explained in this section.

2.6.1 Hasselman–Johnson (H–J) Model

The mathematical description of thermal transport in composite materials originates from Maxwell's treatment of spherical inclusions embedded within a continuous matrix. Maxwell's model assumes perfect thermal contact between the matrix and reinforcement, implying infinite thermal boundary conductance. As a result, it commonly overestimates the effective thermal conductivity of composites containing highly conductive particles [119].

Hasselman and Johnson extended Maxwell's formulation by incorporating finite interfacial thermal resistance and solving the steady-state heat conduction equation. In the Hasselman-Johnson model, the effective thermal conductivity of composite is given [120]:

$$\kappa_c = \kappa_m \frac{2\left(\frac{\kappa_p}{\kappa_m} - \frac{\kappa_p}{hr} - 1\right)V_p + \frac{\kappa_p}{\kappa_m} + \frac{2\kappa_p}{hr} + 2}{\left(1 - \frac{\kappa_p}{\kappa_m} - \frac{\kappa_p}{hr}\right)V_p + \frac{\kappa_p}{\kappa_m} + \frac{2\kappa_p}{hr} + 2} \tag{2.8}$$

where κ_c is the composite thermal conductivity, κ_m is the matrix thermal conductivity, κ_p is the particle thermal conductivity, h is the thermal boundary conductance between the matrix and the particles, r is the particle radius, and V_p is the particle volume fraction. By incorporating interfacial conductance, the Hasselman–Johnson model provides more realistic predictions for metal–

diamond composites, where heat carrier transmission mechanism at the interface introduces significant thermal resistance.

In the limiting case where $h \rightarrow \infty$, the interfacial resistance vanishes and the equation reduces to the classical Maxwell model [119] given by:

$$\kappa_c = \kappa_m \frac{\kappa_p + 2\kappa_m + 2V_p(\kappa_p - \kappa_m)}{\kappa_p + 2\kappa_m - V_p(\kappa_p - \kappa_m)} \tag{2.9}$$

This equation is based on effective medium theory, where a two-phase composite is treated as a homogeneous material with an equivalent thermal conductivity.

2.6.2 Differential Effective Medium (DEM) Model

While the Hasselman–Johnson model is well suited for composites containing dispersed particles, it does not fully capture increased particle–particle interactions at higher loadings. The DEM model addresses this by incrementally adding particles and continuously updating the effective thermal conductivity. The Differential Effective Medium (DEM) model extends the Bruggeman approach by establishing a differential relationship between the effective thermal conductivity and the volume fraction of the dispersed phase [121].

For spherical inclusions, the DEM formulation can be expressed implicitly as:

$$1 - V_P = \frac{\kappa_p - \kappa_c}{\kappa_p - \kappa_m} \left(\frac{\kappa_c}{\kappa_m}\right)^{-\frac{1}{3}} \tag{2.10}$$

The influence of thermal boundary conductance and particle volume fraction on effective thermal conductivity is further illustrated in Appendix A (**Figure A.4**).

Since the original Bruggeman framework neglects interfacial thermal resistance, the particle conductivity is replaced with an effective particle conductivity defined as [122]:

$$\kappa_{eff} = \frac{\kappa_p}{1+(\frac{\kappa_p}{hr})} \tag{2.11}$$

which explicitly accounts for finite thermal boundary conductance. As $h \to \infty$, the effective particle conductivity approaches the intrinsic particle conductivity.

Together, the Hasselman–Johnson and DEM models demonstrate that the influence of diamond volume fraction on composite thermal conductivity is strongly governed by interfacial heat transport. When thermal boundary conductance is insufficient, the high intrinsic conductivity of diamond may not translate into improved composite performance. Conversely, once adequate interfacial conductance is achieved, increasing diamond content can produce substantial gains in effective thermal conductivity.

Chapter 3: Experimental Procedures

3.1 Materials and Methods

Copper–diamond composite materials were electrodeposited in an acidic copper plating bath containing diamond particles supplied by DEV Industrial Corp. (Boca Raton, FL, USA). Two types of diamond particles were used for fabricating the composite heat sinks evaluated in Chapter 4: synthetic diamond particles and TiC-coated diamond particles, both with a nominal particle size of approximately 400 µm. Representative morphology and particle size distribution of these particles are shown in **Figure 3.1** based on statistical measurements of 250 randomly selected particles. The average particle size was 405 µm with a standard deviation of 40 µm.

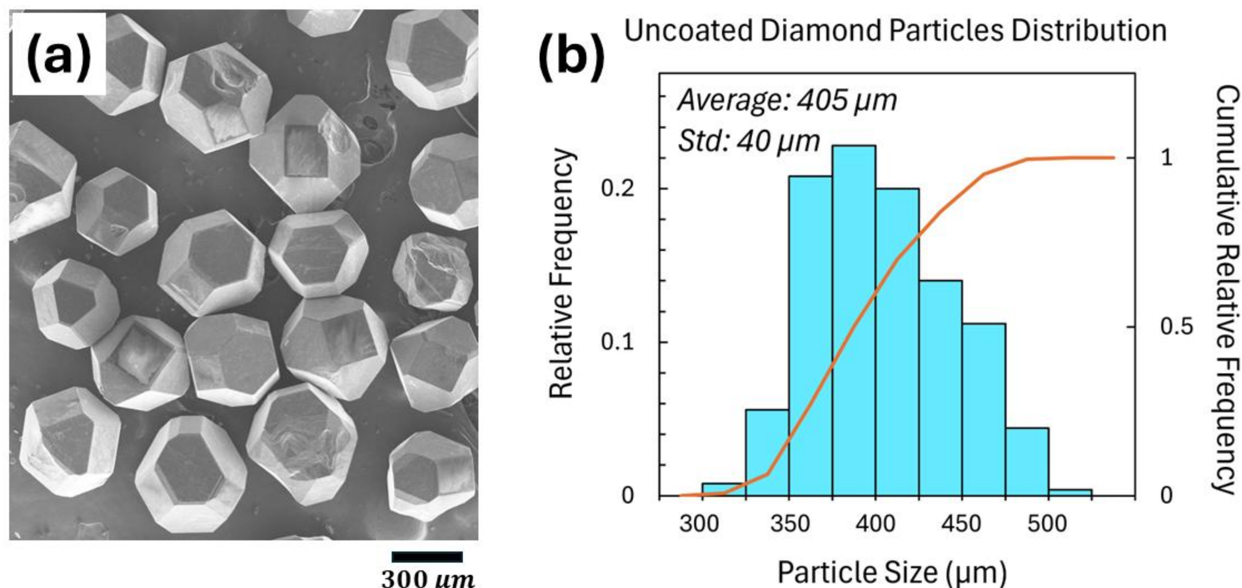

Figure 3.1: (a) SEM micrographs of diamond particles and (b) respective particle size distribution.

Prior to electrodeposition, both diamond particles were etched in a 10 vol.% HNO_3 solution to remove surface impurities and improve surface cleanliness, producing a more chemically active surface that promotes interfacial bonding during copper deposition [123], [124]. In addition to the heat sink diamond particles, smaller synthetic diamond particles with a nominal size of approximately 65 µm were used exclusively for the thermal interface material work presented in Chapter 5. The morphology and particle size distribution of these particles are shown in **Figure 3.2**. This particle size was selected to be smaller than the thickness of the compressed as-received thermal paste layer, which is approximately 120 µm (**Appendix A.5**). Larger particles were not

used, as they would increase the overall thickness of the TIM layer. An increase in bond line thickness leads to higher thermal resistance, which would counteract the benefits of incorporating a high thermal conductivity filler and ultimately degrade thermal performance. These smaller particles were rinsed with deionized water and dried prior to incorporation into paste-based formulations.

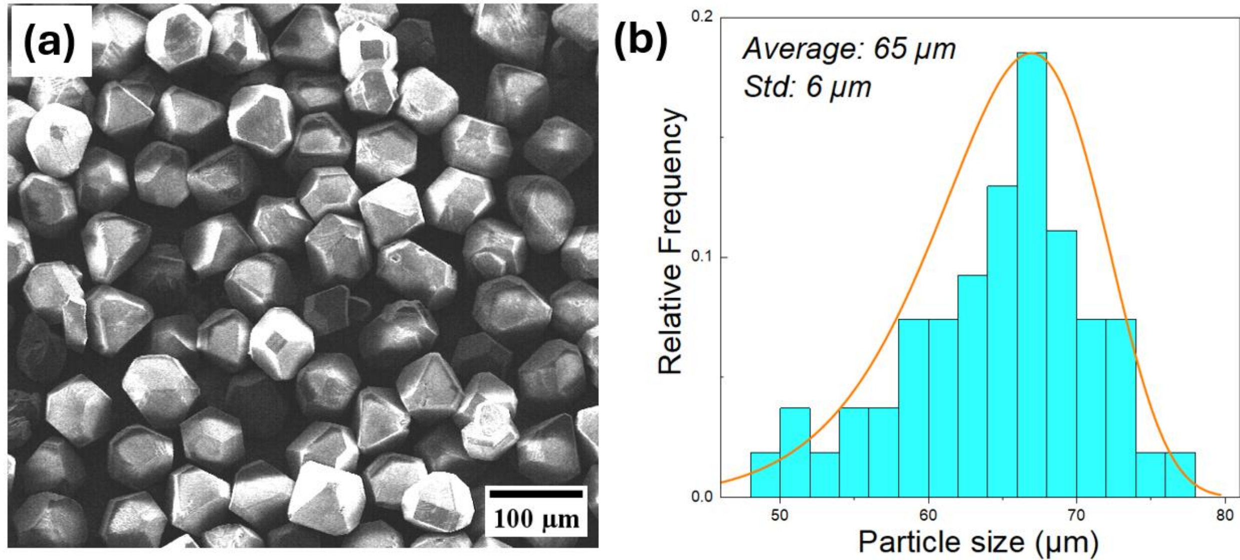

Figure 3.2: (a) SEM image of the synthetic diamond particles and (b) the corresponding particle size distribution (right), showing an average particle size of 65 ± 6 µm.

All diamond particles used in this work exhibit cubo-octahedral shapes primarily showing (111) and (100) planes with near-equiaxed geometry (aspect ratio close to unity). The copper plating bath composition and operating parameters are summarized in **Table 3.1**. Copper sulfate pentahydrate ($CuSO_4 \cdot 5H_2O$, 250 g/L) served as the primary source of Cu^{2+} ions, while sulfuric acid (H_2SO_4, 230 g/L) was added to enhance electrolyte conductivity and maintain Cu^{2+} solubility. The acidic environment also facilitated anode dissolution, ensuring a stable supply of copper ions throughout the electrodeposition process.

Table 3.1 - Bath composition and plating parameters for Cu-D composite materials

Bath compositions	
$CuSO_4(5{\cdot}H_2O)$ H_2SO_4 (Sulfuric acid) Diamond particle concentration	100 – 120 g/L 230 g/L (125 mL/L) 2 g/L
Plating parameters	
Bath temperature Current density (per cathode area) Bath agitation rate	20 °C 12 mA/cm^2 125 – 150 RPM

A titanium cathode was used for electrodeposition, onto which a 3D-printed polylactic acid (PLA) frame with a 1 cm × 1 cm plating area was secured using an electroplating maskant (Enplate Stop-off No.1, Canadian Finishing System Ltd., Burlington, ON, Canada). Titanium was chosen since it develops a thin, stable TiO_2 passivation layer, which limits bonding with the electrodeposited copper and facilitates easier removal of the composites following deposition [125]. High-purity copper nuggets (99.99%, Belmont Metals Inc., Brooklyn, NY, USA) served as the anode. The experimental apparatus is shown in **Figure 3.3a**, while a schematic illustration of the system is provided in **Figure 3.3b** for clarity. The setup employed a horizontally oriented titanium cathode in a gravity-assisted (sedimentation) plating arrangement to facilitate diamond particle incorporation. Deposition was performed with a DC power supply in a magnetically stirred plating bath.

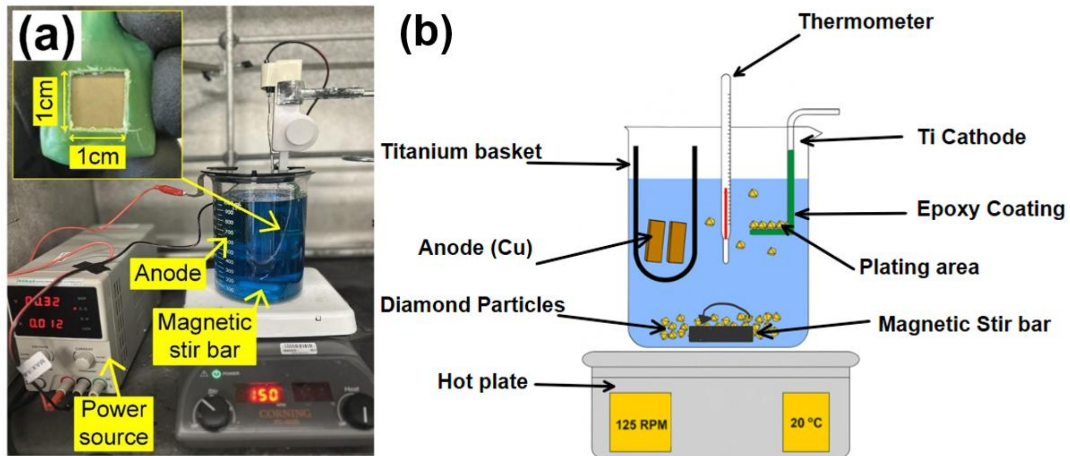

Figure 3.3: (a) Experimental electrodeposition apparatus for fabricating Cu-D composites and (b) schematic illustration of the plating setup.

The sequential development of Cu-D composite samples during electrodeposition is demonstrated in **Figures 3.4(a–f)**, with the corresponding schematical illustration is shown in **Figure 3.4(g)**. Diamond particles initially settle on the cathode surface and become embedded by copper growth. As electrodeposition proceeds, additional layers of diamond particles are introduced one after another, each encapsulated by the copper matrix, until the desired composite thickness is achieved. An initial layer of diamond particles was established by briefly increasing agitation in the plating bath before the power source was activated, allowing the particles to settle uniformly on the cathode. Once electrodeposition began, the particles were incorporated into the growing copper layer. Subsequent layers were introduced by intermittently re-suspending the particles through short bursts of agitation, ensuring that each new layer was deposited only after the preceding layer was sufficiently covered with copper. During the particle suspension process, the stirring rate was increased to approximately 400 RPM for ~1 min, after which the diamond particles were manually leveled across the cathode. The timing of each burst was set by the estimated copper deposition thickness, which was calculated from the applied current and Faraday's law, accounting for the two-electron reduction of Cu^{2+} to Cu. The resulting mass deposition rate was converted to volume using the density of copper and then to an average layer thickness based on the cathode area. Agitation was applied only after sufficient copper coverage had formed over the previously deposited particle layer, ensuring mechanical encapsulation before the introduction of additional particles. A sample calculation used to estimate copper deposition thickness and guide agitation timing is provided in **Appendix A.7**. This iterative stacking approach, performed continuously without interrupting the current, resulted in a multilayered Cu–diamond composite structure with uniformly distributed diamond particles and good interlayer bonding, as illustrated in **Figure 3.4(g).**

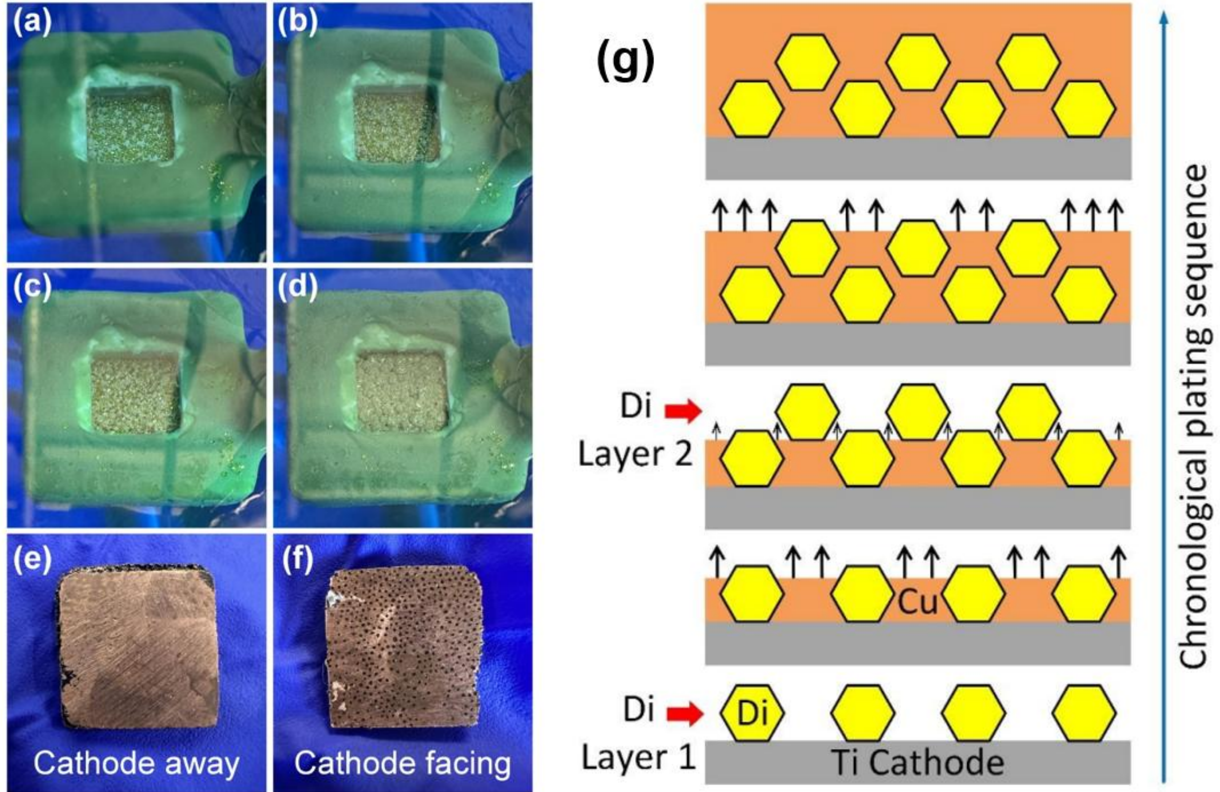

Figure 3.4: (a–d) Optical micrographs showing diamond particle deposition and copper coverage during electrodeposition; (e,f) as-prepared composite heat sink after grinding; (g) schematic of layer-by-layer particle embedding and copper growth.

In terms of diamond particle distribution, two types of Cu-D composites were fabricated: single-layered (SL) and multi-layered (ML) (**Figure 3.5**). The SL composite contained one diamond layer positioned near the cathode side, whereas the ML composite incorporated several diamond layers distributed throughout the composite thickness For each configuration, TiC-coated and uncoated diamond particles were used, resulting in four composite samples: coated single-layer (CSL), coated multi-layer (CML), non-coated single-layer (NCSL), and non-coated multi-layer (NCML), fabricated to replicate the high thermal conductivity values reported previously [42]. Two baseline materials, aluminum (Al) and pure copper (Cu), were also evaluated. Pure copper samples were electrodeposited under identical conditions without diamond particles to enable a direct comparison. These configurations allowed systematic assessment of the effects of particle coating and composite architecture on the thermal performance.

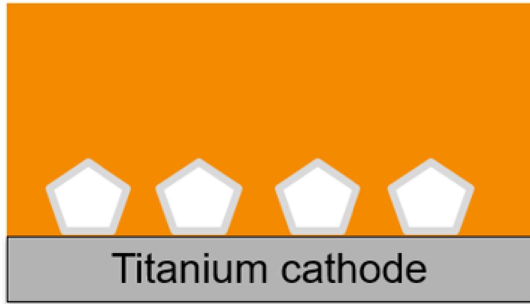

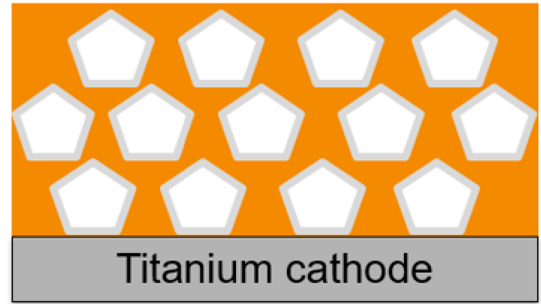

Figure 3.5: Schematic illustration of the electrodeposited Cu-D composite configurations: (a) SL and (b) ML composites. Each configuration was also prepared using TiC-coated diamond particles to investigate interfacial effects.

In total, seven heat sink samples were evaluated in this thesis. Six heat sink samples were used for the heat sink performance evaluation presented in Chapter 4, while an additional larger pure Cu heat sink was used exclusively for the thermal interface material evaluation described in Chapter 5. Of the seven samples, six were fabricated by electrodeposition, including pure Cu reference heat sinks and Cu-D composite heat sinks containing diamond particles with and without surface coatings. The Al heat sink was used as a commercially sourced reference (purchased from Home Depot and cut and grinded to identical external dimensions as the electrodeposited samples). Only one heat sink was produced for each configuration. All heat sink samples were mechanically ground using silicon carbide (SiC) abrasive papers from 240 to 800 grit. The same grinding procedure was applied to all specimens to ensure consistent surface quality for radiation and convection. Samples were ground until the thickness became uniform across the planar area to minimize variations in thermal contact resistance during testing.

3.2 Sample dimensions and diamond volume fraction calculations

For each composite sample, the diamond volume fraction was determined using the measured mass and dimensions of the electrodeposited coating, applying the rule of mixtures based on the known densities of copper and diamond. The theoretical density of each composite (ρ_c) was first obtained from the measured mass (m) and geometric volume (V) using $\rho_c = \frac{m}{V}$. The diamond volume fraction (V_d) was then calculated from the rule of mixtures:

$$V_d = \frac{(\rho_{Cu} - \rho_C)}{(\rho_{Cu} - \rho_D)} \times 100\% \tag{3.1}$$

where ρ_{Cu} and ρ_D are the densities of copper (8.96 g·cm^{-3}) and diamond (3.52 g·cm^{-3}), respectively.

The dimensions and diamond volume fractions of the tested samples are listed in **Table 3.2**, where the diamond content for each composite was calculated using Equation (3.1) based on the measured mass, sample dimensions, and material densities. All samples were ground until their thicknesses became reasonably uniform across the whole planar area. The sample dimensions were all approximately 1 cm × 1 cm × 0.125 cm while the diamond volume fractions were up to 55%.

Table 3.2 - Dimensions and diamond volume fractions of heat sink samples used in the composite heat sink performance evaluation (Chapter 4). Thickness errors are from statistical variations across planar areas

Heat sink material	Length (cm) × Width (cm)	Thickness (mm)	Mass (g)	Diamond vol. frac. (%)
Al	1.00 ± 0.01 × 1.00 ± 0.01	1.28 ± 0.04	0.332 ± 0.01	-
Cu		1.27 ± 0.04	1.053 ± 0.01	-
NCSL		1.24 ± 0.04	0.971 ± 0.01	19.8 ± 0.7
NCML		1.24 ± 0.04	0.820 ± 0.01	42.4 ± 1.5
CSL		1.25 ± 0.03	0.998 ± 0.01	17.0 ± 0.5
CML		1.25 ± 0.04	0.740 ± 0.01	55.2 ± 1.9

The larger pure Cu heat sink used for the thermal interface material testing in Chapter 5 is not included in this table, as it has a larger footprint (1.30 × 1.30 cm^2) and thickness (0.215 cm) compared to the composite heat sinks evaluated in Chapter 4, and was therefore not part of the composite heat sink performance testing.

3.3 Scanning electron microscopy and X-ray diffraction

Scanning electron microscopy (SEM, Zeiss GeminiSEM 500) was used to determine the distribution of diamond particles and the microstructures of the electrodeposited materials. The composite samples were cut in half using a waterjet to see the cross-sectional microstructures.

The crystallographic orientations of Cu-D composites were characterized using a Bruker D8 Endeavor X-ray diffractometer (XRD). The software package of the X-ray diffractometer (Rigaku Miniflex 600) provided the Inorganic Crystal Structure Database (ICSD) with the relative diffraction peak intensities for randomly oriented crystalline materials. The diffraction condition, governed by Bragg's law (**Figure 3.6**), describes the requirement for constructive interference, which occurs when the path difference between X-rays reflected from successive crystal lattice planes is equal to an integer multiple of the X-ray wavelength:

$$n\lambda = 2dsin\theta \tag{3.2}$$

where *n* is the diffraction order, λ is the X-ray wavelength, *d* is the interplanar spacing, and θ is the Bragg angle. This principle explains the origin of diffraction peaks used to calculate the orientation index.

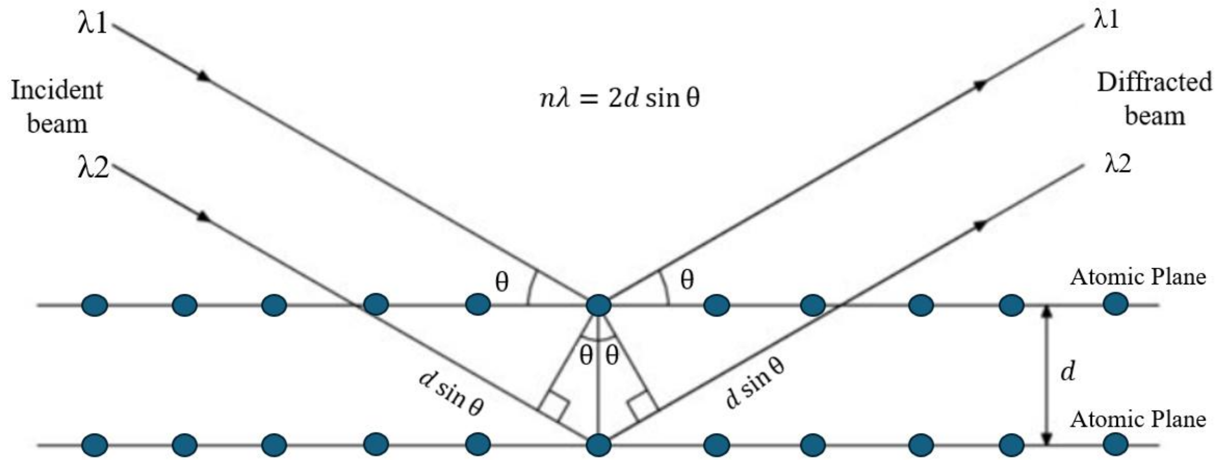

Figure 3.6: Schematic illustration of Bragg's law showing the diffraction of X-rays from successive atomic planes in a crystalline material.

Using equation 3.3, the XRD orientation index η_{hkl} of a measured (*hkl*) peak was calculated [126].

$$\eta_{hkl} = \left(\frac{I_{(hkl),m}}{\sum_{h'k'l'} I_{(h'k'l'),m}}\right) \Bigg/ \left(\frac{I_{(hkl),r}}{\sum_{h'k'l'} I_{(h'k'l'),r}}\right) \tag{3.3}$$

where I is the XRD intensity, subscripts "m" and "r" stand for the measured specimen and the randomly oriented crystalline material, respectively. *hkl* is the Miller index, and the summation takes over all the peaks observed from the XRD pattern. A material's preferred orientation can be determined by the orientation index. The orientation index for every peak in a random crystal orientation is 1. However, if a peak's orientation index is higher than 1, it means that the plane in consideration is preferentially oriented with the observed sample surface. A sample orientation index calculation can be found in **Appendix A.1.**

3.4 Heat sink performance testing and setup

The thermal performance of the samples was evaluated by integrating them as heat sinks on the back of a commercially available light-emitting diode (LED, TOPINCN B07F67GRWD), as shown in **Figure 3.7**. The LED consists of an InGaN/GaN junction mounted on an aluminum substrate with a silicone encapsulant and operates within a forward voltage range of 9–12 V and a typical forward current of 200 mA.

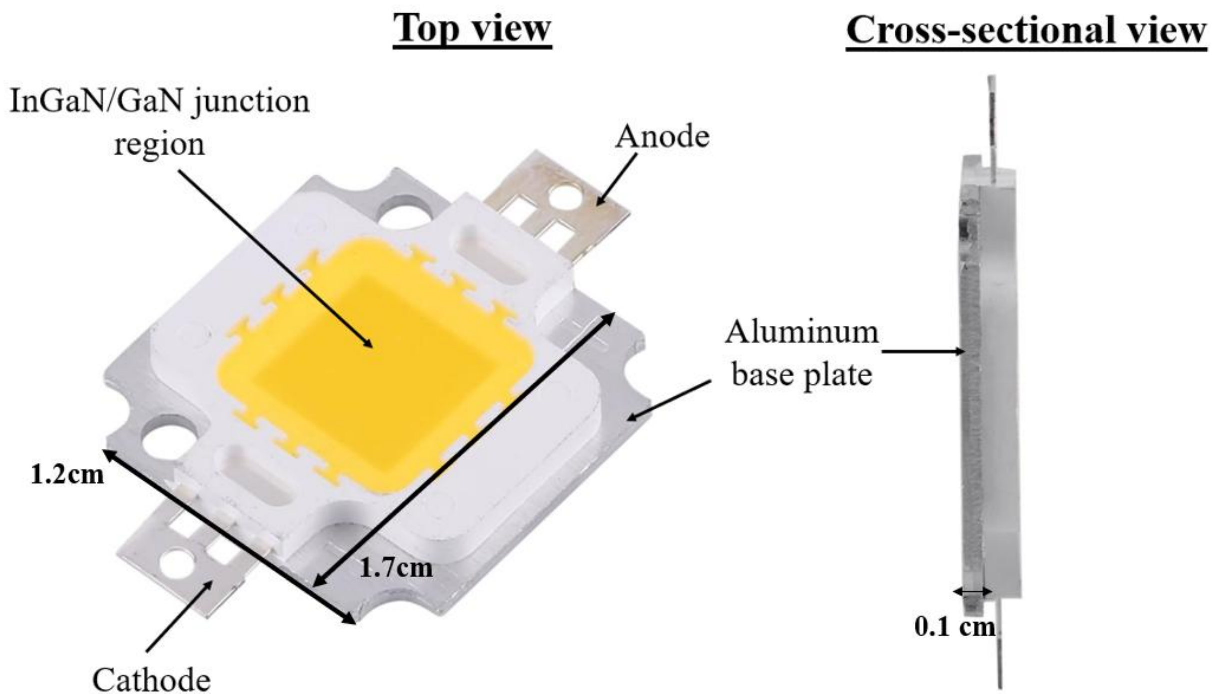

Figure 3.7: The LED used in this project (LED lamp beads, TOPINCN)

The experimental setup shown in **Figure 3.8** was used for both the composite heat sink performance evaluation presented in Chapter 4 (left) and the thermal interface material (TIM) studies presented in Chapter 5 (right).

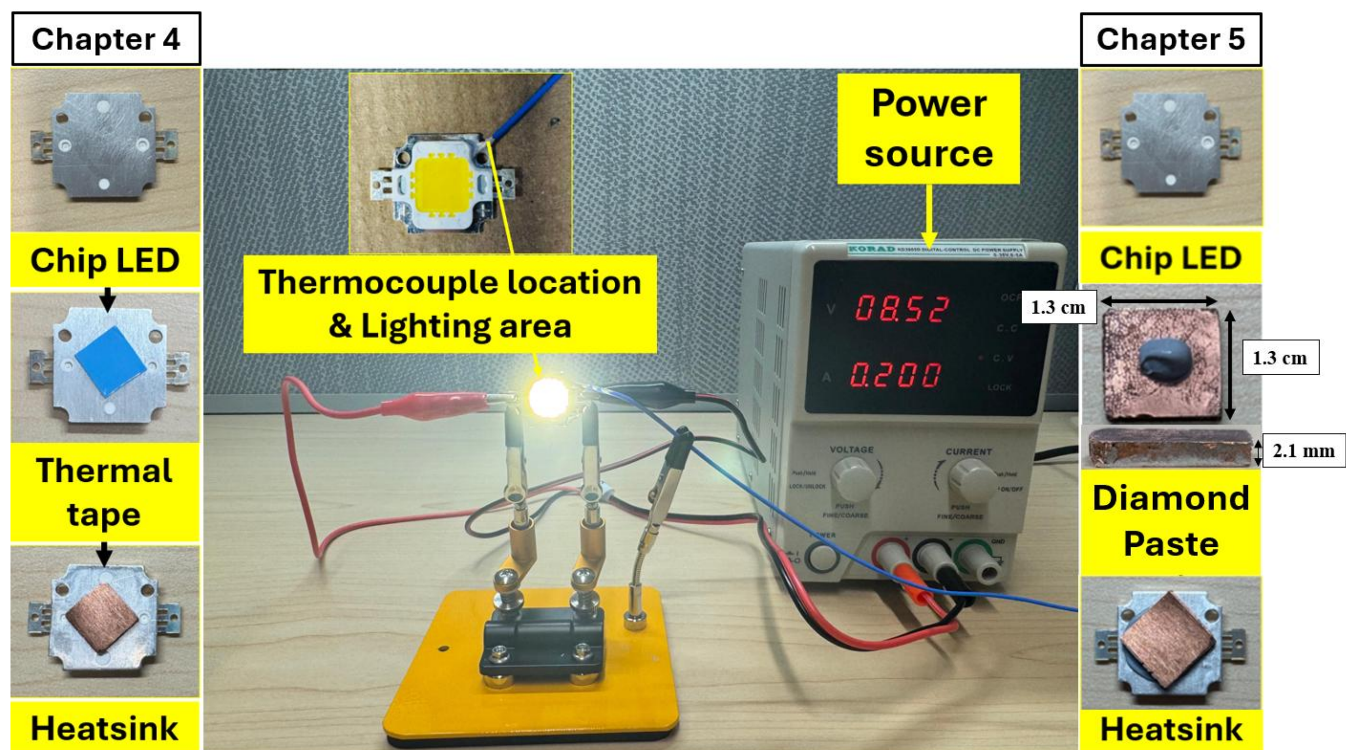

Figure 3.8: Experimental setup for LED-based heat sink performance testing. The LED is mounted onto the heat sink using a thermal interface material (TIM), with temperature measured via a thermocouple near the lighting region. Figure shows configurations for Chapter 4 (thermal tape interface) and Chapter 5 (diamond-enhanced thermal paste).

For Chapter 4, the heat sink samples were attached to the LED using a thermally conductive adhesive tape (HOAOH, aluminum/silicone). The electrodeposited heat sinks used in these tests had dimensions of approximately $1.00 \times 1.00 \times 0.125$ cm^3 (**Table 3.2**). The thermal tape had an approximate thickness of ~0.2 mm and thermal conductivity ~3 $W \cdot m^{-1} \cdot K^{-1}$, based on manufacturer specifications. In Chapter 5, for modifying heat sink attachment with diamond particles, commercial thermal paste (SYY-157) and its diamond-enhanced formulations were evaluated as the thermal interface materials (TIMs). To better capture the influence of the thermal interface layer, larger heat sinks with dimensions of approximately $1.30 \times 1.30 \times 0.215$ cm^3 were used. A fixed amount of 0.05 g of TIM was applied in each test to maintain consistency in bond line thermal mass. In all cases, the cathode-facing side of each composite sample was oriented toward the LED.

A K-type thermocouple was attached directly onto the surface of the LED chip near the lighting area using silver paint and epoxy to ensure good thermal coupling and prevent movement during testing. The LED assembly was secured using a clamp-style test fixture (**Figure 3.8**), which held the LED and heat sink vertically and allowed stable electrical connections to the power supply. The total LED dimensions were approximately 1.2 cm × 1.7 cm × 0.3 cm, corresponding to a volume of 0.612 cm^3. For the composite heat sink evaluations in Chapter 4, the LED was operated at 200 mA, while in Chapter 5, the current was reduced to 150 mA to mitigate thermal aging as this chapter required many repeated measurements to collect statistics for anticipating human errors associated with manually applying TIMs. In all cases, the steady-state LED voltage was maintained at 8.52 ± 0.01 V.

3.5 Preparation of diamond-modified thermal interface materials

Three diamond–TIM formulations were prepared at 10 wt.%, 20 wt.%, and 30 wt.% filler loadings as part of the experimental work presented in Chapter 5. The corresponding diamond volume fractions were estimated using the rule of mixtures based on the densities of diamond (3.51 g/cm^3) and the thermal paste (2.9 g/cm^3), yielding approximately 8.4 vol.%, 17.1 vol.%, and 26.2 vol.%, respectively. For each mixture, 0.50 g of the thermal paste was first weighed, followed by the addition of the appropriate mass of diamond particles (resulting in total masses of 0.55 g, 0.62 g, and 0.71 g, respectively). The diamond particles were then manually incorporated into the paste using a shearing and folding action with a small spoon and a flat plastic card. During mixing, the paste was repeatedly pressed and spread to promote uniform particle dispersion while minimizing additional air entrapment. The viscosity of the composite increased with higher particle loading, but all formulations remained sufficiently spreadable for application onto the LED surface. The 30 wt.% formulation represented the highest practical loading that maintained a workable viscosity; higher diamond loading made the overall TIM excessively thick and difficult to spread uniformly. A schematic summary of the preparation workflow is provided in **Figure 3.9**, illustrating the weighing of materials, the addition of diamond particles, and the manual blending process.

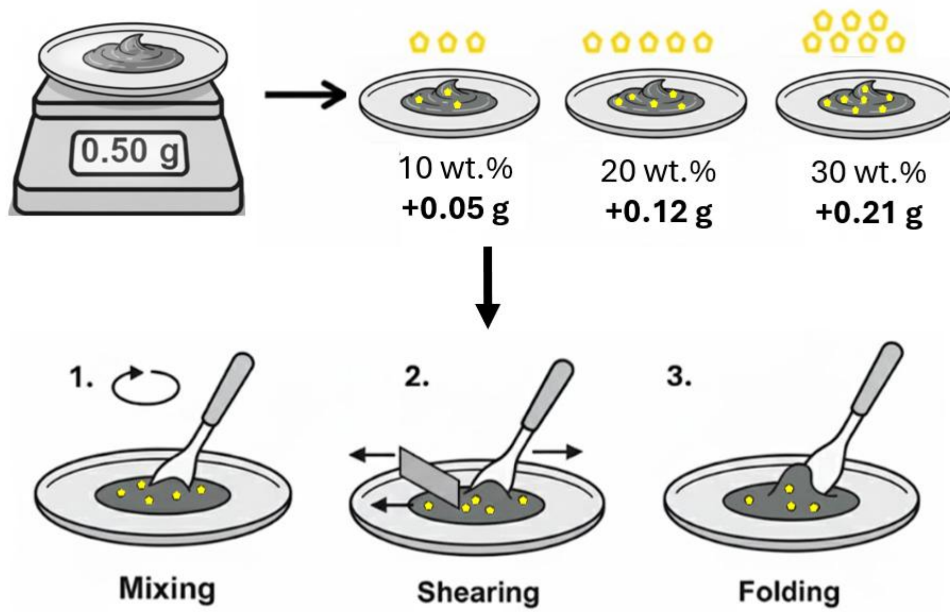

Figure 3.9: Schematic of diamond-loaded thermal paste preparation, showing filler addition (10–30 wt.%) and homogenization by mixing, shearing, and folding.

Chapter 4: Heat Sink Performance of Electrodeposited Copper–Diamond Composites Using Thermal Tape Interface

This chapter addresses the thermal performance of electrodeposited Cu-D composites implemented as heat sinks of a commercial LED with a thermal tape interface. The objective is to optimize the composite design by investigating the effects of particle stacking configuration and intermetallic coating (TiC) on the heat sink performance of the composites.

4.1 Electron microscopy and X-ray diffraction patterns

Microstructural features of the electrodeposited Cu-D composites are presented in **Figure 4.1**. In the planar view (**Figure 4.1a**), diamond particles appear uniformly distributed within the copper matrix, indicating effective incorporation during deposition. Cross-sectional images (**Figures 4.1b** and **4.1c**) show that the particles are aligned with the copper growth direction. The faceted voids observed within the matrix correspond to regions where diamond particles were dislodged during waterjet cutting. It can be seen that the diamond particle distributions in the copper matrix were successful as intended (CSL & CML).

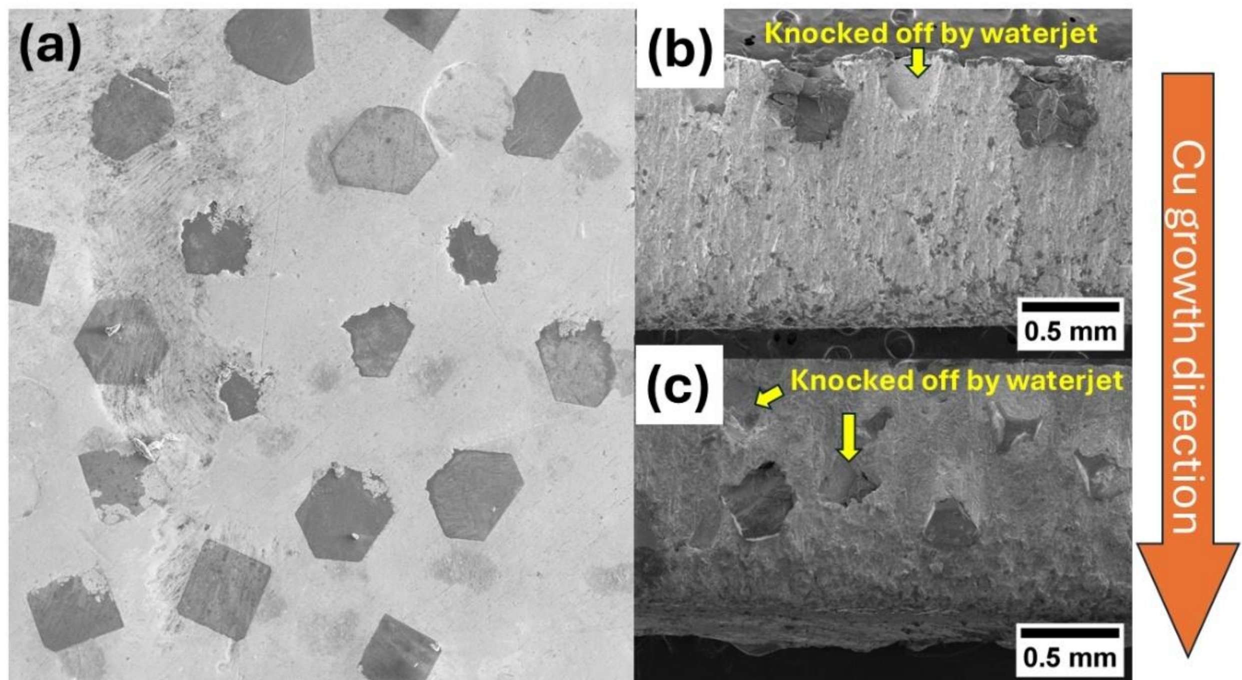

Figure 4.1: (a) Planar SEM view of as-deposited composite samples on the side facing the cathode, and microstructures of the cross-sections of (b) a CSL (19.8 vol.%) and (c) CML sample (42.4 vol.%).

At higher magnifications, the ion-milled cross-sectional SEM micrographs of electrodeposited Cu-D interfaces (**Figure 4.2**) reveal a continuous region between the copper matrix and diamond particles in both CML and NCML. No significant cracks, voids, or other interfacial defects are observed that could impair thermal conduction across the Cu-D boundary. For the composite with uncoated diamond particles (**Figure 4.2a, b**), copper near the interface consists of fine grains on the order of ~1 μm without any columnar textures. According to previous studies, this is not desirable for high thermal boundary conductance compared to large columnar textured grains [44] and may negatively affect the heat sink performance. In comparison, the TiC-coated composite (**Figure 4.2 c, d**) also shows a defect-free interface. The thin black lines observed in **Figure 4.2c** correspond to re-deposited diamond fragments generated during the ion-milling process. In addition, copper adjacent to the TiC-coated diamond also exhibits an equiaxed grain structure rather than the columnar texture typically associated with high thermal boundary conductance, indicating that the presence of the TiC interlayer alone does not promote the formation of large, oriented grains during electrodeposition.

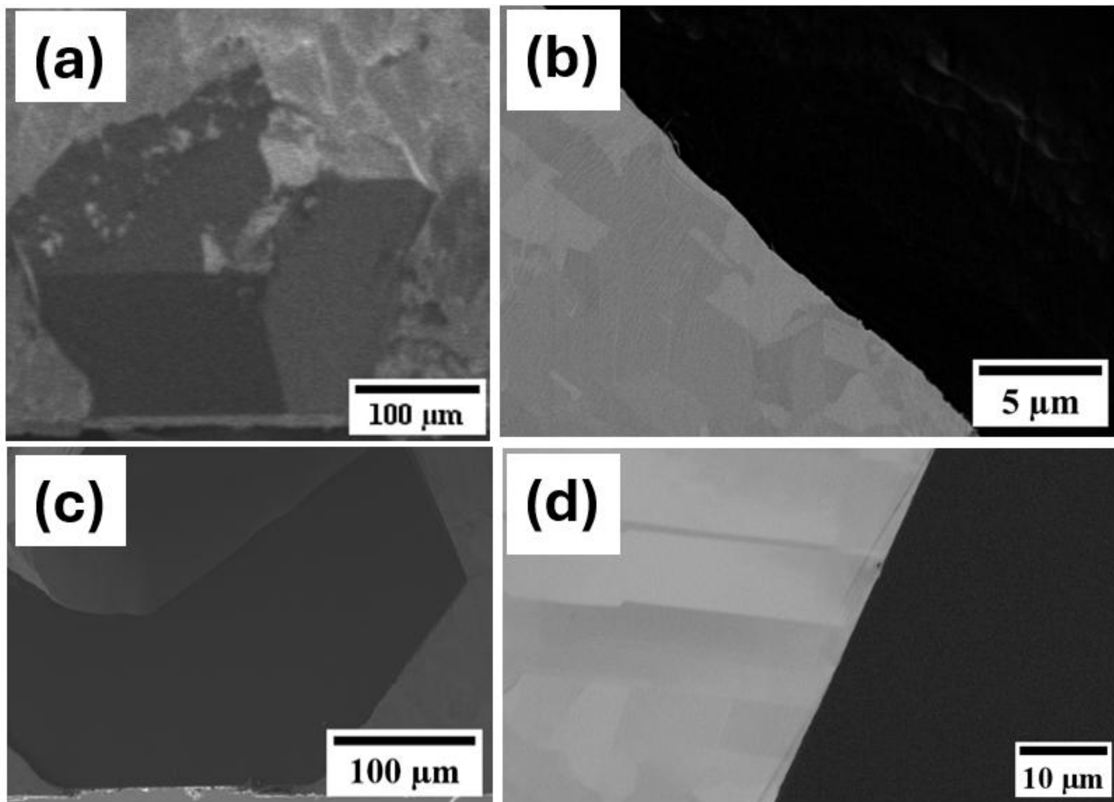

Figure 4.2: SEM micrographs of ion-milled electrodeposited Cu–D interfaces showing defect-free bonding for (a,b) uncoated and (c,d) TiC-coated diamond particles.

XRD patterns obtained from both sides of the electrodeposited samples are presented in **Figure 4.3**. Based on the orientation indices summarized in **Table 4.1**, the pure copper deposit initially exhibits a preferred crystallographic orientation along the [220] direction, consistent with observations from copper electroplated in acidic baths reported in previous studies [127], [128]. However, this [220] texture weakens as the deposition progresses and composite thickness increases. In contrast, for the Cu-D composites, the presence of diamond particles suppresses the [220] preferred orientation at the early stages of deposition. The absence of a distinct diamond (220) peak is attributed to the predominance of (100) and (111) facets on the diamond particle surfaces, as observed in **Figure 3.1a**. Furthermore, no diamond peaks are detected on the composite side facing away from the cathode, since most of the diamond particles on that side are embedded and fully encapsulated by the copper matrix, as illustrated in **Figure 3.4e**.

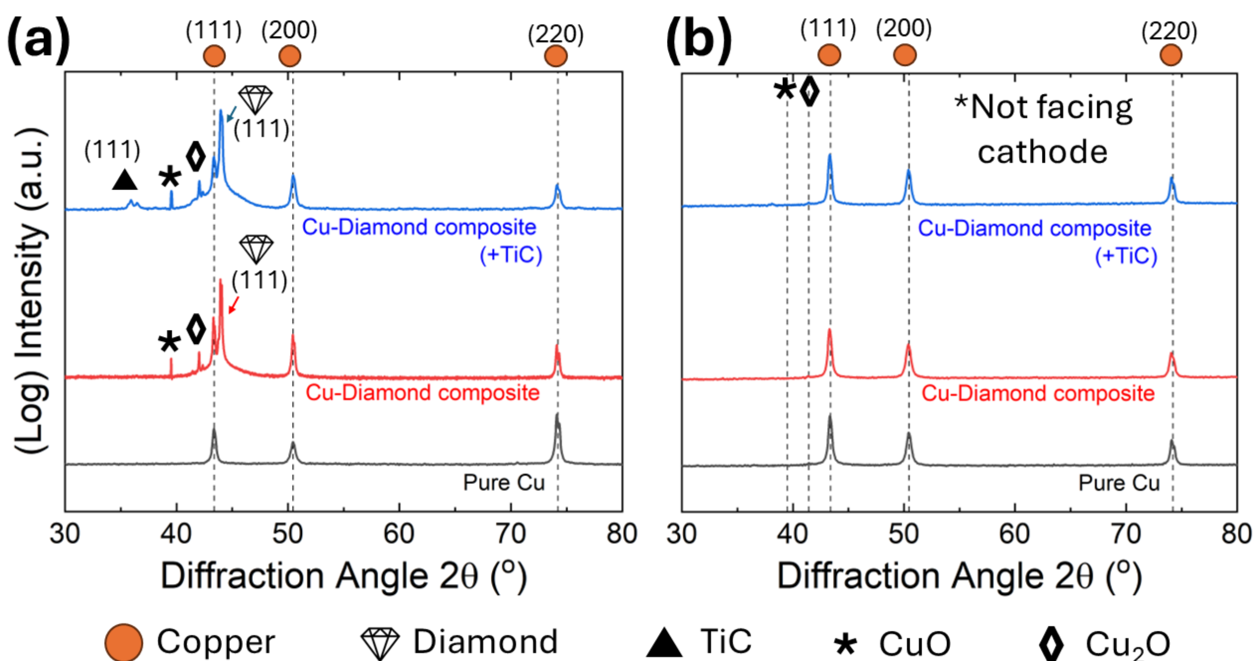

Figure 4.3: XRD patterns of the electrodeposited pure copper and Cu-D composite materials obtained from (a) sample side facing the cathode and (b) sample side facing away from the cathode.

Table 4.1 - Copper crystallographic orientation indices (η_{hkl}) for electrodeposited pure Cu and Cu–diamond heat sink materials.

Heat sink materials	Planes	η_{hkl} (start of plating → end)
Pure Cu	(111)	(0.43 ±0.01) → (0.94±0.01)
	(200)	(0.50 ±0.01) → (1.05 ±0.01)
	(220)	(3.55 ±0.03) → (1.18 ±0.03)
Copper-diamond	(111)	(0.98 ±0.01) → (0.90 ±0.01)
	(200)	(0.97 ±0.02) → (1.10 ±0.02)
	(220)	(1.19 ±0.05) → (1.27 ±0.06)
Copper-diamond (+TiC on diamond)	(111)	(1.10 ±0.04) → (0.96 ±0.01)
	(200)	(0.81 ±0.02) → (1.03 ±0.03)
	(220)	(0.97 ±0.05) → (1.12 ±0.07)

For the composites containing TiC-coated diamond particles, TiC (111) diffraction peaks appear as doublets (**Figure 4.3**, indicated by triangles), which can be attributed to variations in TiC formed on the (100) and (111) diamond surfaces. Both types of composites, those with and without TiC coatings, exhibit additional peaks corresponding to CuO and Cu_2O, indicating surface oxidation. The intensity of these oxidation peaks is significantly higher on the cathode-facing side compared to the opposite side. This difference arises from the sedimentation plating process, wherein the cathode-facing surface contains a greater number of exposed diamond particles, as shown in **Figures 3.4e** and **3.4f**. The increased exposure of diamond particles appears to be promoting localized oxidation of the copper matrix. Here, the extra thermal resistance from the oxidation layer was assumed to be negligible, as it is much thinner than the thermal tape and beyond the scope of this work. However, future work would be required to quantify its exact impact.

4.2 Heat sink performance of electrodeposited copper-diamond composites

The heat sink performance of Cu-D composites, along with that of commercially available aluminum, are shown in **Figure 4.4** while the respective steady-state temperatures of the LED with different heat sink materials are summarized in **Table 4.2**. The dimensions and diamond volume fractions of the tested samples are summarized in **Table 3.2** (see Section 3.2).

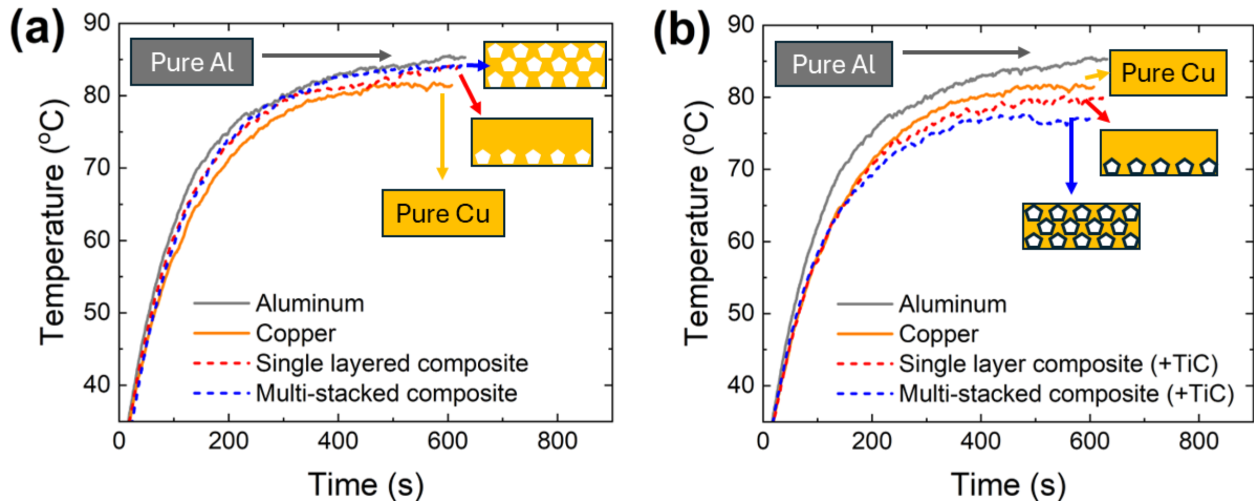

Figure 4.4: Heat sink performances of (a) Cu-D composites and (b) Cu-D composites with intermetallic TiC coatings on diamond particles.

Table 4.2 – Steady-state LED temperatures with different heat sink materials, calculated from the average temperature of the last 30 seconds in the plateau. The uncertainties are the respective standard deviations.

Heat sink material	Steady-state temp.
Al	85.27 ± 0.13 ºC
Cu	81.43 ± 0.15 ºC
NCSL	83.93 ± 0.13 ºC (↑)
NCML	84.09 ± 0.24 ºC (↑)
CSL	78.65 ± 0.23 ºC (↓)
CML	76.97 ± 0.09 ºC (↓)

For the uncoated Cu-D composite, the inclusion of diamond particles resulted in an increase in steady-state temperature relative to the pure copper heat sink, indicating a reduction in overall heat-removal efficiency. This observation contrasts with the results reported by Cho et al. [44]; electrodeposited Cu–D composites containing large (~400 μm) uncoated diamond particles achieved up to ~13% higher thermal conductivities than pure copper. The present work, however, reveals the opposite trend, lower heat sink performance despite using similarly large particle sizes. This discrepancy can be attributed to the microstructural evolution of the copper matrix at the Cu–

D interface. The copper microstructures near diamond particles observed from this thesis and a previous study from Cho *et al.* [44]are shown in **Figure 4.5** (with permission). In this work, the ion-milled cross-section (**Figure 4.5(a)**) reveals small equiaxed copper grains near the diamond particles (400 um). In contrast, in ref. [44], vertically oriented columnar copper grains extending from the surface to the Cu-D interface when similar ~400 um particles were incorporated (**Figure 4.5(c)**) [44]. The microstructure of copper near diamond particles in this work resembles that near 66 um particles in ref. [44] (**Figure 4.5(b)**), which was not favorable for high thermal boundary conductance. Consequently, although the current electrodeposited interface is metallurgically continuous and free of voids or cracks, its thermal boundary conductance (TBC) remains limited because the copper grain structure is unfavorable for efficient phonon transportation. The absence of the columnar morphology likely stems from the variation in plating geometry between this work (1 cm × 1 cm, square-shaped) and ref. [44] (1.5 cm × 0.3 cm, needle-like). This could have affected how the current-density field developed during electrodeposition. These findings suggest that in electrodeposited systems, achieving a defect-free interface alone is insufficient, and that the interfacial copper grain orientation and size play an equally decisive role in determining heat-transfer efficiency. Nevertheless, it is worth noting that columnar copper grains would not have offered substantial improvements in the heat sink performance here since the maximum thermal conductivity reported in ref. [44], with the columnar copper grains, is only 454 W/ m·K. On the other hand, when the diamond particles are coated with TiC, a notable improvement in thermal performance is achieved. The lowest LED temperature recorded was 76.97 °C for the multilayered Cu-D composite with TiC coatings, representing a 4.46 °C decrease relative to the pure copper heat sink and an 8.30 °C decrease compared to the aluminum heat sink. This reduction is particularly significant considering that the heat sinks used in this chapter had a volume of only 0.125 cm^3, nearly five times smaller than the LED (0.612 cm^3). These results confirm that establishing effective vibrational coupling between copper and diamond through interfacial coatings like TiC is critical for optimizing heat sink performance in electrodeposited Cu-D systems. Although the multi-layer Cu-D composite with TiC coatings showed the best thermal performance, the single-layer Cu-D composite with TiC coatings also showed a significant improvement over pure copper and aluminum heat sinks, reaching a steady-state temperature of 78.65 °C. This shows that even a single-layer diamond in the composites can deliver substantial cooling performance, and a compromise can be considered between heat sink performance and

fabrication cost, as single-layered diamond composites involve lower raw materials cost as well as reduced labor associated with multi-stacking diamond layers.

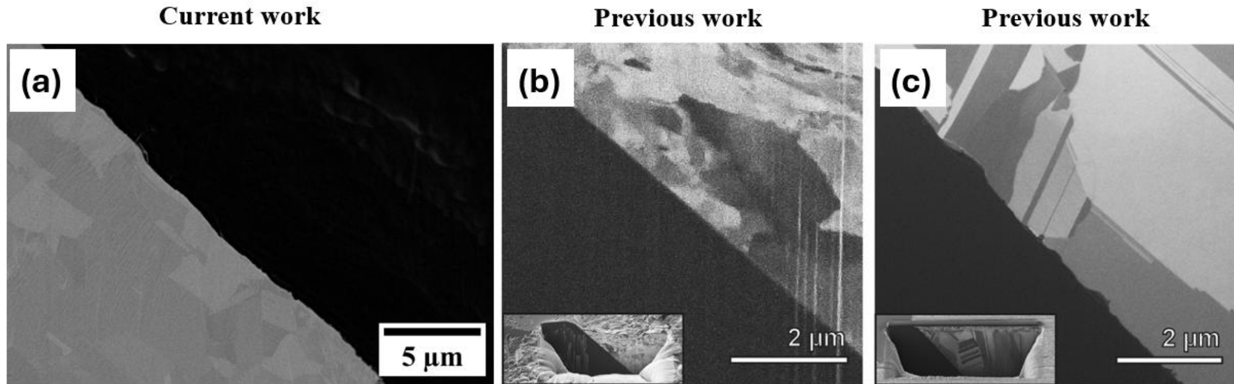

Figure 4.5: Comparison of copper matrix microstructures near diamond particles in uncoated Cu–D composites. (a) Present work showing fine, equiaxed copper grains; (b,c) previous work illustrating interfaces with (b) 66 µm and (c) 420 µm diamond particles.

4.3 Discussions

Building upon the predictive models introduced in Chapter 2, the Differential Effective Medium (DEM) approach was applied to interpret the influence of diamond volume fraction and interfacial thermal conductance on composite thermal conductivity. As described in Section 2.6.2, the effective particle conductivity relation accounts for the interfacial thermal resistance between copper and diamond. The effective particle conductivity relation previously defined in Equation 2.11 was therefore used in this section to support the discussion of the experimental thermal performance trends without repeating the equation.

The thermal conductivity of electrodeposited copper is approximately 400 W/m·K [42], [44], while the diamond particles incorporated in the present composites have an average size of 405 µm. Using the diamond particle thermal conductivity of $\kappa_p \approx 1800$ W/m·K, as reported in a previous study employing diamond particles from the same manufacturer [38], the minimum Cu-D interfacial thermal boundary conductance (TBC) required to enhance the composite thermal conductivity (compared to pure copper) is estimated to be 2.6 MW/m^2·K using equation 4.1 (details available in **Appendix A.2**). As heat sink performance directly correlates with the heat

sink thermal conductivity, these findings suggest that the effective TBC at the electrodeposited Cu-D interfaces in this chapter is below 2.6 MW/m²·K.

Figure 4.6 summarizes the reported values of thermal boundary conductance at Cu-D interfaces without intermediate coatings on the diamond surface, directly cited from literature or derived from analyzing experimentally measured thermal conductivity in Cu-D composites fabricated by both electrodeposition and high-temperature synthesis methods. The corresponding numerical data used for **Figure 4.6** are available in **Appendix A.3** (**Table A.2**). Most studies involving high-temperature processes report TBC values on the order of ~5 MW/m²·K, with a few exceptional cases reaching 30–50 MW/m²·K. In contrast, aside from the early study (ref. [42]) and the present work, several investigations on electrodeposited Cu-D composite materials reported high thermal conductivities up to 846 W/ m·K and Cu-D boundary conductance comparable to exceptional results from high temperature methods (**Figure 4.6**). These higher values are commonly attributed to the formation of defect and void-free interfaces between copper and diamond, as observed in multiple reports [41], [45], [47], [48], [114], [115]. However, ref.[44] demonstrated low thermal boundary conductance on the order of 3 MW/m^2K at defect-free Cu-D interface formed by electrodeposition. In this work, despite the absence of visible microstructural defects at the micrometer scale (**Figures 4.1** and **4.2**), the TBC inferred from the heat sink performance is also estimated to be on the order of 3 MW/m²·K, comparable to most values obtained from high-temperature synthesis methods. This observation underscores that a defect-free interface does not necessarily ensure high thermal boundary conductance. These scattered results can be brought into better contexts if compared with theoretically calculated thermal boundary conductance values at the Cu-D interfaces.

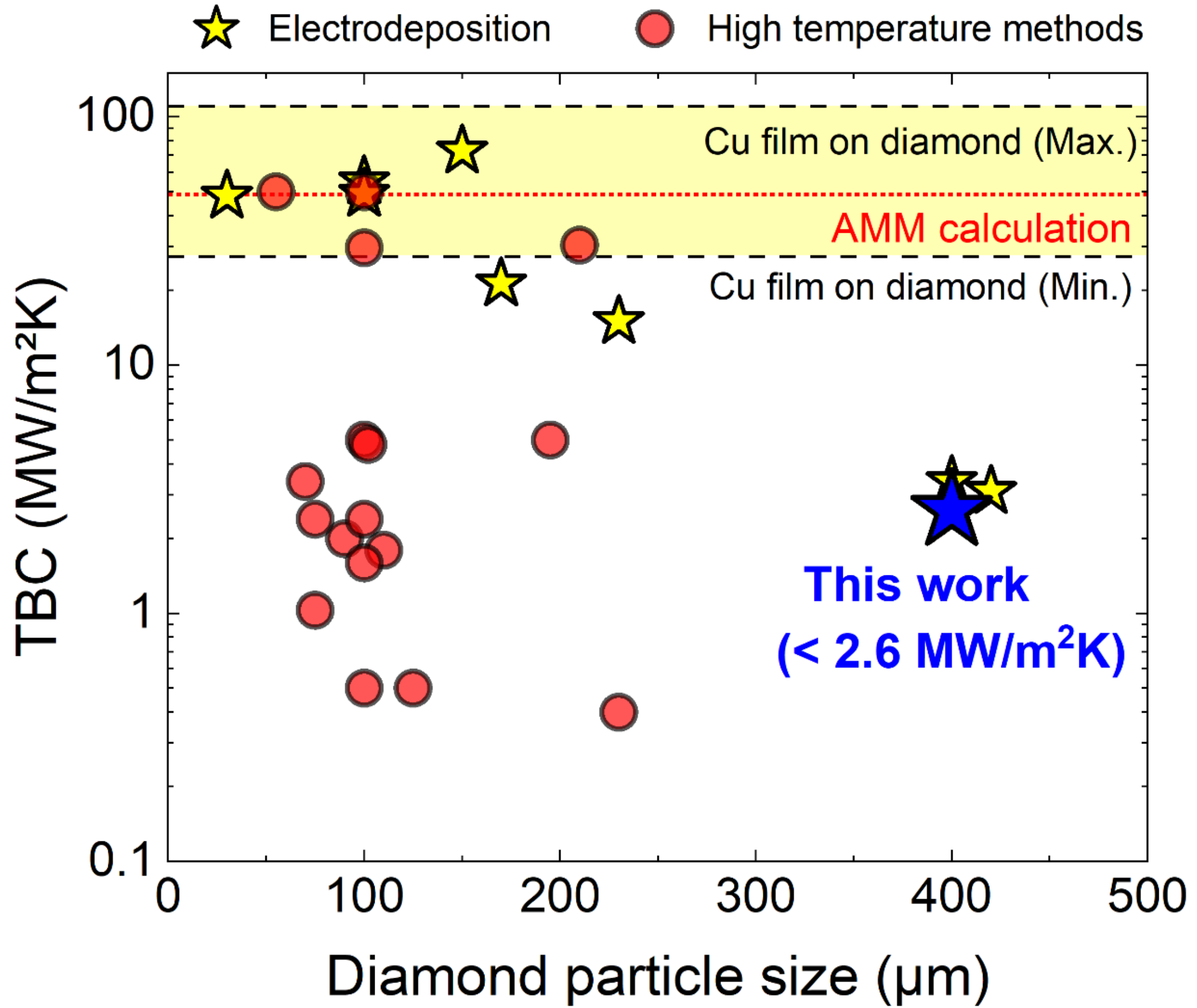

Figure 4.6: Thermal boundary conductance (TBC) at the Cu–diamond interface as a function of diamond particle size, comparing electrodeposition and high-temperature fabrication methods.

The upper bound for the achievable thermal boundary conductance (TBC) at the Cu-D interface is typically estimated using classical phonon transport models, namely the Acoustic Mismatch Model (AMM) and the Diffuse Mismatch Model (DMM). Both models are based on continuum wave mechanics and describe phonon transmission across dissimilar interfaces.

In the AMM, the interface is treated as a perfectly smooth boundary, and phonon transmission is governed by the acoustic impedances of the two materials:

$$\alpha_{1\to 2} = \frac{4Z_1Z_2}{(Z_1+Z_2)^2} \tag{4.1}$$

where $Z_i = \rho_i v_i$ is the acoustic impedance, ρ_i is the density, and v_i is the sound velocity of material i. The corresponding TBC can be expressed as:

$$G_{AMM} = \frac{1}{4} \sum \int_0^{\omega Dj} C_j(\omega, T) v_j(\omega) \alpha_{1\rightarrow 2}(\omega) d\omega \tag{4.2}$$

where $C_j(\omega, T)$ is the phonon heat capacity per mode and $\omega_{D,j}$ is the Debye frequency. The AMM assumes specular phonon transmission and provides an upper theoretical limit for well-bonded, coherent interfaces [127]. Conversely, the DMM assumes completely diffuse phonon scattering, where phonons lose memory of their incident direction upon transmission. The transmission coefficient ($\alpha_{1\rightarrow 2}$) is determined by the ratio of the phonon densities of states in the two materials:

$$\alpha_{1\rightarrow 2} = \frac{\sum_j D_2(\omega_J) v_{2j}}{\sum_j [D_1(\omega_j) v_{1j} + D_2(\omega_j) v_{2j}]} \tag{4.3}$$

where $D_i(\omega)$ is the phonon density of states (DOS) of material i, representing the number of available phonon modes per unit frequency that can participate in thermal transport, and v_i is the phonon group velocity. The DMM provides a more realistic lower bound for thermally rough or incoherent interfaces [129]. Using these models, the theoretical TBC at a Cu-D interface is approximately 49 MW/m^{2}K at 300 K [45]. A bit more refined predictions are available through *ab-initio* calculations, which are 24.2 - 27 MW/m^{2}K at 300 K[130], [131], [132]. Experimental validation of these numbers, measured from pristine Cu-D interfaces prepared by depositing copper films on diamond plates, range from 27.5 MW/m^{2}K to 110 MW/m^{2}K [131], [132], [133], [134], [135], [136], averaging to ~55 MW/m^{2}K.

Since interfaces produced by thin-film deposition techniques such as sputtering or electron-beam deposition are considerably more pristine (i.e., well bonded structures without impurities) to those formed by high-temperature synthesis or electrodeposition, achieving thermal boundary conductance values on the order of ~30 MW/m^2·K (the lower bound typically reported for film-deposited systems, **Figure 4.6**) would require extraordinary interfacial bonding mechanisms at the Cu-D boundary. In Cu-D composites fabricated by high temperature methods, despite the low

wettability of carbon-based surfaces for copper [137], [138], [139], [140], firm interfaces and high thermal boundary conductance can be explained by high external pressures during the synthesis. For example, 2 of the 4 exceptional thermal boundary conductance results in **Figure 4.6** from high-temperature methods involved synthesis pressures on the order of GPa [108], [141]. However, such specialized conditions do not exist for Cu-D interface formed by electrodeposition, as the nature of microstructure formation is the diamond particles being surrounded by the copper matrix growing from the cathode. Therefore, thermal boundary conductance on the order of 30 MW/m^2K or higher in electrodeposited Cu-D interfaces is weakly justified by defect/void free interfaces as conflicting thermal boundary conductance results exist on similar defect-free interfaces [44], [45]. The findings of this study are consistent with previously reported results [44] and further indicate that a defect-free Cu-D interface alone is not sufficient to achieve thermal boundary conductance values (greater than 30 $MW/m^2 \cdot K$) in electrodeposited Cu-D heat sinks. This highlights that interfacial integrity, while necessary, does not solely govern thermal transport in electrodeposited systems, and that factors such as copper grain structure also play critical roles. Bridging this discrepancy will require extensive interfacial characterization in combination with heat sink performance testing and bulk thermal conductivity measurements to fully clarify the mechanisms that limit thermal boundary conductance. Such combined investigations are essential before electrodeposited Cu-D composites can advance toward practical application and commercialization.

4.4 Research Contributions from This Chapter

The heat sink performance of electrodeposited Cu-D composites was evaluated within a practical framework, where TBC at the Cu-D interface was examined as one of several key factors influencing overall thermal transport. Despite using relatively large diamond particles (405 µm), the overall performance of the uncoated composites remained lower than pure copper, consistent with previously reported thermal conductivity values for electrodeposited Cu-D materials [42], [44]. Introducing TiC interfacial coatings on the diamond particles led to a clear improvement in heat sink performance, demonstrating that appropriate interfacial engineering can enhance phonon transmission and overall thermal transport. The replicated performance trends, together with the improvement from TiC coatings, confirm that electrodeposited Cu-D composites can function

effectively as heat sink materials in electronic applications when suitable interface modifications are applied.

Chapter 5: Engineering Thermal Interface Materials and its Effect on the Performance of Metal-Based Heat Sink Materials

The previous chapter evaluated the heat sink performance of electrodeposited Cu-D composites, demonstrating how material design and diamond interfacial coatings influence the ability for these materials to lower device temperature. The insights gained from the previous chapter provided a foundation for a follow-up work in this chapter, which focuses on the interface between the heat sink and electronic components, extending the discussion from heat sink material design to system-level heat sink implementation. In practical applications, the thermal management performance of a cooling system is not only determined by the heat sink material but also by the thermal interface material (TIM) that couples the heat source to the heat sink. Commercial TIMs, while widely used and generally effective, still exhibit characteristics such as porosities and low thermal conductivity, all of which can influence the overall thermal performance of the assembly [142], [143]. To investigate whether the performance of a commercial TIM can be improved further, this chapter examines the effect of incorporating diamond particles into commercially available thermal paste. The goal is to assess how these diamond-modified formulations affect the quality of the interface and the steady-state temperature of the LED–heat-sink system, thereby determining whether enhancements beyond the base performance of the commercial TIM can be achieved.

5.1 Thermal Interface Materials Used in This Chapter

A commercially available thermal paste (SYY-157) was selected as the base thermal interface material (TIM) in this chapter owing to its established use in electronic cooling applications. The paste has a thermal conductivity of 15.7 $W \cdot m^{-1} \cdot K^{-1}$ according to the manufacturer. Its matrix is silicone and has carbon-based particles (likely graphite), which serve as the primary thermally conductive filler. Numerous voids and low-density regions are distributed throughout the paste matrix, disrupting continuous heat-transfer pathways and reducing the effective contact area between the LED and the heat sink. An optical micrograph illustrating the presence of such pores is shown in **Figure 5.1**. These voids increase the thermal resistance of TIM layer. To account for uncertainty associated with optical contrast limitations, the pore population was quantified using manual ImageJ point counting to establish lower and upper bounds, yielding a density of approximately 3.7×10^2 to 2.0×10^3 pores/mm^2 (**Appendix A.4).** While a rough pore density was

estimated using ImageJ, the associated uncertainty is high due to optical contrast limitations. Therefore, no direct quantitative comparison to the diamond volume fraction was made. Instead, the pores are qualitatively identified as a contributing factor to the relatively lower thermal performance of the as-received paste.

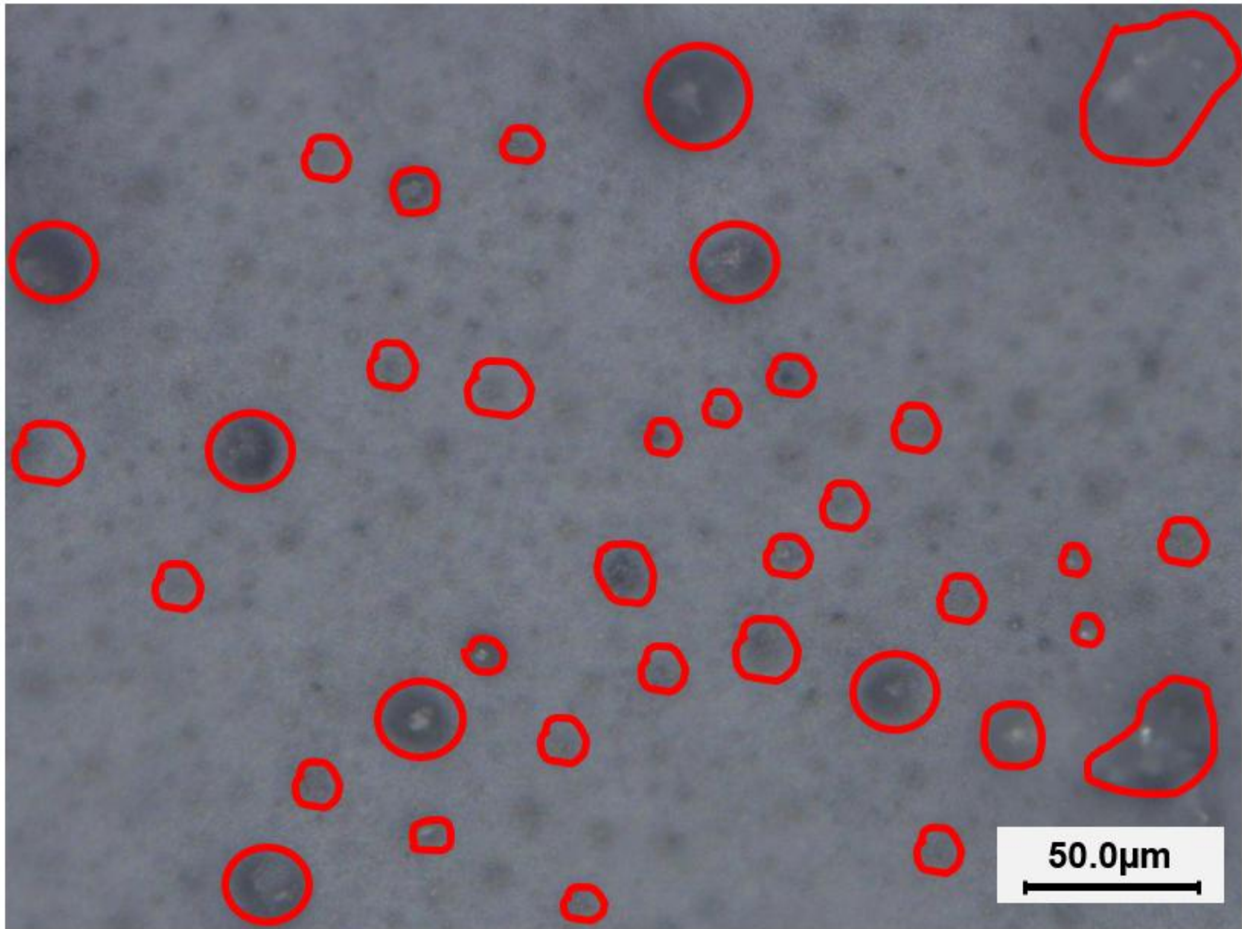

Figure 5.1: Optical micrograph of the commercial SYY thermal paste showing some pore regions highlighted.

Such microstructural features are typical characteristics of silicone-based thermal pastes, which often contain isolated pore regions that can interrupt continuous heat-transfer pathways and contribute to their low thermal conductivity [144]. These observations motivated the investigation of whether the TIM layer could be improved by increasing the proportion of continuous solid pathways across the TIM interfaces to enhance its effective thermal conductivity. Incorporating diamond particles increases the solid volume fraction of the TIM and consequently reduces the overall pore fraction of the TIM mixture, in addition to the diamond being an excellent heat

conductor. As a result, the effective thermal conductivity of the TIM layer improves, with the magnitude of enhancement depending on particle loading and interfacial resistance.

5.2 Results and discussion

Before evaluating the thermal performance of the diamond-modified TIMs, it is necessary to quantify the thickness of each applied TIM layer, as the thermal resistance of a TIM is directly proportional to its bond-line thickness (**Appendix A.6**), which is affected by the viscosity of the TIM and its respective diamond contents. The thickness of each TIM layer was measured from side-view optical micrographs using ImageJ. The copper heat sinks thickness (2.15 mm), measured using a caliper, was used to calibrate each image. The average of these measurements over all four sides was used to determine the overall bond-line thickness. An example of TIM thickness measurement is shown in **Figure 5.2**.

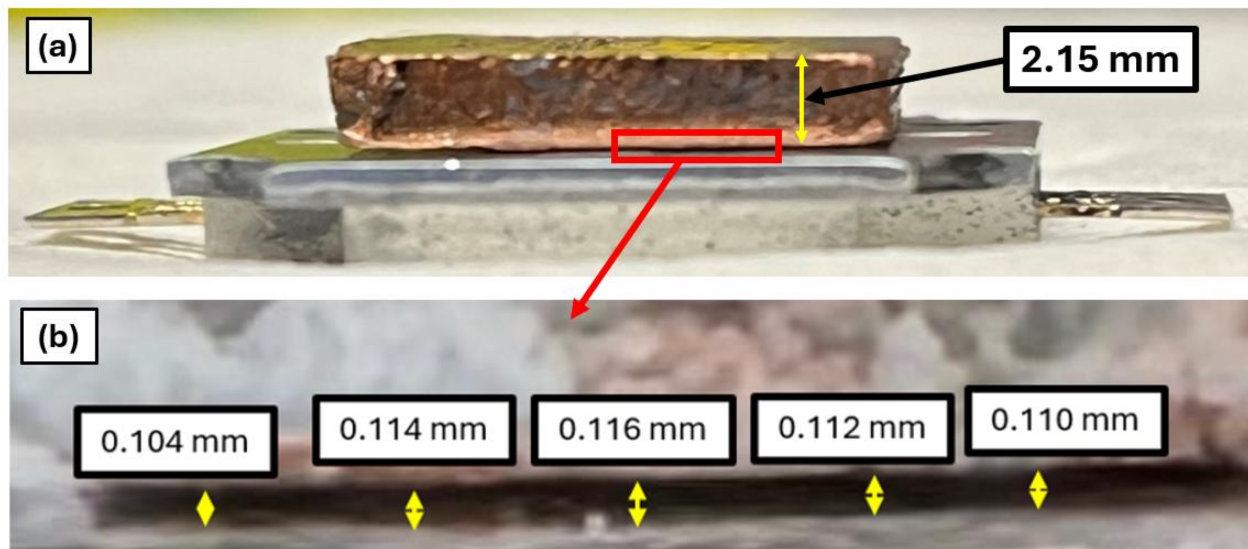

Figure 5.2: (a) Pixel-to-length calibration in ImageJ using the known copper heat sink thickness (2.15 mm). (b) Representative thickness measurements of the TIM layer obtained from the calibrated image.

The measured TIM bond-line thickness is shown in **Figure 5.3** for the baseline thermal paste (0 wt.% diamond) and the higher diamond loadings (10, 20, & 30 wt.%). A substantial increase in bond-line thickness is observed at 30 wt.% diamond loading compared to the unfilled thermal paste. This behavior is expected, as the addition of rigid solid particles increases the effective viscosity of the composite, reducing its ability to flow and compress during mounting.

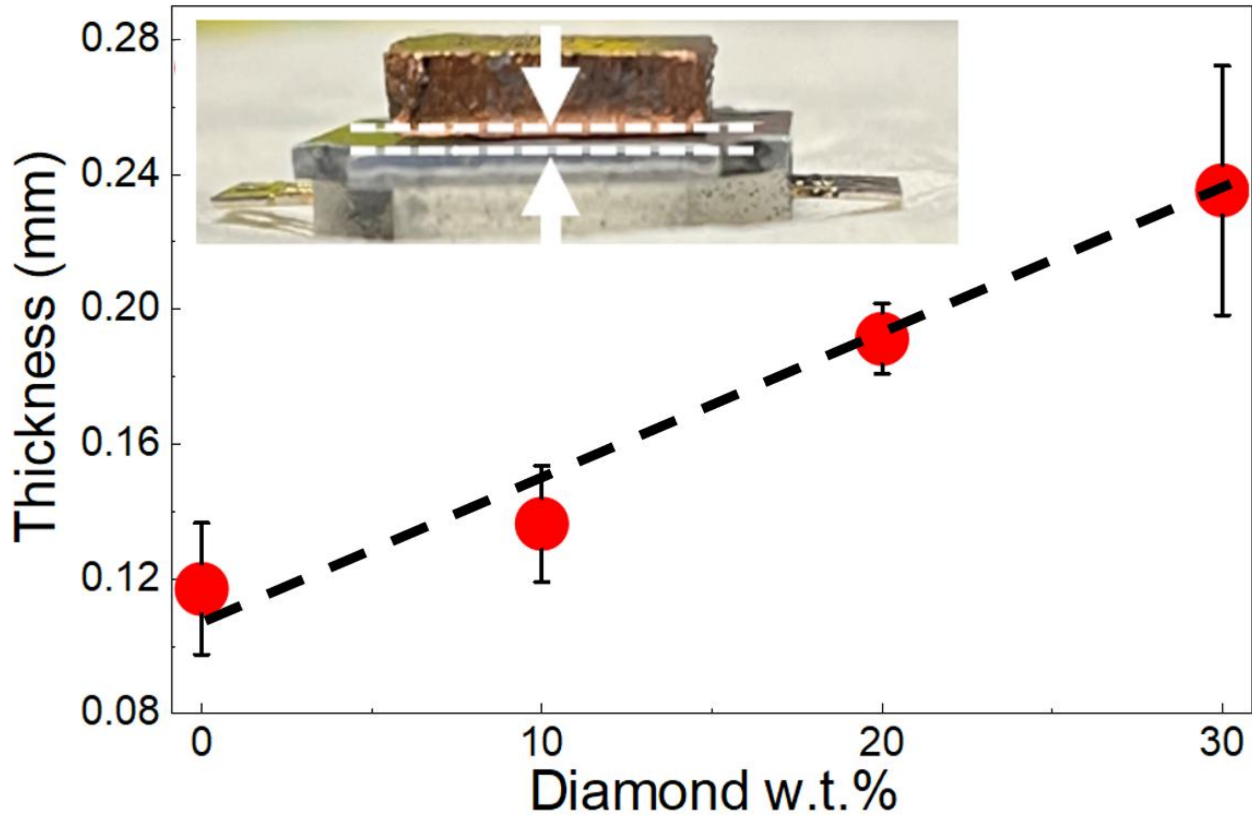

Figure 5.3: Measured TIM bond-line thickness for the baseline thermal paste (0 wt.% diamond) and the higher diamond loadings (10, 20, & 30 wt.%).

The results of the thermal performance evaluation are presented in **Figure 5.4** and summarized in **Table 5.1**. **Figure 5.4** shows the corresponding temperature–time results, while **Table 5.1** provides the numerical steady-state values for each thermal interface material (TIM) condition. The commercial paste and all diamond-modified formulations (10 wt.%, 20 wt.%, and 30 wt.%) were each repeated three separate times entirely to account for potential human-related variations in TIM application (e.g., manual preparation of mixtures, differences in particle distribution, and inconsistencies in spreading). Due to these practical factors, all TIMs, commercial and diamond-containing, exhibited some degree of trial-to-trial variability errors. Nevertheless, a clear and consistent trend emerged: increasing the diamond content further improves heat sink performance.

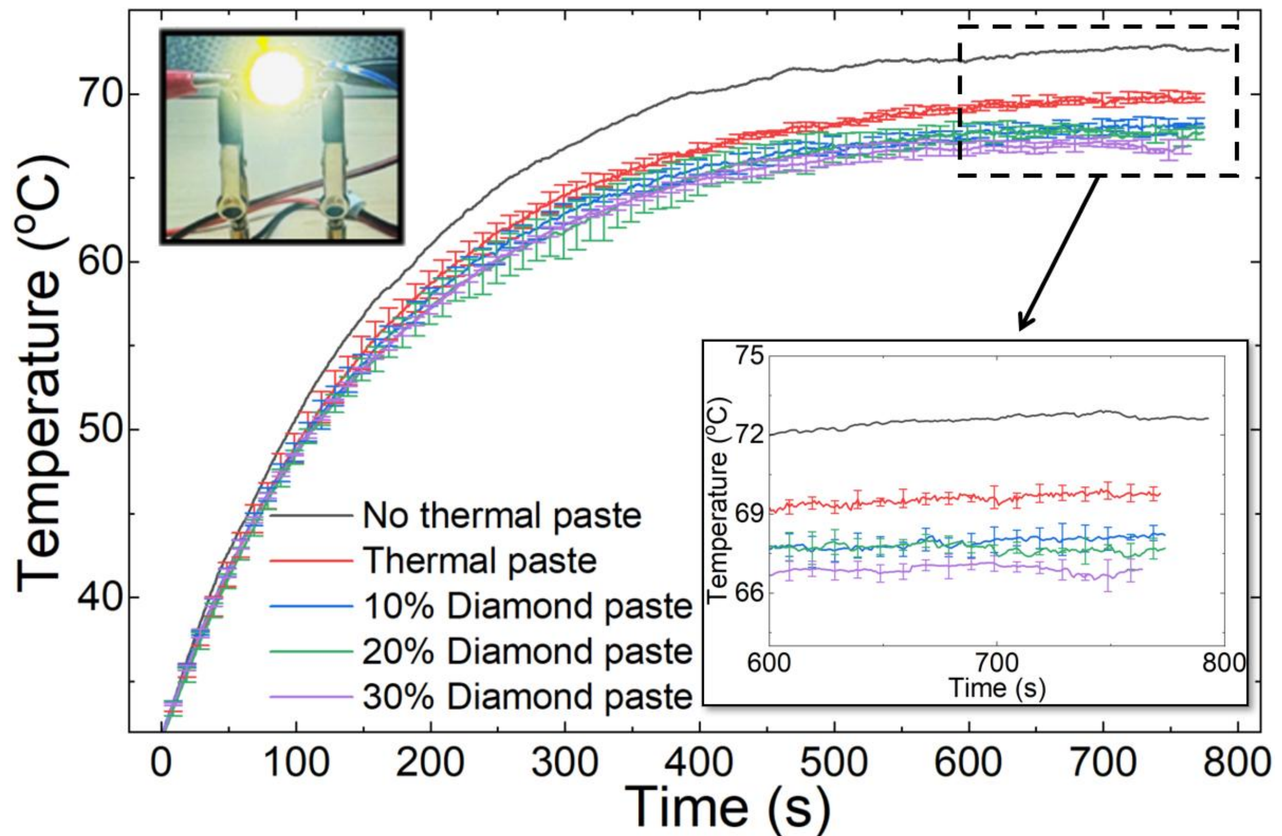

Figure 5.4: Transient LED temperature as a function of diamond wt.% for different thermal interface materials (TIMs). Corresponding LED steady-state temperatures are shown in the inlet. Error bars represent the standard deviation across three independent trials.

Table 5.1 – Steady-state LED temperatures of different TIMs, calculated from the average temperature of the last 30 seconds in the plateau. The uncertainties are the standard deviations from the three trials and thermocouple stability.

TIM	Steady-state temp.
Heat sink alone (no TIM)	72.64 ± 0.03 ºC
Thermal paste	69.70 ± 0.25 ºC
10% diamond paste	68.21 ± 0.30 ºC
20% diamond paste	67.58± 0.32 ºC
30% diamond paste	66.73 ± 0.15 ºC

When tested without any TIM, the LED reached a steady-state temperature of 72.64 ± 0.03 °C. Applying the commercial thermal paste reduced the temperature to 69.70 ± 0.25 °C, confirming

that even a conventional TIM provides a meaningful reduction in interfacial thermal resistance. The 10 wt.% diamond paste achieved a steady-state temperature of 68.21 ± 0.30 °C, already better than the commercial paste. The 20 wt.% formulation provided a more substantial improvement, reducing the temperature to 67.58 ± 0.32 °C. The best performance was obtained with the 30 wt.% diamond paste, which reached 66.73 ± 0.15 °C, representing a 3 °C reduction relative to the pure thermal paste. At first consideration, these outcomes may look surprising. Measurements provided earlier indicated that increasing diamond loadings produced progressively thicker TIM layers, which would lead to increased interface resistance and worse thermal performance. This behavior would align with results in **Appendix A.5** showing that thicker TIM layers lead to higher steady-state temperature. The experimental findings, however, indicate an opposite pattern. The improved thermal performance of the diamond-modified TIMs shows that the increase in effective thermal conductivity provided by the diamond particles outweighs the drawback of a thicker bond-line. As a highly conductive filler, diamond is expected to introduce additional heat-transfer pathways within the paste. While the presence of diamond particles may partially reduce low-conductivity regions such as pores, this effect was not directly quantified in the present work and should therefore be considered a plausible contributing mechanism rather than a confirmed outcome. Future work involving quantitative pore analysis would help clarify the extent to which diamond addition alters the void structure of the TIM. The progressive decrease in temperature with increasing diamond fraction is consistent with improved thermal transport, suggesting that the enhancement in effective TIM conductivity offsets the thermal resistance associated with a thicker bondline. In essence, the thermal benefit of diamond addition exceeds the performance penalty introduced by the increased interface thickness. Importantly, these results highlight a clear opportunity for further optimization, as reducing the thickness of diamond-enhanced TIMs through improved compression or refined paste formulations would likely yield additional gains in thermal performance.

5.3 Contribution from this chapter

This chapter demonstrated that the commercial SYY-157 thermal paste can be reinforced with small synthetic diamond particles to improve the thermal performance. Diamond-modified TIMs were then developed by incorporating 10, 20, and 30 wt.% diamond particles into the thermal paste. Although higher diamond loadings resulted in thicker bond-line layers, all diamond-TIM

formulations outperformed the commercial paste. Steady-state LED temperatures decreased progressively with increasing diamond content, reaching 68.21 °C, 67.58 °C, and 66.73 °C for 10, 20, and 30 wt.%, compared to 69.70 °C for the unmodified paste, respectively. These results indicate that the improved heat conduction pathways provided by diamond offer better thermal performance that offsets the issue of increased thickness. Overall, diamond incorporation significantly enhances TIM performance, and further reductions in bond-line thickness are expected to yield even greater thermal improvements.

Chapter 6: Conclusion and Future Work

6.1 Conclusions

This thesis investigated the heat sink performance of electrodeposited Cu-D composites, replicating Cu-D thermal conductivities published by Dr. Cho in practical heat sink performance and examining how intermetallic coatings, composite microstructure, and thermal interface materials collectively influence the heat-removal performance for practical electronic applications.

The experimental results revealed that although electrodeposition can produce defect-free Cu-D interfaces without cracks or voids, a pristine interface alone does not ensure high thermal boundary conductance and consequently, better heat sink performance. The copper grain microstructure, particularly the lack of columnar texture at the interface, limited phonon transport. As such, composites fabricated with uncoated diamond particles exhibited higher steady-state LED temperatures compared to pure copper heat sinks, indicating that the effective TBC at the electrodeposited Cu-D interfaces was below the ~2.6 $MW/m^2 \cdot K$ threshold required for conductivity enhancement as predicted by the Differential Effective Medium (DEM) model.

In contrast, a significant improvement in thermal performance was achieved using TiC-coated diamond particles. The multilayered Cu-D composite with TiC coatings recorded the lowest LED steady-state temperature (76.97 °C), representing a 4.46 °C reduction relative to pure copper and an 8.30 °C reduction compared to aluminum under identical conditions. These findings confirm that interfacial modification with intermediate coatings such as TiC, which are known to effectively bridge the vibrational mismatch between copper and diamond [42], [78], [80], [90], [104], [133], [137], is important for enhancing phonon coupling and interfacial heat transport. Additionally, the relatively high diamond volume fractions in the multilayer composites contributed to the observed thermal improvements, consistent with composite heat-transfer models in which increased particle loading enhances effective conductivity when interfacial resistance is sufficiently minimized. These observations demonstrate that electrodeposition can produce high-performance, application-ready metal–diamond heat sinks under ambient conditions through proper interfacial engineering and diamond particle distributions.

In addition to microstructural and interfacial engineering, this thesis also examined the influence of thermal interface materials (TIMs) on overall heat sink performance. Image-based pore analysis showed that the commercial silicone-based SYY paste contained 3.7×10^2 to 2.0×10^3 pores/mm^2, limiting its effective thermal transport capability. Incorporating 10–30 wt.% diamond particles into the paste produced progressively improved thermal performance, reducing the steady-state LED temperature from 69.70 °C (commercial paste) to 66.73 °C (30 wt.% diamond), despite the associated increase in bond-line thickness. These results demonstrate that the enhanced solid conduction pathways introduced by diamond more than offset the thickness penalty and highlight TIM formulation as an additional pathway for improving heat sink behavior in Cu-D systems.

Overall, this work extends previously reported thermal conductivity values of electrodeposited Cu-D composites and advances them toward practical heat sink applications. It shows that high-performance Cu-D materials can be achieved through a combination of interfacial engineering, microstructure optimization, and tailored thermal interface materials. Together, these findings demonstrate that electrodeposition remains a scalable, cost-effective method for producing next-generation passive cooling components and that further improvements are attainable through continued refinement of deposition parameters and TIM design.

6.2 Future Work

6.2.1 Thermo-Mechanical Reliability and Long-Term Stability

For electrodeposited Cu-D composites to be adopted in real heat sink applications, their long-term stability under thermal hysteresis cycles must be studied. While this work demonstrated promising steady-state heat sink performance, future studies should evaluate the durability and structural integrity of Cu-D composites when exposed to repetitive temperature fluctuations, thermomechanical loading, and environmental aging. Repeated heating and cooling cycles during device operation can induce thermal fatigue at the Cu–diamond interfaces due to the large mismatch in the coefficients of thermal expansion (CTE) between copper ($\sim 17 \times 10^{-6}$ K^{-1} [145]) and diamond ($\sim 1 \times 10^{-6}$ K^{-1} [145]). Such cycling may lead to gradual formation of microcracks, delamination, or voids at the interface, ultimately increasing interfacial thermal resistance. To quantify these effects, thermal-cycling and hysteresis testing should be performed within representative temperature ranges (e.g., 25–150 °C), monitoring any progressive change in thermal

resistance or heat sink performance. Analytical methods such as transient thermal impedance or in-situ infrared thermography can be used to capture degradation dynamics in real time [4].

Environmental factors also play a critical role in long-term stability. Exposure to elevated humidity or oxygen at high temperature can promote oxidation and corrosion of the copper matrix, compromising bonding strength and electrical contact. High-temperature storage (e.g., 200 °C in air) is recommended to assess oxidation resistance and interfacial adhesion, particularly for coated systems such as TiC-modified Cu-D composites. Complementary mechanical testing, using nano-indentation or micro-shear adhesion methods, can reveal how interface strength evolves with aging and cycling [146].

Another important aspect of reliability assessment is the measurement of the effective CTE of the Cu-D composite. As the diamond volume fraction, coating type, and interfacial quality change, the overall CTE can deviate from theoretical predictions, affecting stress evolution during temperature excursions. Accurate determination of CTE using thermomechanical analysis (TMA) or high-temperature X-ray diffraction would enable predictive modeling of stress distributions in integrated Cu-D/semiconductors. Through a combination of accelerated thermal-cycling, environmental exposure, and thermo-mechanical characterization, future research can reveal the dominant degradation mechanisms and define the operational limits of electrodeposited Cu-D heat sinks. Establishing reliable data will be critical for translating laboratory-scale composites into industrialized, high-performance thermal-management materials.

6.2.2 Fabrication of Fin-Shaped and Structured Copper–Diamond Composites

Translating electrodeposited Cu-D composites from laboratory-scale heat sinks to real-world heat sink architectures requires developing scalable fabrication strategies that retain microstructural integrity while enabling efficient heat removal. One of the most promising directions is the creation of fin-shaped or structured Cu-D geometries, which are widely recognized as the most effective configuration for heat sink applications. Fin structures maximize the surface area available for convective heat transfer, allowing more efficient removal of heat into the surrounding environment. This geometry also enhances airflow distribution and reduces thermal resistance, leading to superior overall heat-spreading capability compared to flat or solid designs.

A practical and adaptable method that could be explored involves first electrodepositing thick Cu-D composite blocks under optimized electrodeposition conditions, followed by laser cutting or micromachining to form the desired fin structure, as illustrated in **Figure 6.1**. This proposed fabrication route would enable precise shaping of the electrodeposited composite without compromising its internal Cu-D microstructure or the strong interfacial bonding achieved during electrodeposition. After cutting, post-processing and polishing steps could be employed to minimize surface irregularities and heat-affected zones, ensuring smooth heat transfer across the fin base. This combination of electrodeposition and precision machining would provide a flexible pathway to produce customized, high-surface-area heat sinks while maintaining the superior interfacial properties intrinsic to the Cu-D composite structure.

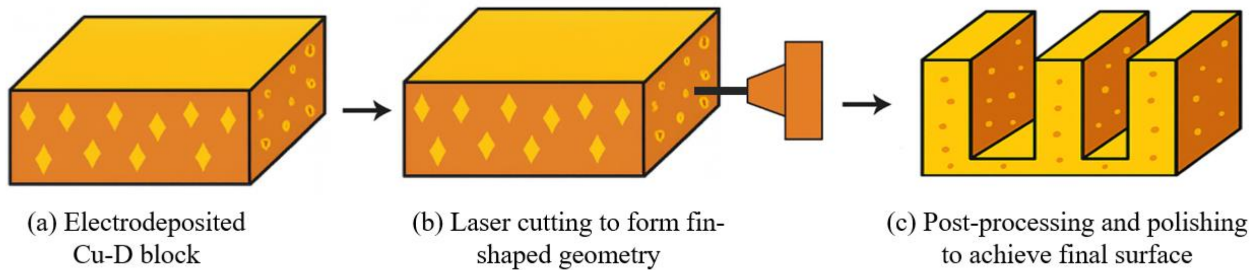

Figure 6.1: Schematic illustration of the proposed fabrication route for fin-shaped Cu-D composite heat sinks: (a) electrodeposition of a thick Cu-D composite block, (b) laser cutting fin geometries, and (c) post-processing and polishing to achieve final surface finish.

However, while this approach serves as an effective proof of concept, it involves considerable material loss and additional processing time due to laser cutting. For practical scalability and cost-effectiveness, future work should therefore focus on developing a direct electrodeposition or electroforming process capable of producing fin geometries in situ without the need for bulk post-machining. This can be achieved using 3D-printed or microfabricated conductive molds that define the fin architecture before deposition. By co-depositing copper and diamond particles within these pre-defined molds, near-net-shape Cu-D fins could be fabricated. Such a mold-assisted electrodeposition process, if successful, would drastically reduce material waste, maintain

geometric precision, and enable scalable manufacturing of complex, high-surface-area heat sinks, as illustrated in **Figure 6.2**.

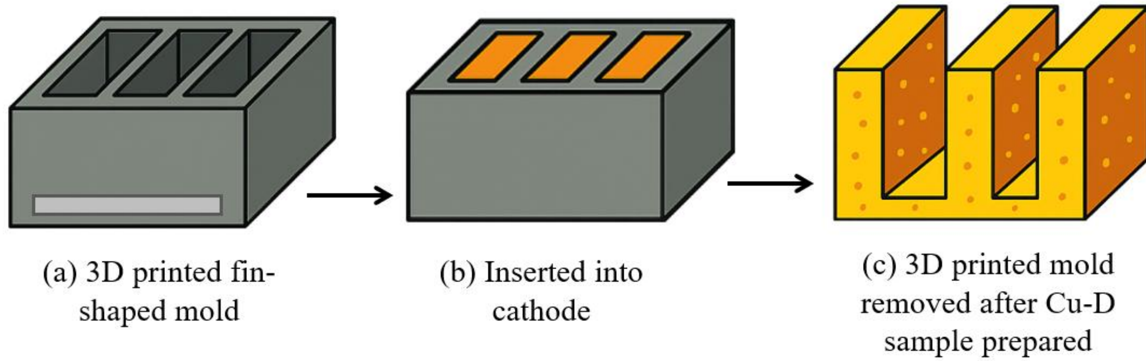

Figure 6.2: Schematic illustration of the proposed mold-assisted electrodeposition route for fabricating fin-shaped Cu-D composites: (a) 3D-printed fin-shaped mold, (b) mold inserted into the cathode for electrodeposition, and (c) removal of the mold after deposition to reveal the final Cu-D fin structure.

References:

[1] G. E. Moore, "Cramming More Components onto Integrated Circuits," 1965.

[2] International Technology Roadmap for Semiconductors, "International Technology Roadmap for Semiconductors: ITRS Reports."

[3] "Multigate transistors as the future of classical metal–oxide–semiconductor field-effect transistors."

[4] A. L. Moore, L. Shi, "Emerging challenges and materials for thermal management of electronics," *Materials Today*, 2014.

[5] Samsung Electronics, "Samsung Begins Chip Production Using 3nm Process Technology With GAA Architecture," Samsung Newsroom, 2022.

[6] TSMC, "3 nm technology," Taiwan Semiconductor Manufacturing Company Ltd, 2022.

[7] Y. Li, J. Chen, S. Zhao, J. Song, "Recent advances on thermal management of flexible inorganic electronics," *Micromachines*, vol. 11 (4), 2020.

[8] Y. Wen, C. Basaran, "Thermomechanical stress analysis of multi-layered electronic packaging," *Journal of Electronic Packaging*, vol. 125 (1), pp. 134–138, 2003.

[9] W. Haensch et al., "Silicon CMOS devices beyond scaling," 2006.

[10] P. K. Schelling, L. Shi, K. E. Goodson, "Managing heat for electronics," 2004.

[11] A. Reuther et al., "AI and ML Accelerator Survey and Trends," *IEEE High Performance Extreme Computing Conference (HPEC)*, 2019.

[12] V. Panchal, "Thermal and Power Management Challenges in High-Performance Mobile Processors," *International Journal of Innovative Research in Science, Engineering and Technology*, vol. 13 (11), 2024.

[13] "Moore's law has accurately predicted the progress in transistor counts over the last 50 years," 2024.

[14] R. Priday, "Samsung is throttling the Galaxy S23's performance — what you need to know," Tom's Guide, 2023.

[15] A. Osthoff, "Apple MacBook Pro 14 2023 review: The M2 Pro is slowed down in the small MacBook Pro," Notebookcheck, 2023.

[16] A. E. Freedman, "Asus ROG Zephyrus G14 (2024) review: Portability over power," Tom's Hardware, 2024.

[17] A. Cunningham, "In-depth with the Snapdragon 810's heat problems," Ars Technica, 2015.

[18] J. Hiner, "iPhone 15 Pro overheating: Thermal photos before and after iOS 17.0.3," ZDNet, 2023.

[19] S. Nižetić, M. Jurčević, D. Čoko, M. Arıcı, “A novel and effective passive cooling strategy for photovoltaic panel,” *Renewable and Sustainable Energy Reviews*, vol. 145, 2021.

[20] F. Grubišić-Čabo, S. Nižetić, I. Marinić Kragić, D. Čoko, “Further progress in the research of fin-based passive cooling technique for the free-standing silicon photovoltaic panels,” *International Journal of Energy Research*, vol. 43 (8), pp. 3475–3495, 2019.

[21] C. Y. Ho, I. R. W. Powell, P. E. Liley, “Thermal Conductivity of the Elements,” *Journal of Physical and Chemical Reference Data*.

[22] J. F. Silvain, A. Veillère, Y. Lu, “Copper-carbon and aluminum-carbon composites fabricated by powder metallurgy processes,” *Journal of Physics: Conference Series*, vol. 525 (1), 2014.

[23] A. Zhang, Y. Li, “Thermal Conductivity of Aluminum Alloys—A Review,” *Materials*, vol. 16 (8), 2023.

[24] I. Oropeza-Perez, P. A. Østergaard, “Active and passive cooling methods for dwellings: A review,” *Renewable and Sustainable Energy Reviews*, 2018.

[25] N. Ali, A. M. Bahman, N. F. Aljuwayhel, S. A. Ebrahim, S. Mukherjee, A. Alsayegh, “Carbon-Based Nanofluids and Their Advances towards Heat Transfer Applications—A Review,” *Nanomaterials*, vol. 11 (6), 2021.

[26] S. V. Kidalov, F. M. Shakhov, “Thermal conductivity of diamond composites,” *Materials*, vol. 2 (4), pp. 2467–2495, 2009.

[27] C. Ye, B. Shentu, Z. Weng, “Thermal conductivity of high density polyethylene filled with graphite,” *Journal of Applied Polymer Science*, vol. 101 (6), pp. 3806–3810, 2006.

[28] A. A. Balandin et al., “Superior Thermal Conductivity of Single-Layer Graphene,” *Nano Letters*, vol. 8 (3), pp. 902–907, 2008.

[29] Sigma-Aldrich Co. LLC, “Single, Double, and Multi-Walled Carbon Nanotubes.”

[30] D. Yoon, Y.-W. Son, H. Cheng, “Negative thermal expansion coefficient of graphene measured by Raman spectroscopy,” *Nano Letters*, vol. 11 (8), pp. 3227–3231, 2011.

[31] S. Q. Jia, F. Yang, “High thermal conductive copper/diamond composites: state of the art,” *Journal of Materials Science*, vol. 56 (3), pp. 2241–2274, 2021.

[32] Z. Jiao et al., “Research progress of diamond/aluminum composite interface design,” *Functional Diamond*, vol. 2 (1), pp. 25–39, 2022.

[33] J. Choi, M. Jeong, “Compact, lightweight, and highly efficient circular heat sink design for high-end PCs,” *Applied Thermal Engineering*, vol. 92, pp. 162–171, 2016.

[34] P. W. Ruch, O. Beffort, S. Kleiner, L. Weber, P. J. Uggowitzer, “Selective interfacial bonding in Al(Si)-diamond composites and its effect on thermal conductivity,” *Composites Science and Technology*, vol. 66 (15), pp. 2677–2685, 2006.

[35] I. E. Monje, E. Louis, J. M. Molina, "Optimizing thermal conductivity in gas-pressure infiltrated aluminum/diamond composites by precise processing control," *Composites Part A: Applied Science and Manufacturing*, vol. 48, pp. 9–14, 2013.

[36] Q. L. Che et al., "Spark plasma sintering of titanium-coated diamond and copper-titanium powder to enhance thermal conductivity of diamond/copper composites," *Materials Science in Semiconductor Processing*, vol. 33, pp. 67–75, 2015.

[37] F. C. Walsh, C. Ponce De Leon, "A review of the electrodeposition of metal matrix composite coatings by inclusion of particles in a metal layer: An established and diversifying technology," *Transactions of the Institute of Metal Finishing*, vol. 92 (2), pp. 83–98, 2014.

[38] H. J. Cho, J. Tam, M. Kovylina, Y. J. Kim, U. Erb, "Thermal conductivity of bulk nanocrystalline nickel-diamond composites produced by electrodeposition," *Journal of Alloys and Compounds*, vol. 687, pp. 570–578, 2016.

[39] S. Wang et al., "Thermal conductivity and electrical resistivity in polycrystalline and nanocrystalline nickel," *Advanced Materials Research*, vol. 409, pp. 561–565, 2012.

[40] C. Ken, D. Barker, F. Walsh, J. Archer, "The electrodeposition of composite coatings based on metal matrix-included particle deposits," *Transactions of the Institute of Metal Finishing*, vol. 78 (5), pp. 171–178, 2000.

[41] Y. Wu et al., "Critical effect and enhanced thermal conductivity of Cu-diamond composites reinforced with various diamond prepared by composite electroplating," *Ceramics International*, vol. 45 (10), pp. 13225–13234, 2019.

[42] H. J. Cho, Y. J. Kim, U. Erb, "Thermal conductivity of copper-diamond composite materials produced by electrodeposition and the effect of TiC coatings on diamond particles," *Composites Part B: Engineering*, vol. 155, pp. 197–203, 2018.

[43] Y. Wu, L. Lai, Y. Wang, H. Wang, G. Ding, "Optimization of external and internal conditions for high thermal conductive Cu-diamond composites produced by electroplating," *Diamond and Related Materials*, vol. 98, 2019.

[44] H. J. Cho, D. Yan, J. Tam, U. Erb, "Effects of diamond particle size on the formation of copper matrix and the thermal transport properties in electrodeposited copper-diamond composite materials," *Journal of Alloys and Compounds*, vol. 791, pp. 1128–1137, 2019.

[45] Y. Wu et al., "Microstructure of Cu-diamond composites with near-perfect interfaces prepared via electroplating and its thermal properties," *Materials Characterization*, vol. 150, pp. 199–206, 2019.

[46] S. Arai, M. Ueda, "Fabrication of high thermal conductivity Cu/diamond composites at ambient temperature and pressure," *AIP Advances*, vol. 9 (8), 2019.

[47] S. Arai, M. Ueda, “Fabrication of high thermal conductivity copper/diamond composites by electrodeposition under potentiostatic conditions,” *Journal of Applied Electrochemistry*, vol. 50 (5), pp. 631–638, 2020.

[48] S. Arai, M. Ueda, “Fabrication of high thermal conductivity copper/diamond composites by electrodeposition under potentiostatic conditions,” *Journal of Applied Electrochemistry*, vol. 50 (5), pp. 631–638, 2020.

[49] S. B. Sadineni, S. Madala, R. F. Boehm, “Passive building energy savings: A review of building envelope components,” *Renewable and Sustainable Energy Reviews*, vol. 15 (8), pp. 3617–3631, 2011.

[50] F. P. Incropera, D. P. DeWitt, *Fundamentals of Heat and Mass Transfer*, Wiley, 2002.

[51] A. A. Pesaran, M. Keyser, S. Burch, “Cooling and preheating of batteries in hybrid electric vehicles,” *SAE Technical Paper*, 2002.

[52] D. G. Gilmore, *Spacecraft Thermal Control Handbook, Volume I: Fundamental Technologies*, 2002.

[53] A. R. Dhumal, A. P. Kulkarni, N. H. Ambhore, “A comprehensive review on thermal management of electronic devices,” *Journal of Engineering and Applied Science*, 2023.

[54] I. Oropeza-Perez, P. A. Østergaard, “Active and passive cooling methods for dwellings: A review,” *Renewable and Sustainable Energy Reviews*, 2018.

[55] A. R. Gentle, G. B. Smith, “Radiative heat pumping from the earth using surface phonon resonant nanoparticles,” *Nano Letters*, 2010.

[56] King, “What Is The Main Obstacle To Using Passive Heat Sinks?”

[57] K. De Vogeleer, G. Memmi, P. Jouvelot, F. Coelho, “Theoretical Analysis of Radiative Cooling for Mobile and Embedded Systems,” 2015.

[58] Italia, Ronak, “An Analysis of Heat Dissipation Techniques in Power Electronics,” *Journal of Engineering and Applied Sciences Technology*, pp. 1–6, 2023.

[59] J. W. Wei, K. Zhang, L. Xu, “Advanced thermal management techniques in power electronics,” *IEEE Transactions on Industrial Electronics*, 2020.

[60] Q. Xu et al., “Enhanced thermal management of power devices using liquid cooling techniques,” *IEEE Transactions on Power Electronics*, 2017.

[61] J. H. Lee, B. H. Cho, “Study on the thermal behavior of power electronic devices with advanced cooling techniques,” *IEEE Transactions on Power Electronics*, 2019.

[62] W. L. Staats, J. G. Brisson, “Active heat transfer enhancement in air cooled heat sinks using integrated centrifugal fans,” *International Journal of Heat and Mass Transfer*, vol. 82, pp. 189–205, 2015.

[63] P. Shahi et al., “Assessment of reliability enhancement in high-power CPUs and GPUs using dynamic direct-to-chip liquid cooling,” *Journal of Enhanced Heat Transfer*, vol. 29 (8), pp. 1–13, 2022.

[64] A. A. Pesaran, “Battery thermal management in EVs and HEVs: Issues and solutions,” *Advanced Automotive Battery Conference*, 2001.

[65] “Understanding Thermal Impedance and Thermal Conductivity in Thermal Interface Materials,” 2023.

[66] E. O. Hercus, T. H. Laby, “The thermal conductivity of air,” *Proceedings of the Royal Society of London A*, 1919.

[67] “Heatsink attachment options,” 2008.

[68] “Thermal Conductivities of Common Metals, Metallic Elements and Alloys,” The Engineering ToolBox.

[69] Y. Tu, B. Liu, G. Yao, “A review of advanced thermal interface materials with oriented structures for electronic devices,” *Electronics*, 2024.

[70] W. Xing, Y. Xu, C. Song, T. Deng, “Recent advances in thermal interface materials for thermal management of high-power electronics,” *Nanomaterials*, 2022.

[71] S. Chambers, “What are thermal interface materials?,” 2020.

[72] D. D. L. Chung, “A critical review of carbon-based thermal interface materials,” *Materials Chemistry and Physics*, 2023.

[73] “Heat Sink Attachment Hardware,” MyHeatsinks.com.

[74] F. Hua, C. Deppisch, “Solder as thermal interface material for high power devices,” *Journal of Surface Mount Technology*, 2006.

[75] M. Singh, R. Asthana, T. P. Shpargel, “Brazing of carbon–carbon composites to Cu-clad molybdenum for thermal management applications,” *Materials Science and Engineering A*, vol. 452–453, pp. 699–704, 2007.

[76] Thermal Processing, “Diffusion bonded printed circuit heat exchangers for severe environments,” 2025.

[77] Q. Wang et al., “High thermal conductivity diamond–copper composites prepared via hot pressing with tungsten–coated interfacial layer optimization,” *Materials*, vol. 18 (16), 2025.

[78] C. Chen et al., “Thermal conductivity of diamond/copper composites with a bimodal distribution of diamond particle sizes prepared by pressure infiltration method,” *Rare Metals*, vol. 30 (4), pp. 408–413, 2011.

[79] K. Chu et al., “Thermal conductivity of SPS consolidated Cu/diamond composites with Cr-coated diamond particles,” *Journal of Alloys and Compounds*, vol. 490 (1–2), pp. 453–458, 2010.

[80] C. Y. Chung, M. T. Lee, M. Y. Tsai, C. H. Chu, S. J. Lin, “High thermal conductive diamond/Cu-Ti composites fabricated by pressureless sintering technique,” *Applied Thermal Engineering*, vol. 69 (1–2), pp. 208–213, 2014.

[81] J. Li, H. Zhang, Y. Zhang, Z. Che, X. Wang, “Microstructure and thermal conductivity of Cu/diamond composites with Ti-coated diamond particles produced by gas pressure infiltration,” *Journal of Alloys and Compounds*, vol. 647, pp. 941–946, 2015.

[82] Z. Tan et al., “A predictive model for interfacial thermal conductance in surface metallized diamond aluminum matrix composites,” *Materials and Design*, vol. 55, pp. 257–262, 2014.

[83] R. Tavangar, J. M. Molina, L. Weber, “Assessing predictive schemes for thermal conductivity against diamond-reinforced silver matrix composites at intermediate phase contrast,” *Scripta Materialia*, vol. 56 (5), pp. 357–360, 2007.

[84] A. M. Abyzov, S. V. Kidalov, F. M. Shakhov, “High thermal conductivity composites consisting of diamond filler with tungsten coating and copper (silver) matrix,” *Journal of Materials Science*, vol. 46 (5), pp. 1424–1438, 2011.

[85] C. Li, X. Wang, L. Wang, J. Li, H. Li, H. Zhang, “Interfacial characteristic and thermal conductivity of Al/diamond composites produced by gas pressure infiltration in a nitrogen atmosphere,” *Materials and Design*, vol. 92, pp. 643–648, 2016.

[86] I. E. Monje, E. Louis, J. M. Molina, “Role of Al4C3 on the stability of the thermal conductivity of Al/diamond composites subjected to constant or oscillating temperature in a humid environment,” *Journal of Materials Science*, vol. 51 (17), pp. 8027–8036, 2016.

[87] Q. Kang et al., “Preparation of high thermal conductivity copper-diamond composites using molybdenum carbide-coated diamond particles,” *Journal of Materials Science*, vol. 48 (18), pp. 6133–6140, 2013.

[88] A. F. Zimmerman, G. Palumbo, K. T. Aust, U. Erb, “Mechanical properties of nickel silicon carbide nanocomposites,” *Materials Science and Engineering A*, 2002.

[89] Q. Kang et al., “Effect of molybdenum carbide intermediate layers on thermal properties of copper-diamond composites,” *Journal of Alloys and Compounds*, vol. 576, pp. 380–385, 2013.

[90] W. Yang, K. Peng, J. Zhu, D. Li, L. Zhou, “Enhanced thermal conductivity and stability of diamond/aluminum composite by introduction of carbide interface layer,” *Diamond and Related Materials*, vol. 46, pp. 35–41, 2014.

[91] A. Giri, B. Foley, P. Hopkins, “Influence of hot electron scattering and electron-phonon interactions on thermal boundary conductance at metal/nonmetal interfaces,” *Journal of Heat Transfer*, vol. 136, 2014.

[92] E. Kondakci, N. Solak, “Enhanced thermal conductivity and long-term stability of diamond/aluminum composites using SiC-coated diamond particles,” *Journal of Materials Science*, vol. 57 (5), pp. 3430–3440, 2022.

[93] P. Zhu et al., “Effect of interface structure on thermal conductivity and stability of diamond/aluminum composites,” *Composites Part A: Applied Science and Manufacturing*, vol. 162, 2022.

[94] Z. Tan et al., “Enhanced thermal conductivity in diamond/aluminum composites with a tungsten interface nanolayer,” *Materials and Design*, vol. 47, pp. 160–166, 2013.

[95] K. Mizuuchi et al., “Thermal conductivity of diamond particle dispersed aluminum matrix composites fabricated in solid-liquid co-existent state by SPS,” *Composites Part B: Engineering*, vol. 42 (5), pp. 1029–1034, 2011.

[96] L. Jiang et al., “Interfacial characteristics of diamond/aluminum composites with high thermal conductivity fabricated by squeeze-casting method,” *Materials Characterization*, vol. 106, pp. 346–352, 2015.

[97] C. Xue, J. K. Yu, “Enhanced thermal conductivity in diamond/aluminum composites: Comparison between the methods of adding Ti into Al matrix and coating Ti onto diamond surface,” *Surface and Coatings Technology*, vol. 217, pp. 46–50, 2013.

[98] J. Li, X. Wang, Y. Qiao, Y. Zhang, Z. He, H. Zhang, “High thermal conductivity through interfacial layer optimization in diamond particles dispersed Zr-alloyed Cu matrix composites,” *Scripta Materialia*, vol. 109, pp. 72–75, 2015.

[99] E. A. Ekimov, N. V. Suetin, A. F. Popovich, V. G. Ralchenko, “Thermal conductivity of diamond composites sintered under high pressures,” *Diamond and Related Materials*, vol. 17 (4–5), pp. 838–843, 2008.

[100] L. Wang et al., “Enhanced thermal conductivity in Cu/diamond composites by tailoring the thickness of interfacial TiC layer,” *Composites Part A: Applied Science and Manufacturing*, vol. 113, pp. 76–82, 2018.

[101] Y. Lu, X. Wang, Y. Zhang, J. Wang, M. J. Kim, H. Zhang, “Aluminum carbide hydrolysis induced degradation of thermal conductivity and tensile strength in diamond/aluminum composite,” *Journal of Composite Materials*, vol. 52 (20), pp. 2709–2717, 2018.

[102] K. Chu, C. Jia, H. Guo, W. Li, “Microstructure and thermal conductivity of Cu-B/diamond composites,” *Journal of Composite Materials*, vol. 47 (23), pp. 2945–2953, 2013.

[103] Y. Zhang, H. L. Zhang, J. H. Wu, X. T. Wang, “Enhanced thermal conductivity in copper matrix composites reinforced with titanium-coated diamond particles,” *Scripta Materialia*, vol. 65 (12), pp. 1097–1100, 2011.

[104] K. Raza, F. A. Khalid, “Optimization of sintering parameters for diamond-copper composites in conventional sintering and their thermal conductivity,” *Journal of Alloys and Compounds*, vol. 615, pp. 111–118, 2014.

[105] T. Guillemet, P. M. Geffroy, J. M. Heintz, N. Chandra, Y. Lu, J. F. Silvain, “An innovative process to fabricate copper/diamond composite films for thermal management applications,” *Composites Part A: Applied Science and Manufacturing*, vol. 43, pp. 1746–1753, 2012.

[106] V. Sinha, J. E. Spowart, “Influence of interfacial carbide layer characteristics on thermal properties of copper-diamond composites,” *Journal of Materials Science*, vol. 48 (3), pp. 1330–1341, 2013.

[107] K. Yoshida, H. Morigami, “Thermal properties of diamond/copper composite material,” *Microelectronics Reliability*, vol. 44, pp. 303–308, 2004.

[108] C. Chen et al., “Thermal conductivity of diamond/copper composites with a bimodal distribution of diamond particle sizes prepared by pressure infiltration method,” *Rare Metals*, vol. 30 (4), pp. 408–413, 2011.

[109] H. Chen, C. Jia, S. Li, “Effect of sintering parameters on the microstructure and thermal conductivity of diamond/Cu composites prepared by high pressure and high temperature infiltration,” *International Journal of Minerals, Metallurgy, and Materials*, vol. 20 (2), pp. 180–186, 2013.

[110] K. Mizuuchi et al., “Consolidation and thermal conductivity of diamond particle dispersed copper matrix composites produced by spark plasma sintering,” *Journal of the Japan Institute of Metals*, vol. 71 (11), pp. 1066–1069, 2007.

[111] L. Weber, R. Tavangar, “On the influence of active element content on the thermal conductivity and thermal expansion of Cu–X (X=Cr, B) diamond composites,” *Scripta Materialia*, vol. 57 (11), pp. 988–991, 2007.

[112] Y. Wu et al., “High thermal conductive Cu-diamond composites synthesized by electrodeposition and the critical effects of additives on void-free composites,” *Ceramics International*, vol. 45 (16), pp. 19658–19668, 2019.

[113] L. Zhou, R. Ding, J. Liu, K. Zhan, B. Zhao, V. Ji, “Preparation of micro-diamond/copper composite foils by direct current electro-deposition method and its properties,” *Diamond and Related Materials*, vol. 145, 2024.

[114] Y. Luo et al., “High thermal conductive Cu-diamond composite sheets reinforced with single-layer diamond prepared by a three-step electroplating process,” *Diamond and Related Materials*, vol. 152, 2025.

[115] JEDEC Solid State Technology Association, “Transient Dual Interface Test Method for the Measurement of the Thermal Resistance Junction-to-Case of Semiconductor Devices With Heat Flow Through a Single Path,” JESD51-14, 2010.

[116] JEDEC Solid State Technology Association, “Transient Dual Interface Test Method for the Measurement of Thermal Resistance Junction-to-Case of Semiconductor Devices,” JESD51-14, 2010.

[117] F. P. Incropera, T. L. Bergman, D. P. DeWitt, *Fundamentals of Heat and Mass Transfer*, 7th ed., Wiley, 2011.

[118] J. Z. Xu, B. Z. Gao, F. Y. Kang, “A reconstruction of Maxwell model for effective thermal conductivity of composite materials,” *Applied Thermal Engineering*, vol. 102, pp. 972–979, 2016.

[119] D. P. H. Hasselman, L. F. Johnson, “Effective thermal conductivity of composites with interfacial thermal barrier resistance,” *Journal of Composite Materials*, vol. 21 (6), pp. 508–515, 1987.

[120] D. A. G. Bruggeman, “Berechnung verschiedener physikalischer Konstanten von heterogenen Substanzen,” *Annalen der Physik*, vol. 416 (7), pp. 636–664, 1935.

[121] A. Kelly, C. Zweben, “Comprehensive composite materials,” *Materials Today*, vol. 2 (1), pp. 20–21, 1999.

[122] X. Zheng, Y. Liu, Y. Cao, J. Wang, Y. Zhang, “CVD synthesis of nanometer SiC coating on diamond particles,” *Ceramics International*, vol. 47 (11), pp. 16162–16169, 2021.

[123] K. J. Brown, E. Chartier, E. M. Sweet, D. A. Hopper, L. C. Bassett, “Cleaning diamond surfaces using boiling acid treatment in a standard laboratory chemical hood,” *Journal of Chemical Health and Safety*, vol. 26 (6), pp. 40–44, 2019.

[124] M. Mindel, S. Pollack, “The room temperature oxidation of titanium thin films,” *Acta Metallurgica*, 1969.

[125] S. Yoshimura, S. Yoshihara, T. Shirakashi, E. Sato, “Preferred orientation and morphology of electrodeposited iron from iron (II) chloride solution,” *Electrochimica Acta*, vol. 39, pp. 589–596, 1994.

[126] Q. Wang, Y. Peng, Y. Mou, M. Chen, “Promotion of high-speed copper-filling performance for interconnections with increasing aspect-ratio using compound additives,” *Micromachines*, vol. 13 (9), 2022.

[127] O. Kozaderov, N. Sotskaya, L. Yudenkova, N. Buylov, E. Ilina, “Electrocrystallization and morphology of copper coatings in the presence of organic additives,” *Coatings*, vol. 13 (11), 2023.

[128] A. Kelly, C. Zweben, “Comprehensive composite materials,” *Materials Today*, vol. 2 (1), pp. 20–21, 1999.

[129] E. T. Swartz, R. O. Pohl, “Thermal boundary resistance,” *Reviews of Modern Physics*, vol. 61 (3), pp. 605–668, 1989.

[130] L. Chen, S. Chen, Y. Hou, “Understanding the thermal conductivity of diamond/copper composites by first-principles calculations,” *Carbon*, vol. 148, pp. 249–257, 2019.

[131] B. Xu et al., “Scalable monolayer-functionalized nanointerface for thermal conductivity enhancement in copper/diamond composite,” *Carbon*, vol. 175, pp. 299–306, 2021.

[132] Z. Wang, F. Sun, Z. Liu, L. Zheng, D. Wang, Y. Feng, “Regulated thermal boundary conductance between copper and diamond through nanoscale interfacial rough structures,” *ACS Applied Materials and Interfaces*, vol. 15 (12), pp. 16162–16176, 2023.

[133] G. Chang et al., “Regulated interfacial thermal conductance between Cu and diamond by a TiC interlayer for thermal management applications,” *ACS Applied Materials and Interfaces*, vol. 11 (29), pp. 26507–26517, 2019.

[134] C. Monachon, L. Weber, “Thermal boundary conductance of transition metals on diamond,” *Emerging Materials Research*, vol. 1 (2), pp. 89–98, 2012.

[135] C. Monachon, G. Schusteritsch, E. Kaxiras, L. Weber, “Qualitative link between work of adhesion and thermal conductance of metal/diamond interfaces,” *Journal of Applied Physics*, vol. 115 (12), 2014.

[136] V. Sinha, J. J. Gengler, C. Muratore, J. E. Spowart, “Effects of disorder state and interfacial layer on thermal transport in copper/diamond system,” *Journal of Applied Physics*, vol. 117 (7), 2015.

[137] T. Schubert, B. Trindade, T. Weißgärber, B. Kieback, “Interfacial design of Cu-based composites prepared by powder metallurgy for heat sink applications,” *Materials Science and Engineering A*, vol. 475 (1–2), pp. 39–44, 2008.

[138] A. V. Andreyev, H. Kanda, “Diamond formation and wettability in a Mg–Cu–C system under high pressure and high temperature,” *Diamond and Related Materials*, vol. 6 (1), pp. 28–32, 1997.

[139] Q. Sun, O. T. Inal, “Fabrication and characterization of diamond/copper composites for thermal management substrate applications,” *Materials Science and Engineering B*, vol. 41 (2), pp. 261–266, 1996.

[140] R. J. MacNamara, T. L. Lupton, R. Lupoi, A. J. Robinson, “Enhanced nucleate pool boiling on copper-diamond textured surfaces,” *Applied Thermal Engineering*, vol. 162, 2019.

[141] H. Chen, C. Jia, S. Li, “Interfacial characterization and thermal conductivity of diamond/Cu composites prepared by two HPHT techniques,” *Journal of Materials Science*, vol. 47 (7), pp. 3367–3375, 2012.

[142] A. Gowda, D. Esler, S. Tonapi, K. Nagarkar, K. Srihari, “Voids in thermal interface material layers and their effect on thermal performance,” *Proceedings of the Electronics Packaging Technology Conference*, pp. 41–46, 2004.

[143] F. Sarvar, D. Whalley, P. Conway, "Thermal interface materials — A review of the state of the art," *Electronic Systemintegration Technology Conference*, pp. 1292–1302, 2006.

[144] D. Blazej, "Thermal Interface Materials," *Electronics Cooling*.

[145] "Linear Thermal Expansion Coefficients of Materials," The Engineering ToolBox.

[146] J. Liu, D.-B. Xiong, Y. Su, Q. Guo, Z. Li, D. Zhang, "Effect of thermal cycling on the mechanical properties of carbon nanotubes reinforced copper matrix nanolaminated composites," *Materials Science and Engineering A*, vol. 739, pp. 132–139, 2019.

[147] H. Hu, J. Kong, "Improved thermal performance of diamond-copper composites with boron carbide coating," *Journal of Materials Engineering and Performance*, vol. 23 (2), pp. 651–657, 2014.

[148] K. Chu, C. Jia, H. Guo, W. Li, "On the thermal conductivity of Cu–Zr/diamond composites," *Materials and Design*, vol. 45, pp. 36–42, 2013.

[149] A. M. Abyzov, F. M. Shakhov, A. I. Averkin, V. I. Nikolaev, "Mechanical properties of a diamond-copper composite with high thermal conductivity," *Materials and Design*, vol. 87, pp. 527–539, 2015.

[150] L. Wang et al., "Unveiling interfacial structure and improving thermal conductivity of Cu/diamond composites reinforced with Zr-coated diamond particles," *Vacuum*, vol. 202, 2022.

[151] Q. Kang et al., "Preparation of copper-diamond composites with chromium carbide coatings on diamond particles for heat sink applications," *Applied Thermal Engineering*, vol. 60 (1–2), pp. 423–429, 2013.

[152] Y. Li et al., "Interfacial characterization and thermal conductivity of diamond/Cu composites prepared by liquid-solid separation technique," *Nanomaterials*, vol. 13 (5), 2023.

[153] T. Schubert, Ł. Ciupiński, W. Zieliński, A. Michalski, T. Weißgärber, B. Kieback, "Interfacial characterization of Cu/diamond composites prepared by powder metallurgy for heat sink applications," *Scripta Materialia*, vol. 58 (4), pp. 263–266, 2008.

[154] M. Zain-ul-abdein, K. Raza, F. A. Khalid, T. Mabrouki, "Numerical investigation of the effect of interfacial thermal resistance upon the thermal conductivity of copper/diamond composites," *Materials and Design*, vol. 86, pp. 248–258, 2015.

[155] S. Ren et al., "Effect of coating on the microstructure and thermal conductivities of diamond–Cu composites prepared by powder metallurgy," *Composites Science and Technology*, vol. 71 (13), pp. 1550–1555, 2011.

[156] T. L. Bergman, F. P. Incropera, *Fundamentals of Heat and Mass Transfer*, 7th ed., Wiley, 2011.

[157] C. Parente, M. Pepe, "Benefit of the integration of visible and thermal infrared images for the survey and energy efficiency analysis in the construction field," *Journal of Applied Engineering Science*, vol. 17 (4), pp. 571–578, 2019.

Appendix A: Supplemental Materials

A.1 Sample Orientation Index Calculation

Figure A.1 shows the XRD pattern of the pure Cu reference sample used to illustrate the procedure for calculating the orientation index (OI). Individual diffraction peaks corresponding to FCC-allowed reflections were fitted using Lorentzian profiles to obtain the integrated peak areas. A representative Lorentzian fit for the Cu (111) reflection is shown in **Figure A.2**. The extracted fitting parameters, including the peak position, full width at half maximum (FWHM), and integrated peak area, are summarized in **Table A.1**. These integrated peak areas were subsequently used in the calculation of the orientation index.

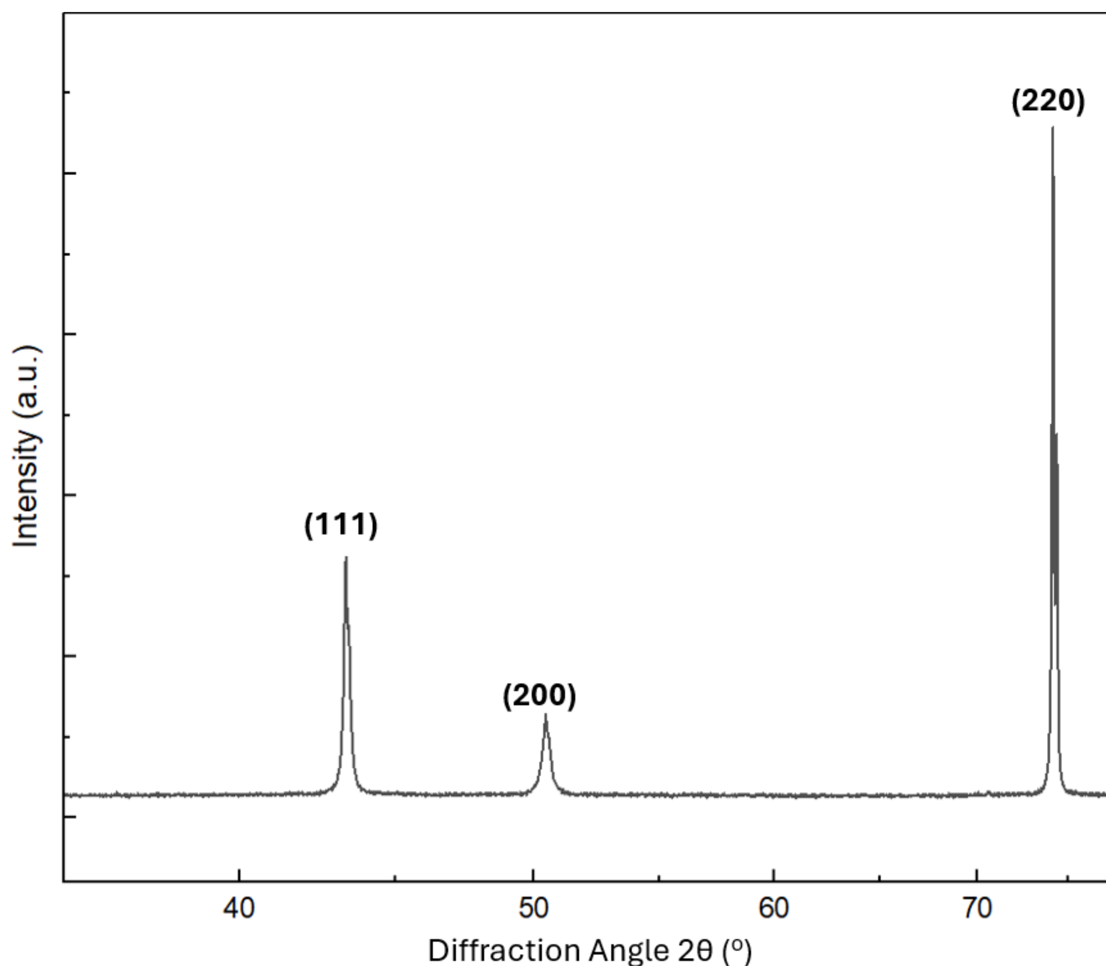

Figure A.1: XRD pattern of the pure Cu reference sample.

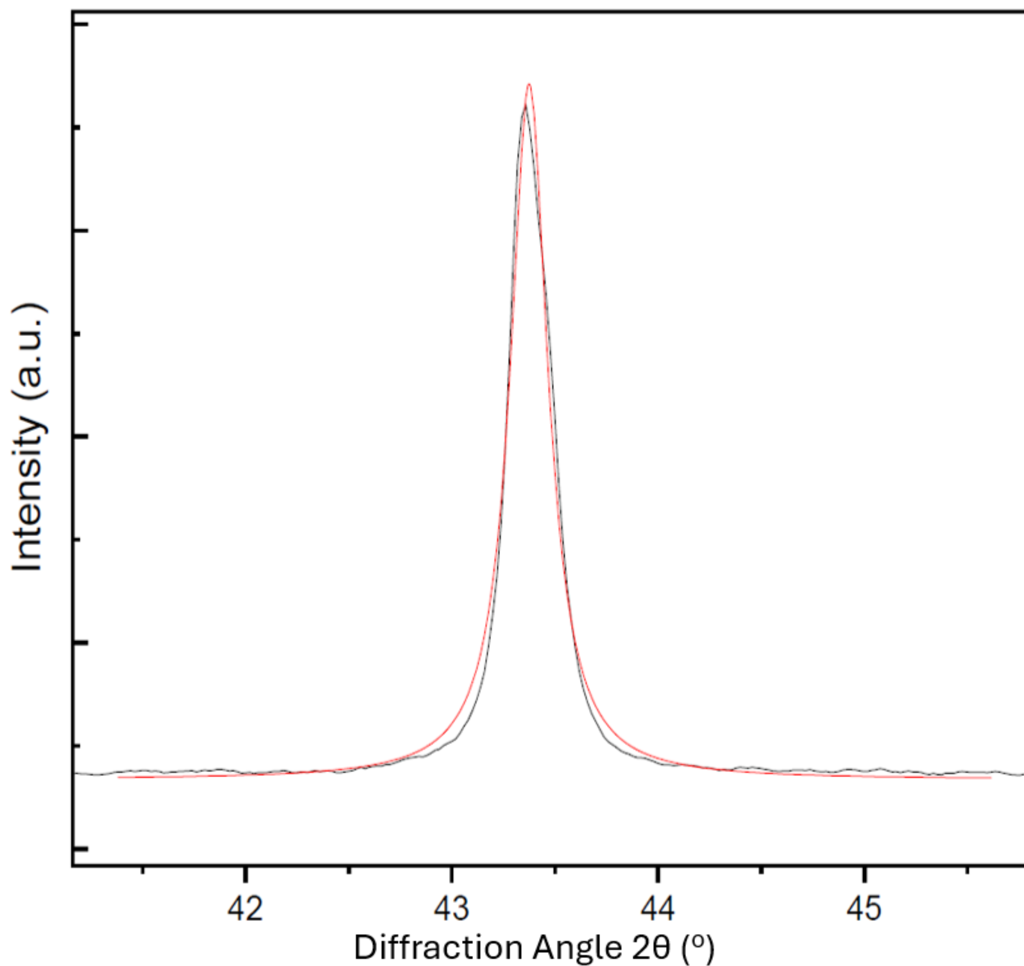

Figure A.2: Lorentz peak fit for the Cu (111) reflection used to determine the integrated peak area.

Table A.1 - Lorentzian peak fitting parameters for the Cu (111) reflection obtained from the pure Cu reference sample, including peak center position, full width at half maximum (FWHM), and integrated peak area used for orientation index calculations.

Parameter	Value
Fitting type	Lorentzian
Peak center, 2θ (°)	43.374 ± 0.001
Full width at half maximum, FWHM (°)	0.221 ± 0.003
Peak area (Intensity, a.u.)	2348.9 ± 26.6

Step 1: Identify the reflection

The peak at $2\theta = 43.37°$ corresponds to the FCC (111) plane.

Reflection parameters used:

Plane	**h**	**k**	**l**	**m = $h^2 + k^2 + l^2$**
(111)	1	1	1	3

Step 2: Extract the integrated peak area

From the Lorentz peak fit:

Integrated area, A (111) = 2348.89369

FWHM = 0.2215

$R^2 = 0.9888$

This integrated area is used in intensity fraction calculation.

Step 3: Calculate the intensity fraction (IF)

Using peak areas obtained for all FCC reflections in the pure Cu sample:

Miller Index	**Area(A)**
(111)	2348.89
(200)	1258.53
(220)	3922.53
(222)	1647.95

$$\sum I = 2348.89 + 1258.53 + 3922.53 + 1647.95 = 9180.0$$

$$IFR_{111} = \frac{2348.89}{9180.0} = 0.2559$$

Step 4: Reference intensity fraction (IFR)

From the ICSD reference data:

$$IFR_{111} = \ 0.06024$$

Step 5: Orientation index (OI)

$$OI_{111} = \frac{IF_{111}}{IFR_{111}} = \frac{0.2559}{0.6024} = \mathbf{0.4248}$$

This value indicates that the (111) plane is not preferentially oriented relative to the ICSD powder reference (OI < 1).

A.2 DEM-Based Evaluation of the Influence of Thermal Boundary Conductance on Composite Thermal Conductivity

To further support the experimental trends discussed in Section 4.3, supplementary DEM modelling results are provided in **Figures A.3** and **A.4** to illustrate the critical role of thermal boundary conductance in determining the effectiveness of diamond reinforcement in copper-based heat sinks. As shown in **Figure A.3**, even though 400µm diamond particles possess exceptionally high intrinsic thermal conductivity (1800 W/m·K), the effective conductivity of a Cu-D composite remains below that of pure copper when the interfacial conductance is low. A sharp rise in composite conductivity occurs only once the TBC exceeds approximately 2.6 MW/m²·K. **Figure A.4** supports this behavior by demonstrating that the benefit of increasing diamond volume fraction is entirely dependent on achieving sufficiently high TBC. At low conductance values (~1 MW/m²·K), adding diamond reduces thermal conductivity, whereas at higher conductance (~10 MW/m²·K), the composite conductivity increases steadily with particle loading. These DEM predictions directly support the experimental findings of this chapter by showing that the limited heat sink performance of uncoated composites arises not from microstructural defects but from restricted phonon transmission at the Cu-D interface.

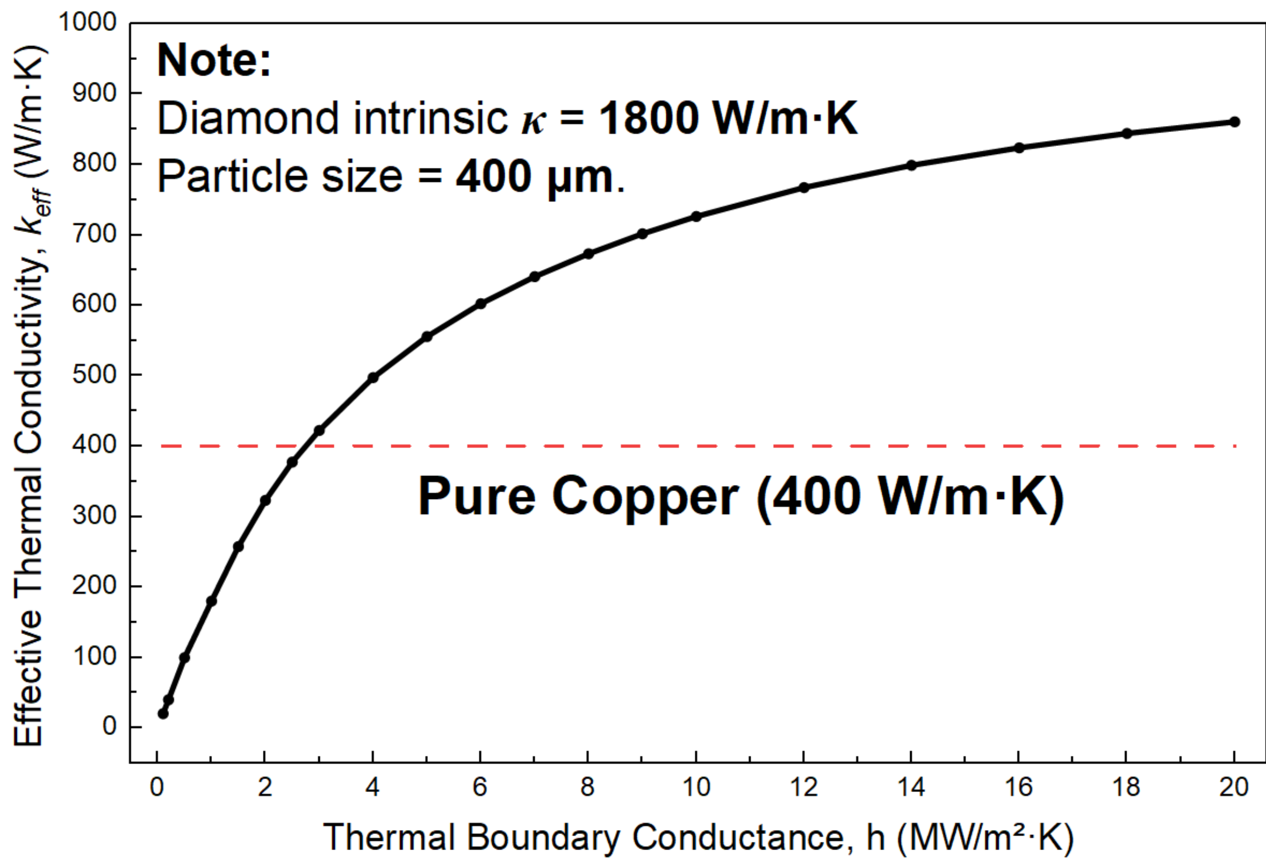

Figure A.3: DEM-predicted effective thermal conductivity of a Cu-D composite versus thermal boundary conductance (TBC) for 400-µm diamond particles (k = 1800 W/m·K). Conductivity remains below pure copper at low TBC and increases sharply above ~2–3 MW/m²·K.

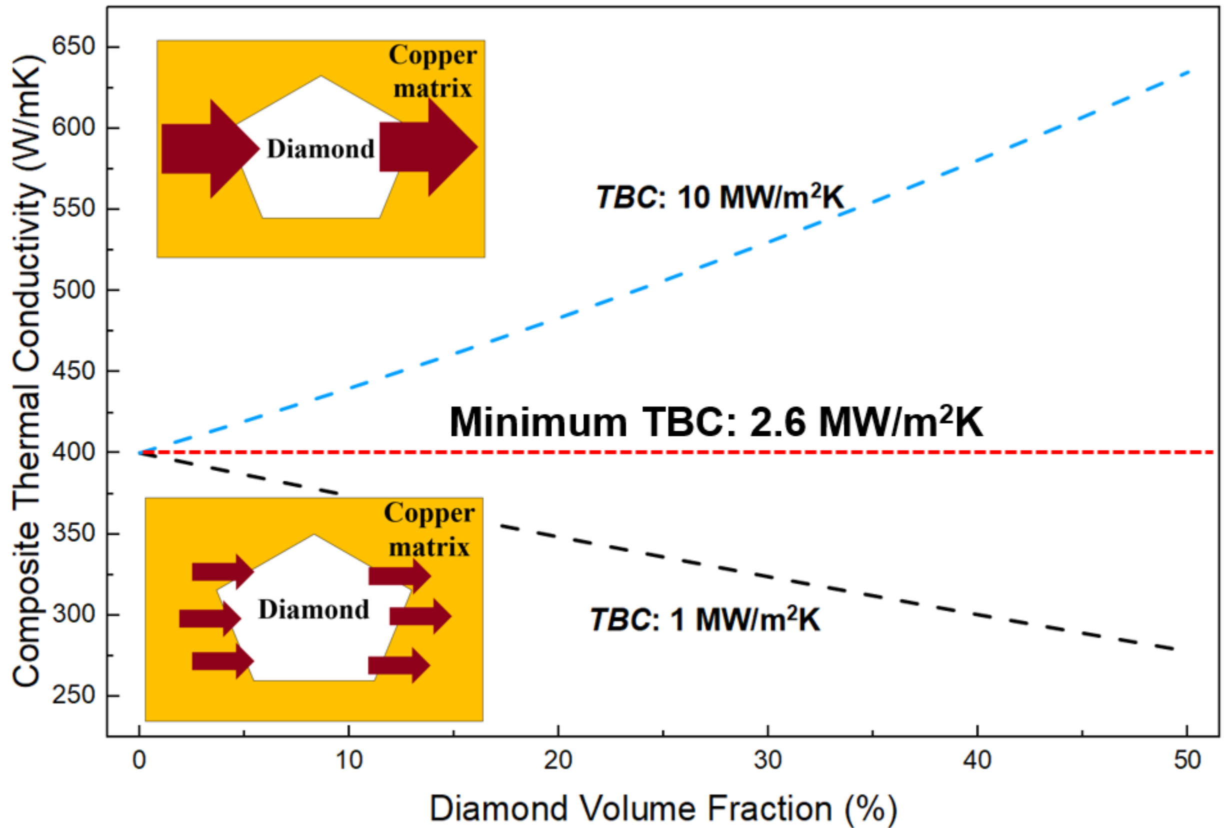

Figure A.4: DEM-predicted composite thermal conductivity versus diamond volume fraction at varying thermal boundary conductance (TBC). Conductivity decreases at low TBC (~1 $MW/m^2 \cdot K$) but increases at high TBC (~10 $MW/m^2 \cdot K$). A minimum TBC of ~2.6 $MW/m^2 \cdot K$ is required to exceed pure copper.

A.3 Copper–diamond TBC values from literature

Supplementary **Table A.2** provides the numerical data set used to generate **Figure 17**. It compiles thermal boundary conductance (TBC) values at Cu-D interfaces without intermediate coatings from both electrodeposited and high-temperature synthesized composites. Reported values are taken directly from the literature, and missing TBC values are derived using the differential effective medium model.

Table A.2 - Literature values of thermal boundary conductance (TBC) at uncoated copper–diamond interfaces. Highest reported values are listed; missing values were estimated using the DEM model.

Electrodeposition		
Diamond particle size (μm)	TBC (MW/m^2K)	Source
400	3.4	Cho *et al.* [42]
420	3.1	Cho *et al.* [44]
30	48	Wu *et al.* [41]
100	55	Wu *et al*. [113]
100	48.8	Wu *et al.* [45]
170	21.3	Luo *et al.* [115]
100	47.6	Wu *et al.* [43]
230	15	Arai & Ueda [48]
230	15	Arai & Ueda [47]
150	73	Zhuo *et al.* [114]
High temperature methods		
Diamond particle size (μm)	TBC (MW/m^2K)	Source
75	1.03	Li *et al.* [82]
100	5	Hu & Kong [147]
110	1.8	Chu *et al.* [148]
90	2	Chu *et al.* [103]
100	1.6	Chu *et al.* [80]
100	50	Abyzov *et al.* [149]
230	0.4	Wang *et al.* [150]
70	3.4	Kang *et al.* [151], [152]
55	50	Chen *et al.* [141]
102	4.8	Li *et al.* [152]
125	0.5	Schubert *et al.* [137]
195	5	Schubert *et al.* [153]
75	2.4	Zhang *et al.* [104]
100	29.7	Yoshida & Morigami [108]
100	0.5	Zain-ul-abdein *et al.* [154]
210	30.5	Xu *et al.* [131]
100	2.4	Ren et al. [155]

A.4 Manual Lower- and Upper-Bound Pore Population Analysis

Manual pore population analysis was performed using ImageJ to account for uncertainty associated with optical contrast and pore definition in the thermal paste micrographs. The image scale was first calibrated using the 50 µm scale bar present in each micrograph. Point counting was then carried out using the ImageJ Point Tool. For the lower-bound analysis (**Figure A.5a**),

only large, dark, and clearly resolved pore features were counted. Ambiguous features and low-contrast regions were intentionally excluded to ensure a conservative estimate of pore population. For the upper-bound analysis (**Figure A.5b**), all non-uniform contrast features within the image, including small and weakly contrasted regions that may correspond to pores, were counted. This approach intentionally overestimates pore population to bracket uncertainty associated with optical imaging limitations. The total image area was measured directly in ImageJ, and pore population density was calculated by normalizing the counted features by the image area.

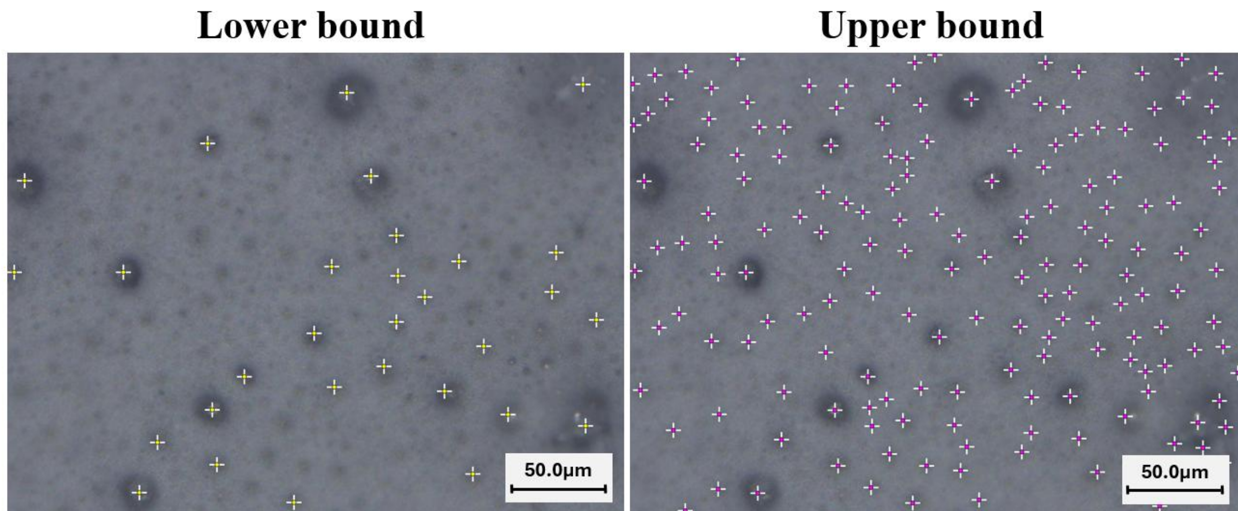

Figure A.5: ImageJ-based manual pore population analysis of commercial SYY thermal paste: (a) lower-bound estimate from clearly defined pores; (b) upper-bound estimate including all possible pore features. The true population lies between these limits. Scale bar: 50 µm.

A.5 Thermal paste lightly pressed vs hardly pressed

As discussed in Chapter 5, a thicker interface increases the effective thermal resistance of the TIM layer. This geometric effect is reflected in the steady-state thermal response: the lightly pressed sample reached a higher LED temperature (70.75 °C) than the hard-pressed interface (69.70 °C) (**Figure A.7**), despite both tests using the same TIM and the same applied power.

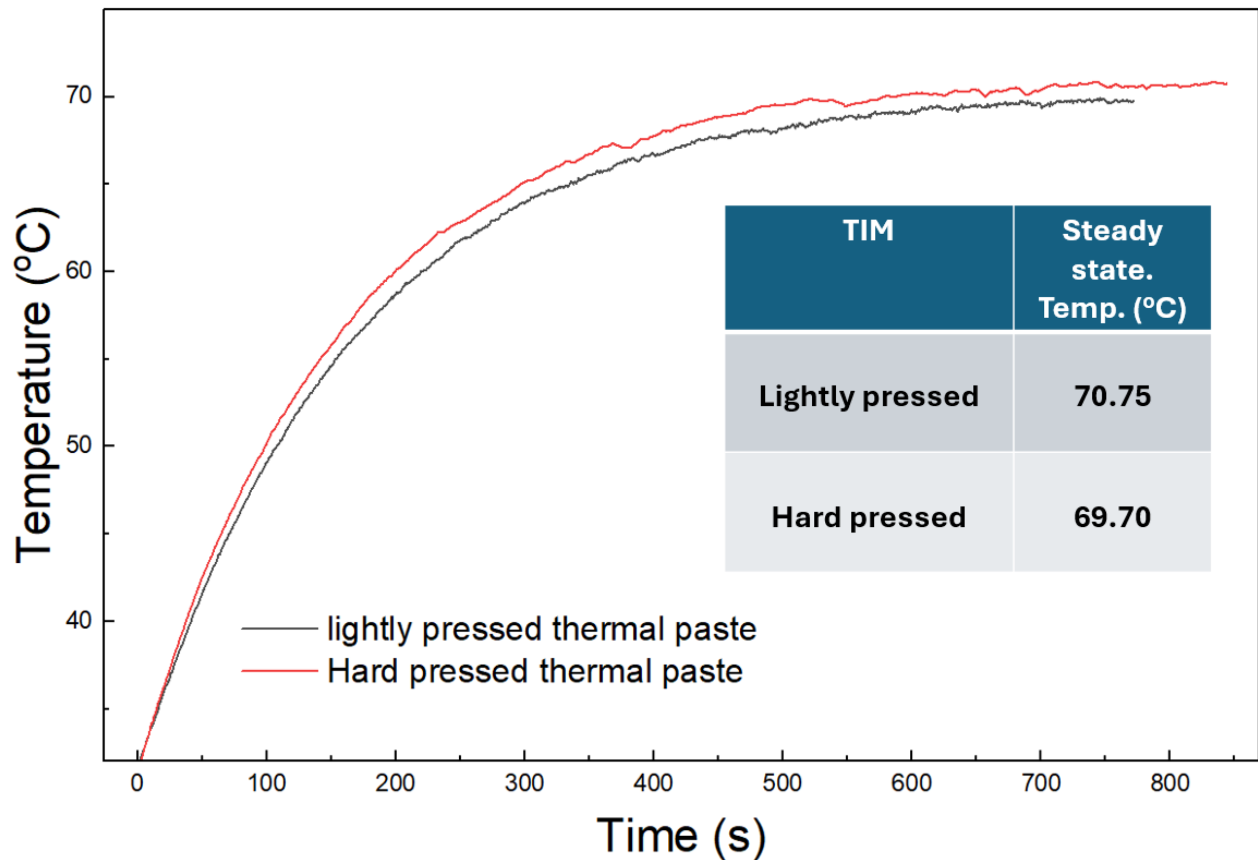

Figure A.6: Measured bond-line thickness of the commercial thermal paste under light and hard pressing conditions. Light pressing produces a noticeably thicker TIM layer, which contributes to higher thermal resistance and reduced cooling performance.

A.6 Steady-State Thermal calculations with Convection, Radiation and Interfacial Resistance

A steady-state one-dimensional heat transfer model was formulated to relate the junction temperature of the aluminum heater substrate to the area-normalized interfacial thermal resistance between the aluminum substrate and the copper heat sink. Heat generated in the aluminum flows through the TIM layer and across the aluminum–TIM–copper interfaces to the outer copper surface. All other external surfaces are treated as thermally insulated, such that heat removal occurs exclusively from the exposed copper surface by natural convection and thermal radiation. Under these assumptions lateral heat spreading is neglected. A schematic illustration of the assumed heat-flow path and boundary conditions is shown in **Figure A.8**.

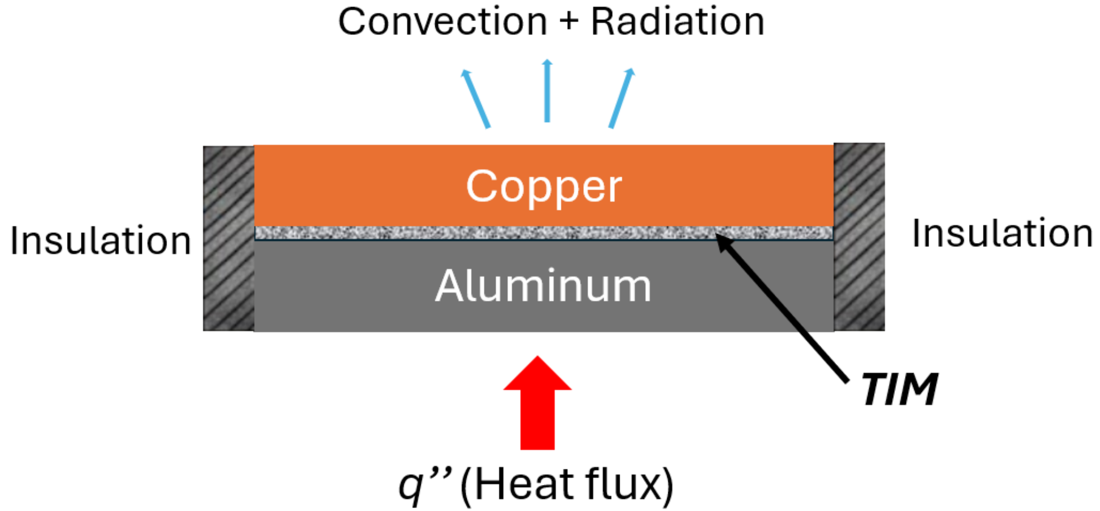

Figure A.7: Simplified steady-state one-dimensional heat transfer model showing heat flow from the aluminum heater through the thermal interface material (TIM) to the copper heat sink, with dissipation by natural convection and radiation.

The applied heat flux was estimated from the transient heating response of the aluminum heater substrate using an energy balance. The rate of temperature rise measured experimentally was $\frac{dT}{dt} = 0.394\mathrm{K/s}$, and the heat flux was calculated using:

$$q'' = \frac{mc_p}{A}\frac{dT}{dt} \tag{A.1}$$

where m and A are the mass and planform area of the aluminum part and c_p is the specific heat capacity of aluminum. Using the known mass-to-area ratio of the aluminum, the resulting effective heat flux was approximately $q'' = 950\ W/m^2$. This value represents the heat input to the heat sink system under the applied electrical loading and is therefore used in the steady-state analysis presented in this appendix.

At the outer copper surface, the arriving heat flux must equal the combined convective and radiative losses to the environment. The surface temperature T_s therefore satisfies:

$$q'' = h_c\,(T_s - T_\infty) + \varepsilon\sigma\,[\,(T_s + 273.15)^4 - (T_\infty + 273.15)^4] \tag{A.2}$$

where T_∞ is the ambient air temperature, h_c is the natural convection heat transfer coefficient, ε is the surface emissivity of the copper heat sink, and σ is the Stefan–Boltzmann constant. The ambient temperature was taken as $T_\infty = 23°\text{C}$, corresponding to the measured laboratory room temperature during testing. A natural convection heat transfer coefficient of $h_c = 10\ \text{W/m}^2$ was used, which is representative of free convection from small horizontal metallic surfaces in quiescent air under laboratory conditions [156]. An emissivity value of $\varepsilon = 0.1$ was selected for the copper heat sink. While fully polished metallic surfaces can exhibit emissivities as low as ~ 0.05, the electrodeposited copper surface used in this study was neither mirror-polished nor severely roughened [157]. The chosen value therefore represents an intermediate, physically realistic emissivity that avoids underestimating or overestimating radiative heat losses. Substituting these values into Eq. (A.2) gives:

$$950 = 10\,(T_s - 23) + 0.1\,(5.67\times10^{-8})\,(T_s^4 - 296^4) \quad \text{(A.3)}$$

The resulting steady-state copper surface temperature is approximately 63°C. This temperature is set entirely by the convection and radiation boundary conditions and is not affected by the magnitude of the interface resistance.

The temperature rise between the aluminum substrate (junction temperature T_j) and the copper surface temperature T_s is governed by the interfacial thermal resistance, expressed in area-normalized form R_c'' ($\text{m}^2\cdot\text{K/W}$). The junction temperature may therefore be written as:

$$T_j = T_s + q''\,R_c'' \quad \text{(A.4)}$$

For the present system, the interfacial thermal resistance is dominated by heat conduction through the thermal interface material layer rather than bulk conduction through the copper or aluminum. The effective interfacial resistance may therefore be expressed as

$$R_c'' = \frac{t_{TIM}}{k_{TIM}} \quad \text{(A.5)}$$

where t_{TIM} is the TIM bond-line thickness and k_{TIM} is its effective thermal conductivity. Equation (A.5) shows that the interfacial resistance increases linearly with TIM thickness for a given material conductivity.

Substituting Eq. (A.5) into Eq. (A.4) demonstrates that, under any positive applied heat flux, the junction temperature increases directly with TIM thickness. Thicker TIM layers therefore result in higher junction temperatures, while reducing the bond-line thickness lowers the effective interfacial resistance and minimizes the temperature rise between the aluminum substrate and the copper surface.

Representative steady-state junction temperatures calculated using Equations (A.4) and (A.5) are presented in **Table A.3**. The interfacial thermal resistance values are derived directly from the thermal interface material bond-line thickness using $R_c'' = t_{\text{TIM}}/k_{\text{TIM}}$, with an effective thermal conductivity of $k_{\text{TIM}} = 0.61\ \text{W/m}\cdot\text{K}$. The selected thicknesses of 50–300 µm span the experimentally observed range in this study and allow the effect of increasing TIM thickness on junction temperature to be calculated.

Table A.3 – Steady-state junction temperature as a function of TIM bond-line thickness (Calculated using $q'' = 950\ \text{W/m}^2$, $k_{\text{TIM}} = 0.61\ \text{W/m}\cdot\text{K}$, and $T_s = 63.0°\text{C}$.)

t_{TIM} (µm)	R_c'' (m²·K/W)	Increase above T_s (°C)	T_j (°C)
50	8.20×10^{-5}	0.0779	63.0779
100	1.64×10^{-4}	0.1557	63.1557
150	2.46×10^{-4}	0.2336	63.2336
200	3.28×10^{-4}	0.3115	63.3115
250	4.10×10^{-4}	0.3893	63.3893
300	4.92×10^{-4}	0.4672	63.4672

These results show that, for thin and relatively high-conductivity TIM layers, interfacial thermal resistance contributes to a temperature rise under any positive heat flux. This analysis highlights

the importance of minimizing TIM bond-line thickness and maintaining good interfacial contact to achieve optimal steady-state thermal performance.

A.7 Sample Copper Deposition Thickness Estimation for Agitation Timing

Electrodeposited copper mass can be estimated with Faradays law as per below:

$$m = \frac{ItM}{nF} \tag{A.6}$$

where m is the deposited copper mass, I is the applied current, t is the deposition time, M is the molar mass of copper, $n = 2$ for $Cu^{2+} + 2e^{-} \rightarrow Cu$, and F is Faraday's constant.

Using the applied current of 12 mA, cathode area of 1×1 cm², and copper density of 8.9 g/cm³, the approximate copper deposition thickness was estimated to guide the timing of agitation and additional diamond stacking during multilayer electrodeposition.

Table A.4 – Sample thickness estimation for a given deposition time

Estimated Cu Thickness	Approximate Time
1 mm Cu	~62.5 hrs
0.5 mm Cu	~31.2 hrs
0.5 mm layer with 50 vol.% diamond assumption	~15.6 hrs

These values provide an approximate estimate of copper growth time under the selected deposition conditions. During fabrication, agitation bursts of approximately 400 RPM for 1 min were applied only after sufficient copper coverage had formed over the previous diamond layer. This helped maintain particle redistribution while reducing the risk of disturbing poorly diamond particles.